Trafficking of voltage-activated calcium channels

Inaugural-Dissertation

zur Erlangung des Doktorgrades
der Mathematisch-Naturwissenschaftlichen Fakultät
der Heinrich-Heine-Universität Düsseldorf

vorgelegt von

Rachel Anna Conrad
aus Dormagen

Jülich, Dezember 2016

aus dem Institut für komplexe Systeme – Zelluläre Biophysik
des Forschungszentrums Jülich

Gedruckt mit der Genehmigung der
Mathematisch-Naturwissenschaftlichen Fakultät der
Heinrich-Heine-Universität Düsseldorf

Referent: Prof. Dr. Patricia Hidalgo

Korreferent: Prof. Dr. Nikolaj Klöcker

Tag der mündlichen Prüfung: 01.06.2017

Ich versichere an Eides Statt, dass die Dissertation von mir selbstständig und ohne unzulässige fremde Hilfe unter Beachtung der „Grundsätze zur Sicherung guter wissenschaftlicher Praxis“ an der Heinrich-Heine Universität Düsseldorf erstellt worden ist.

_____ _____

Ort, Datum Unterschrift

Abstract

Voltage-activated calcium channels (VACC) are major contributors to the entry of calcium into excitable cells that in turn initiates a variety of cellular functions. In order to coordinate calcium signals and to prevent deleterious intracellular calcium accumulation, permeation through these channels is tightly regulated in time and space. The amount of calcium entering the cell is controlled by its biophysical properties as well as by the number of channels assembled in the plasma membrane. The mechanisms regulating VACCs cell surface expression that is given by the balance between anterograde and retrograde trafficking are poorly understood. VACCs are hetero-multimers formed by an α_1 pore-forming subunit ($Ca_V\alpha_1$) that associates with one or more accessory subunits, including the β-subunit ($Ca_V\beta$). It is well established that $Ca_V\beta$ is required for $Ca_V\alpha_1$ exit from the endoplasmic reticulum (ER), and that $Ca_V\alpha_1$ - $Ca_V\beta$ association at the level of the plasma membrane is reversible though the subunit stoichiometry of the transport is unclear. The aim of this study was to investigate the trafficking pathway of the L-type $Ca_V1.2$ channels that are predominantly expressed in cardiac cells and the effect of $Ca_V\beta$. Further I aimed to analyze the motional dynamics of the channel during its itinerary. I used molecular biology techniques to express fluorescently labelled $Ca_V1.2$ and $Ca_V\beta$ in mammalian cells and laser scanning confocal microscopy for live imaging to visualize the channel's location during its anterograde and retrograde pathway. Single particle tracking was used to estimate the type of motion as well as the dynamic parameters of the channel during its intracellular journey and compares the effect of two isoforms $Ca_V\beta2a$ and $Ca_V\beta2b$.

My results show that $Ca_V\beta$ provides a very efficient release of $Ca_V1.2$ from the ER to the Golgi-system independent from microtubules integrity and that the channels, packed into vesicles, are further cotransported with $Ca_V\beta$ along microtubules towards the plasma membrane. The two $Ca_V\beta$ isoforms show different impact on the channels transport dynamics. During its itinerary the channels shows alternating motion combining directed active transport interrupted by periods of confined movement. The channel surface expression is regulated by an actin-dependent endosomal recycling pathway, lysosomal degradation does not contribute. Dissociation of $Ca_V\beta$ at the level of the plasma membrane is the regulatory factor, initiating the internalization and the retrograde transport of $Ca_V1.2$ towards recycling endosomes until its reinsertion in the plasma membrane. In summary my work contributes to understand the intracellular transport of voltage-activated calcium channels.

Zusammenfassung

Spannungsabhängige Kalziumkanäle (VACC) sind maßgeblich an dem Einfluss von Kalziumionen in erregbare Zellen beteiligt, wodurch eine Vielzahl zellulärer Funktionen gesteuert wird. Um diese Kalziumsignale zu koordinieren und gleichzeitig eine schädliche Akkumulation von Kalzium in der Zelle zu vermeiden, muss die Regulation der Kanäle sowohl zeitlich als auch räumlich sehr präzise kontrolliert werden. Der regulierende Mechanismus für die gleichbleibende Expression von Kanälen an der Zelloberfläche ist die Erhaltung eines Gleichgewichts zwischen nach außen und nach innen gerichtetem Transport innerhalb der Zelle. VACCs bestehen je nach Subtyp aus einer porenbildenden α_1-Untereinheit ($Ca_V\alpha_1$) assoziiert mit einer oder mehreren zusätzlichen Untereinheiten, einschließlich der β-Untereinheit ($Ca_V\beta$). Es ist bekannt, dass $Ca_V\beta$ für die Freisetzung von $Ca_V\alpha_1$ aus dem Endoplasmatischen Retikulum (ER) notwendig, und dass die Assoziation der beiden Untereinheiten an der Plasmamembran reversibel ist. Das Ziel dieser Arbeit war es, den Transportweg des Kanals mit Hinblick auf die regulatorische Funktion von $Ca_V\beta$ zu untersuchen. Außerdem wurden die Bewegungsparameter des Kanals genauer analysiert. Dafür wurden $Ca_V1.2$, überwiegend vorkommend in Herzzellen, und $Ca_V\beta$ fluoreszent markiert und deren Lokalisation und Bewegung in lebenden HEK293 Zellen mithilfe von konfokaler Laserscanning-Mikroskopie untersucht. Durch ‚Single particle tracking' wurden die Bewegungsvorgänge des Kanals sowie deren dynamische Parameter bestimmt. Ich konnte beobachten, dass $Ca_V\beta$ eine sehr effiziente Freilassung von $Ca_V1.2$ aus dem ER und einen schnellen Transport zum Golgi herbeiführt, unabhängig von Tubulin. Vom Golgi aus werden die Kanäle, in Vesikeln, im Kotransport mit $Ca_V\beta$, durch Motorproteine entlang von Tubulin Filamenten zur Plasmamembran transportiert. Dabei zeigen die beiden Isoformen von $Ca_V\beta$, 2a und 2b, einen unterschiedlichen Einfluss auf die Transportdynamik von $Ca_V1.2$. Entlang der Transportroute zeigt der Kanal alternierende Bewegungsformen von aktivem Transport unterbrochen von Perioden beschränkter Zufallsbewegung. Die Expression der Kanäle in der Membran wird durch einen von F-Aktin abhängigen Recycling Prozess reguliert, es findet kein lysosomaler Abbau statt. Dabei ist $Ca_V\beta$ der regulierende Faktor. Durch Dissoziation von $Ca_V1.2$ an der Plasmamembran initiiert $Ca_V\beta$ dessen Internalisierung und den retrograden Transport zum Recycling Endosome und die anschließende Wiedereinfügung in die Plasmamembran. Zusammengefasst, trägt meine Arbeit zum Verständnis des intrazellulären Transports spannungsabhängiger Kalziumkanäle bei.

Danksagung

An dieser Stelle möchte ich meinen besonderen Dank nachstehenden Personen entgegen bringen, die mich während meiner Dissertationszeit begleitet und unterstützt haben:

Mein außerordentlicher Dank gilt an erster Stelle Frau Prof. Dr. Patricia Hidalgo, meiner Doktormutter, für die Möglichkeit der Durchführung meiner Arbeit. Vielen Dank für die intensive persönliche Betreuung, für konstruktive Gespräche und immer neue Ideen, aber auch für viel Verständnis und aufmunternde Worte.

Außerdem danke ich sehr Herrn Prof. Dr. Christoph Fahlke, der als Institutsleiter mein Projekt immer unterstützt und gefördert hat, und der mir somit die Möglichkeit gab, diese Arbeit durchzuführen.

Ebenfalls danke ich Herrn Prof. Dr. Klöcker für die unkomplizierte Übernahme des Zweitgutachtens und sein Interesse an meiner Arbeit.

Besonders herzlich möchte ich mich bei Nadine Jordan bedanken, die mich mit großer experimenteller Hilfe und in vielen persönlichen Gesprächen mit aufbauenden Worten sehr unterstützt hat.

Mein Dank gilt weiterhin Arne Franzen für die große Unterstützung bei molekularbiologischen Planungen und Experimenten.

Außerdem möchte ich mich sehr bei Daniel Kortzak bedanken, der mir in letzter Minute noch mit einer wichtigen statistischen Auswertung geholfen hat.

Bei Johnny Hendriks möchte ich mich bedanken für die Bereitstellung seiner Super-Resolution Bilder.

Weiterhin bedanke ich mich bei Anita Eckert, Thomas Gensch, Christoph Aretzweiler, Gustavo Guzman, Gabriel Stölting, Felix Beinlich, Bettina Mertens und allen technischen und wissenschaftlichen Mitarbeitern des ICS4 für gute Zusammenarbeit, hilfreiche Unterstützung und fachliche Diskussion und bei Rudolf Esser für viel Gemüse und lustige Momente.

Darüber hinaus gilt mein großer Dank meinen lieben Kolleginnen und Freundinnen Anna Sieben und Verena Untiet. Danke für viele aufmunternde und ermutigende Worte, so manchen wertvollen Ratschlag, viele kritische Diskussionen aber auch das ein oder andere ablenkende lustige Gespräch in unserem gemeinsamen Büro und viele tolle Erinnerungen.

Allen meinen lieben Freunden danke ich für die Ausdauer, Ruhe und Geduld, womit sie mir stets zur Seite standen und mich immer wieder aufgemuntert haben.

Ich danke außerdem sehr meinem Bruder Ruben Conrad, für viel ehrliche Kritik und ermutigende Worte.

Mein ganz besonderer Dank gilt meinem Freund Matthias Schrammen. Für seine mühevolle Geduld mir immer wieder bei mathematischen Problemen zu helfen und sein liebevolles Verständnis in meiner anstrengenden Schreibphase.

Aus tiefstem Herzen danke ich meinen Eltern Hans-Rolf und Ingrid Conrad, die mir meinen bisherigen Lebensweg ermöglicht haben, mich immer unterstützt und an mich geglaubt haben und denen ich diese Arbeit widme. Ihr wart immer für mich da, habt mich aufgebaut und mir immer geholfen. Danke für alles.

List of tables

List of figures

Index

1 Introduction

'The least movement is of importance for all nature.'

These words of the physicist Blaise Pascal describe movement as essential feature for life. Without movement no life would have developed. The movement of particles allows their encounters leading to chemical reactions that ensure propagation of life. Cells are delimited from the extracellular space by a biological plasma membrane that encompasses several transmembrane proteins. These plasma membrane proteins act as sensors to external signals and are responsible for the transmembrane transport of ions or other small essential molecules (Alberts 2008). Membrane proteins, produced in the cell interior, must be transported to the cell surface. This journey can be over micrometer distance or for example in polarized cell up to a meter. The protein transport is highly regulated ensuring that proteins are delivered to their final destination in the right amount.

In my study, I investigated the transport of one membrane protein belonging to the large family of ion channels, the so called voltage-activated calcium channels. They allow the entry of one of the most ubiquitous second messenger molecule, the calcium ions (Clapham 2007). Calcium entering to the cell triggers diverse cellular processes including proliferation, synaptic transmission, excitation-contraction coupling, hormone secretion and gene expression. An excessive entry of calcium into the cell may lead to strong cytotoxic effects (Szydlowska and Tymianski 2010) but a lack of calcium can also cause loss of important biological responses due to missing signaling processes (Berridge et al. 2000). Thus, calcium influx into the cell is tightly controlled in time and space in order to allow the initiation of different calcium signal cascades while preventing the cytotoxicity due to intracellular calcium accumulation. Voltage-activated calcium channels are the main entry of calcium in excitable cells and thus their transport, quantity and temporal coordination of the membrane insertion are essential for calcium signaling. Defects in the regulation of these processes are associated with pathologic conditions (Neefjes and van der Kant 2014, Smyth and Shaw 2010).

The knowledge about an active transport would increase the possibilities to interfere in the process of transport, given the opportunity to compensate both a lack and a surplus of channels within the plasma membrane. Therefore a detailed understanding of the trafficking

processes of voltage-activated calcium channels will advance the development of strategies aimed at modulating the electrical properties of the cardiomyocyte membrane.

1.1 Voltage-activated calcium channels

Voltage-activated calcium channels are integral membrane proteins that act as mediators of calcium influx into electrically excitable cells. They open in response to membrane depolarization allowing Ca^{2+}-ions to enter the cell from the extracellular space. The transient increase of the cytosolic calcium concentration in turn couples the electrical signals in the cell surface to intracellular processes (Campiglio and Flucher 2015, Catterall 2011, Hofmann et al. 2014, Neely and Hidalgo 2014). According to their electrophysiological properties voltage-gated calcium channels are divided into two classes: Low voltage-activated (LVA) calcium channels are activated by weak depolarization and show transient currents (Yunker and McEnery 2003). High voltage-activated (HVA) channels are activated by relatively strong depolarization and produce long-lasting currents. HVA channels are hetero-multimers formed by a pore-forming transmembrane α_1-subunit ($Ca_V\alpha_1$) associated with the auxiliary $\alpha_2\delta$-($Ca_V\alpha_2\delta$), β- ($Ca_V\beta$) and γ- ($Ca_V\gamma$) subunits (Figure 1.1 and Figure 1.2).

Recently, the three-dimensional structure of the skeletal muscle voltage-activated calcium channel complex was solved by cryo-electron microscopy (Wu et al. 2016). It is shown in Figure 1.1

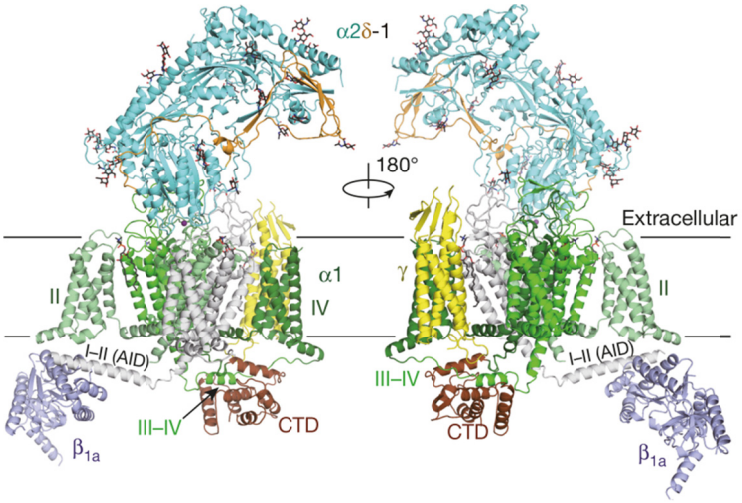

Figure 1.1: Overall structure of the $Ca_V1.1$ complex. The structure of the skeletal muscle voltage-activated calcium channel complex was solved by cryo-electron microscopy encompassing the pore-forming $Ca_V\alpha_1$ with four homologous repeats (I-IV) with accessory $Ca_V\beta$, $Ca_V\alpha_2\delta$ and $Ca_V\gamma$ subunits. Figure taken from (Wu et al. 2016).

The accessory subunits regulate the biophysical properties and surface expression of the $Ca_V\alpha_1$. A scheme of the multi-subunit calcium channel protein complex is shown in Figure 1.2.

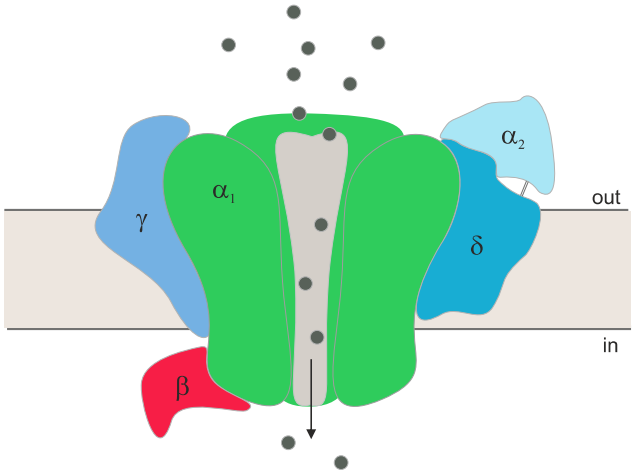

Figure 1.2: The multi-subunit complex of a high-voltage-activated calcium channel. The central pore-forming α_1-subunit is associated with a disulfide-linked glycoprotein dimer of α_2- and δ-subunits, a transmembrane glycoprotein γ-subunit and an intracellular β-subunit. After opening the voltage-activated pore, Ca^{2+}-ions can enter the cell.

The amount of calcium entering into a cell depends on the conduction properties of voltage-activated calcium channels within the plasma membrane and also on the number of functional channels inserted in the plasma membrane. The channel's surface density is regulated by the balance between channels that are being inserted into the plasma membrane (anterograde trafficking or biosynthetic transport) and the channels being removed from the plasma membrane (retrograde). The aim of my thesis was to describe the molecular pathway and regulation of the intracellular transport of voltage-activated calcium channels, in particular of $Ca_V\alpha_1$, and the impact of $Ca_V\beta$ on the channels' trafficking pathway.

1.1.1 The pore-forming α_1-subunit

The pore-forming α_1-subunit ($Ca_V\alpha_1$) of high voltage-activated calcium channels determines the main biophysical and pharmacological properties of the channels. It contains the ion conduction pore, the voltage sensor, and multiple intracellular domains that regulate calcium influx and provide interaction sites for regulatory proteins. The transmembrane topology of $Ca_v\alpha_1$ is shown in Figure 1.3.

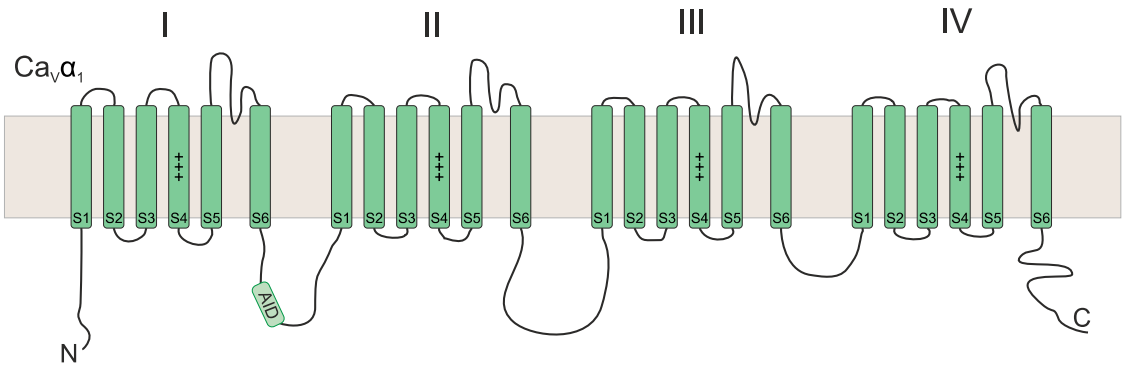

Figure 1.3: Membrane topology of $Ca_V\alpha_1$ protein. $Ca_V\alpha_1$ is a transmembrane protein composed of four domains (I-IV) joined by three cytoplasmic linkers (I-II, II-III and II-IV). Each domain contains six transmembrane segments, S1 to S6 and one entering loop between S5 and S6 that contributes to build the ion conduction pathway. S4 of each domain contains a positively charged voltage sensor. The highly conserved binding site for the $Ca_V\beta$ subunit, the AID (α-interaction domain) located within the intracellular linker connecting domains I and II is shown.

$Ca_V\alpha_1$ contains four homologous domains (I-IV) each with six membrane-spanning segments (S1–S6) connected by intracellular loops. The domains are flanked by cytosolic N- and C-termini. The S4 segments of each domain comprise the voltage sensor, whereas the S5–S6 segments and the reentering loop connecting them form the channel pore and the selectivity filter (Catterall 2011).

Voltage-activated calcium channels are classified according to their $Ca_V\alpha_1$ containing subunit. Ten different types of $Ca_V\alpha_1$ are known that are encoded by ten different genes. They are divided in three classes, $Ca_V1.x$, $Ca_V2.x$ and $Ca_V3.x$. The two first classes including $Ca_V1.1$ – $Ca_V1.4$ as well as $Ca_V2.1$ - $Ca_V2.3$, form the HVA subgroup, whereas three $Ca_V3.x$ ($Ca_V3.1$ – $Ca_V3.3$) belong to the group of LVA channels (Catterall et al. 2005). The HVA group is divided in two subgroups, the biggest comprising of the $Ca_V1.x$ or L-type channels displaying long lasting currents, and the second class, $Ca_V2.x$, comprises the P/Q-, N- and R-types. The $Ca_V3.x$ class encompasses the so called T-type channels that show transient currents and are supposed to comprise only the $Ca_V\alpha_1$ subunit with no associated accessory subunits. Figure 1.4 shows a summary of all $Ca_V\alpha_1$ subunits cloned until now with their corresponding nomenclature.

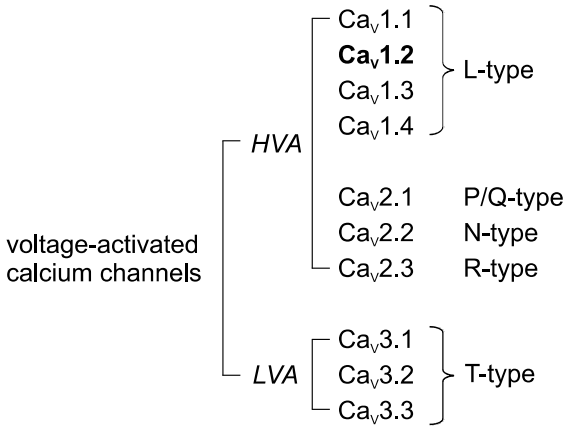

Figure 1.4: Nomenclature of the α_1-subunit of voltage-activated calcium channels. $Ca_V\alpha_1$ is classified in high-voltage activated (HVA) calcium channels, including L-, P/Q-, N- and R-type and low-voltage activated (LVA) calcium channels, comprising only T-type channel (Catterall et al. 2005).

In my studies, I investigated the L-type $Ca_V1.2$ calcium channel. This isoform is predominantly expressed in cardiac muscle cells and plays a key role in excitation-contraction coupling (Catterall 2011, Shaw and Colecraft 2013). Aberrations in the function or number of $Ca_V1.2$ channels in the plasma membrane have been associated with multiple cardiac diseases such as hypertrophy and heart failure (Catterall 2011, Striessnig et al. 2014).

1.1.2 The auxiliary β-subunit

The $Ca_V\beta$ auxiliary subunit is encoded by four nonallelic genes (β1 – β4) each with multiple splice variants. Most $Ca_V\beta$ are cytosolic, however two splice variants from subtype 2, β2a and β2e, are targeted to the plasma membrane even in the absence of $Ca_V\alpha_1$ (Chien et al. 1995, Dolphin 2003, Hidalgo and Neely 2007, Miranda-Laferte et al. 2014, Neely and Hidalgo 2014). $Ca_V\beta2$ is the most prominent isoform in mice and human embryonic as well as adult heart cells. Here we compare the effect of a membrane anchored $Ca_V\beta$ (β2a) with the effect of a cytosolic $Ca_V\beta$ (β2b) on $Ca_V1.2$ intracellular transport.

$Ca_V\beta$ binds to a highly conserved sequence in the I–II linker of the poreforming subunit, the so-called α-interaction domain (AID) (Hidalgo et al. 2006, Pragnell et al. 1994). The crystal structures of three $Ca_V\beta$ isoforms alone and in complex with the AID site has been solved.

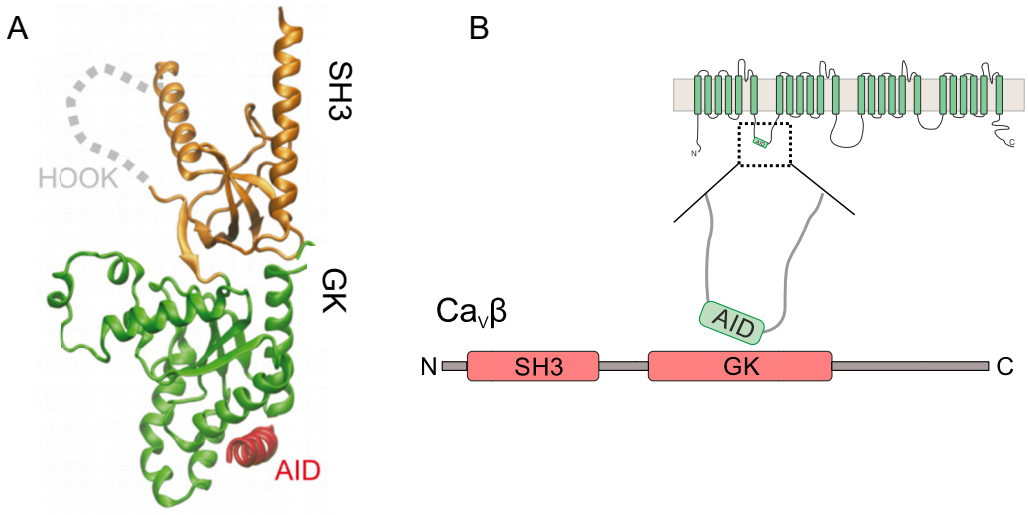

Figure 1.5: Crystal structure (A) and scheme of the domain organization (B) of Ca$_V$β. Ca$_V$β encompasses five distinct regions, two domains, highly conserved among all Ca$_V$β isoforms, a Src homology 3 (SH3)-domain and a guanylate kinase (GK)-domain. With the GK-domain Ca$_V$β binds to the α-interaction domain (AID) a highly conserved sequence in the I–II linker of the poreforming subunit.

These studies revealed that Ca$_V$β encompasses two highly conserved domains, one homologous to the Src homology 3 (SH3) domain and the other one to the guanylate kinase (GK) domain. SH3 and GK are found in all members of the membrane-associated guanylate kinase (MAGUK) family of proteins (Buraei and Yang 2010, Chen et al. 2004, Opatowsky et al. 2004a, Van Petegem et al. 2004) (Figure 1.5). Both domains function as protein-protein interaction modules. The structure showed that the GK-domain contributes to the association with the AID site (Figure 1.5). The SH3 domain lies opposite to the association interface within AID and GK and appears available for further protein-protein interactions (Mayer 2001).

The association of Ca$_V$β with Ca$_V$α$_1$ regulates the biophysical properties and the cell surface expression of the calcium channel. It has been well established that Ca$_V$β is required for the release of Ca$_V$α$_1$ from the endoplasmic reticulum (Fang and Colecraft 2011, Hidalgo and Neely 2007) and three models have been proposed for the action of Ca$_V$β: i) association of Ca$_V$β with channels in the ER unmasks an ER retention signal located in the I-II loop nearby the AID site (Bichet et al. 2000); ii) binding of Ca$_V$β exposes an export signals on the I–II loop that overcome the effect of retention signals on other cytoplasmic regions (Fang and Colecraft 2011) and iii), Ca$_V$β impairs the ubiquitination and targeting of ER-retained channels to the ER-associated degradation (ERAD) pathway (Altier et al. 2011).

In addition of this $Ca_V\beta$ can affect the trafficking of $Ca_V\alpha_1$ indirectly by interacting with other proteins involved in calcium channel regulating processes like through downregulation of the transport by binding to individual members of the RGK family of Ras-related GTPases e.g. Kir/Gem (Beguin et al. 2005, Beguin et al. 2001, Campiglio and Flucher 2015) or through direct interaction with actin filaments (Stolting et al. 2015). Moreover $Ca_V\beta$ can induce endocytosis of the channel through interaction with dynamin, a small GTPase involved in receptor-mediated endocytosis (Gonzalez-Gutierrez et al. 2007, Miranda-Laferte et al. 2011).
At the level of the plasma membrane it has been shown that association of $Ca_V\beta$ with $Ca_V\alpha_1$ is reversible and the association occurs in an one-to-one stoichiometry (Dalton et al. 2005, Hidalgo et al. 2006). However, whether these subunits dissociate after $Ca_V\alpha_1$ exits the ER during the journey to the plasma membrane and from the cell surface remains elusive. This question is addressed in my thesis.

1.2 Transport of proteins

Surface expression of membrane proteins requires their movement from their place of synthesis, the endoplasmic reticulum, through the Golgi apparatus, to their final destination, the plasma membrane. The number of channels in the plasma membrane is ultimately determined by the balance between the channel´s anterograde (biosynthetic forward) and retrograde (backward) trafficking (Figure 1.6).

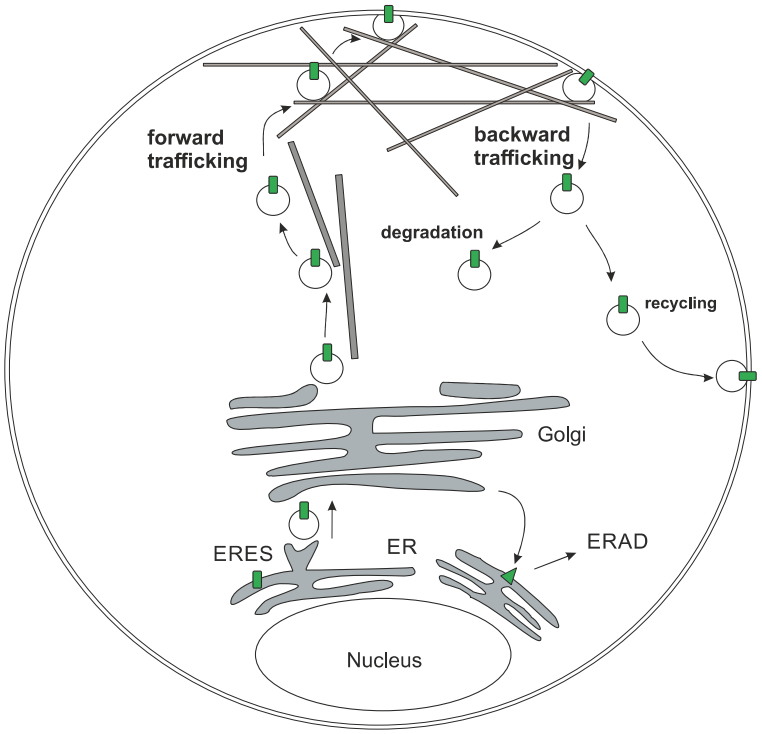

Figure 1.6: Trafficking pathway of membrane proteins. Channels are transported forward from their place of synthesis, within the endoplasmic reticulum, towards the plasma membrane. To balance the number of channels within the membrane, they can be internalized and brought backward either on a recycling or a degradation pathway.

1.2.1 Biosynthetic forward transport – from synthesis to the final sorting

As for all membrane proteins, the translation of calcium channels takes place in a perinuclear region at the ribosomes attached to the ER and from this place of synthesis they have to be actively transported to the plasma membrane.

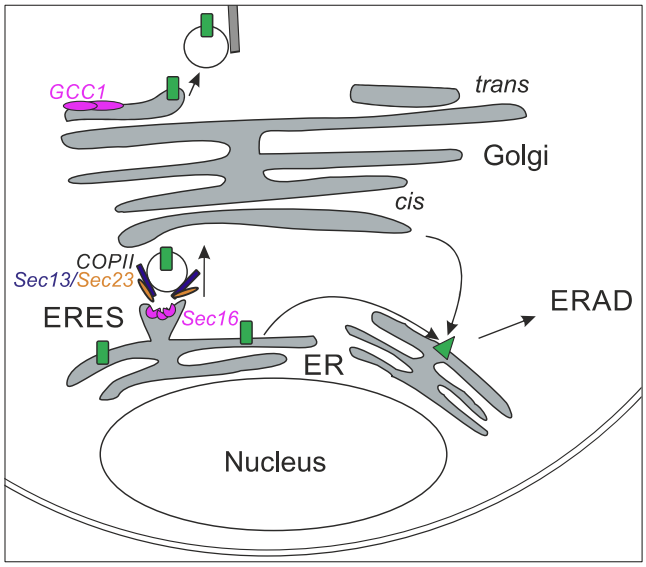

Figure 1.7: Biosynthetic forward transport. Membrane proteins, synthetized at the endoplasmic reticulum (ER) are either degraded by the ER associated degradation pathway (ERAD) or released from ER exit sites, marked by Sec16-proteins that associated with COPII-subunits, coating the vesicle. Membrane proteins are transported over the Golgi-system (*cis* to *trans,* GCC1 as marker protein) and left it packed in vesicles towards the plasma membrane.

The newly synthetized membrane protein is translocated into the membrane of the endoplasmic reticulum (ER) as the first step in the process that deliver these proteins to the secretory pathway and thereby initiating their journey to the plasma membrane (Braakman and Bulleid 2011, Rapoport 2007, Walter and Johnson 1994). The ER provides a quality control checkpoint which in general only allows secretion of proteins that are folded and modified correctly (Braakman and Bulleid 2011). Misfolded proteins are retained in the ER where they may be subsequently sent for the ER-associated degradation (ERAD) pathway. Alternative, proteins can be brought back, after translocation to the Golgi complex, from the *cis*-Golgi to the ER to be degraded by ERAD (Kincaid and Cooper 2007, Vashist et al. 2001) (Figure 1.7). In both cases they are targeted for retranslocation back into the cytosol, become ubiquitinated and finally degraded by the ubiquitin-proteasome system (Claessen et al. 2012, Olzmann et al. 2013, Ruggiano et al. 2014). Fully matured proteins are packed as cargo proteins into COPII (coat-protein-complex II) coated transport vesicles which bud off from the ER exit sites (ERES) prior to fusion with the *cis*-Golgi complex (Budnik and Stephens 2009). The location of ER exit sites can be shown by the peripheral membrane protein Sec16, which interacts physically with the COPII subunits Sec23 and Sec13 and therefore provides a platform for the COPII assembly (Bhattacharyya and Glick 2007, Hughes et al. 2009).

From the Golgi the proteins continue through to the *medial*- and *trans*-Golgi compartments where they are further modified and sorted for delivery (Nakano and Luini 2010, Smyth and Shaw 2010) (Figure 1.7). It is suggested that microtubules are required for translocation of proteins from the ER to the Golgi (Caviston and Holzbaur 2006, Watson et al. 2005).
Membrane proteins are packed into vesicles that move directionally through the cytoplasm to finally fuse with the plasma membrane. The transport of vesicles is done by motor proteins that move directionally along cytoskeletal tracks from the Golgi, which is known to be tightly associated with the cytoskeleton (Egea et al. 2006, Egea et al. 2013). The cytoskeletal tracks are the intracellular highways by which proteins packed into vesicles are deliveed to their destinations.

1.2.2 Endocytotic backward pathway – recycling or degradation?

Regulation of the composition of the plasma membrane is a critical component of the physiological response and endocytosis plays a crucial role in regulating this process. Endocytosis is the transport of cargo from the plasma membrane to the cell interior. It starts with the invagination of the plasma membrane and pinching off an endocytic vesicle or endosome that contains ingested substances and associated membrane proteins. Endocytosis occurs by various mechanisms, which can be divided into those that are clathrin dependent and those that are clathrin independent (Grant and Donaldson 2009). Clathrin is a three-legged triskelion protein that forms vesicle coats by coassembly with adaptor proteins (Kirchhausen 2000, Traub 2009). In clathrin-dependent endocytosis ligands bind to specific cell surface receptors of plasma membrane proteins, are packed into clathrin-coated vesicles and brought into the cell interior (Doherty and McMahon 2009). F-actin dynamics are needed at multiple stages of clathrin-coated vesicle formation (Merrifield et al. 2005, Yarar et al. 2005) suggesting that actin may have coordinated functions during endocytosis.
Clathrin-independent endocytosis uses an alternative protein coat or does not require protein coating for the formation of endocytic vesicles (Doherty and McMahon 2009, Ivanov 2008) Caveolae or lipid rafts invaginations within the membrane, both enriched in structural sterols, are found to mediate those endocytic processes (Grant and Donaldson 2009, Lingwood and Simons 2010, Mayor and Pagano 2007, Samaj et al. 2004).
The large GTPase dynamin is a critical regulator of both clathrin-dependent and -independent endocytosis, because it regulates formation and scission of the newly formed endocytic vesicles (Hinshaw 2000, Lanzetti 2007, Merrifield et al. 2002).

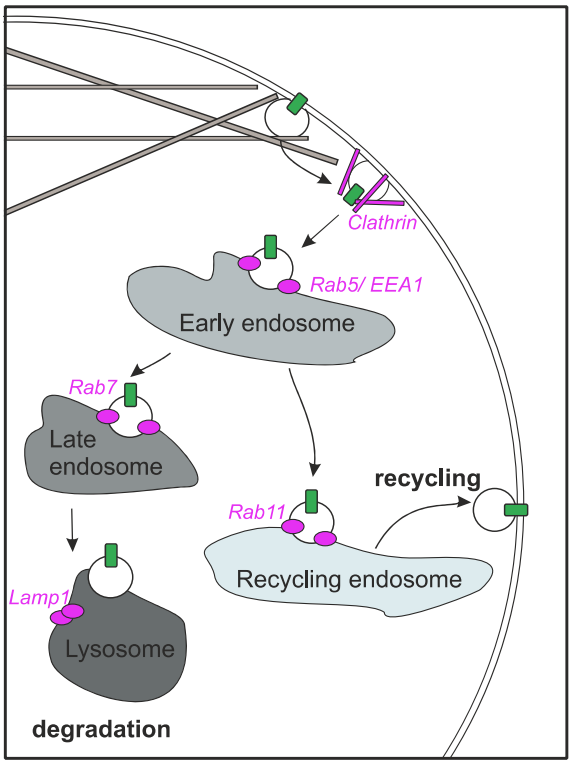

Figure 1.8: Endocytotic backward pathway. Internalized clathrin-coated vesicles fuse with the early endosome (Rab5 or EEA1), and then can be either transported to late endosome (Rab7) and further on the degradational route to lysosomes (Lamp1) or on the recycling pathway to the recycling endosome (Rab11) for reinsertion in the plasma membrane.

It has been has been reported by our group that dynamin is involved in the endocytosis of voltage-activated calcium channels (Gonzalez-Gutierrez et al. 2007). Internalized vesicles fuse with early endosomes which serve as the major sorting station of the endocytic pathway (Figure 1.8). From there molecules are sorted into degradational or recycling pathway (Jovic et al. 2010, Steele and Fedida 2014).

Endosomal trafficking is regulated by a group of over 60 small monomeric GTPases known as the Rab GTPases (Mizuno-Yamasaki et al. 2012) (Figure 1.8). They cycle between active vesicle-associated GTP-bound and inactive free cytoplasmic GDP-bound states. Recruitment of effector proteins in the active state enables Rabs to control the main steps in vesicular trafficking processes including budding, tethering, delivery and fusion of membrane vesicles (Mizuno-Yamasaki et al. 2012). Different Rab proteins are localized to specific intracellular domains and can therefore act as markers for specific endosomes (Stenmark 2009, Zerial and McBride 2001) (Figure 1.8). Rab5 marks the early endosome and colocalizes with the early

endosomal antigen 1 (EEA1) (Mu et al. 1995). From the early endosome proteins that are sorted for recycling are directly transported to the plasma membrane by vesicular transport or indirectly via a Rab11-dependent recycling endosomes (Maxfield and McGraw 2004). Proteins that undergo the degradational route are sorted by Rab7 to late endosomes which finally fuse with lysosomes where protein degradation occurs (Ohashi et al. 2011). Members of the Rab-family have been shown to interact with motor proteins, dyneins and kinesins (Horgan and McCaffrey 2011) as well as myosins V and VI (Desnos et al. 2007, Seabra and Coudrier 2004), which function in the cytoskeletal trafficking.

1.2.3 The cytoskeleton as vesicular highway

Every eukaryotic cell is shaped by a complex network of interlinking filaments which form a three dimensional meshwork. However, the cytoskeleton is not a fixed but rather a dynamic and adaptive structure (Alberts 2008, Fletcher and Mullins 2010). According to the current demand of the cell the protein filaments can be synthetized, removed and rebuild. With this constant flux these polymers control the shape and mechanics of cells, spatially organize their contents and finally enable the cell to move. The network of filaments consists of three major classes of cytoskeletal polymers: actin microfilaments, microtubules and intermediate filaments. Motor proteins which moves along the filaments of the cytoskeleton, promotes the transport of substances and particles (cargo) throughout the cell (Alberts 2008, Fletcher and Mullins 2010). This cargo transport takes place along actin filaments and microtubules that as a result of their structural polarity due to polarized polymers is directional (Ross et al. 2008). Intermediate filaments, which provide the mechanical strength of a cell, are not polarized and cannot support directional movement of molecular motors (Herrmann and Aebi 2000). The motor proteins dynein and kinesin are moving along microtubules and myosin moves along actin filaments. A graphical scheme of the vesicular transport along the cytoskeletal network is shown in Figure 1.9.

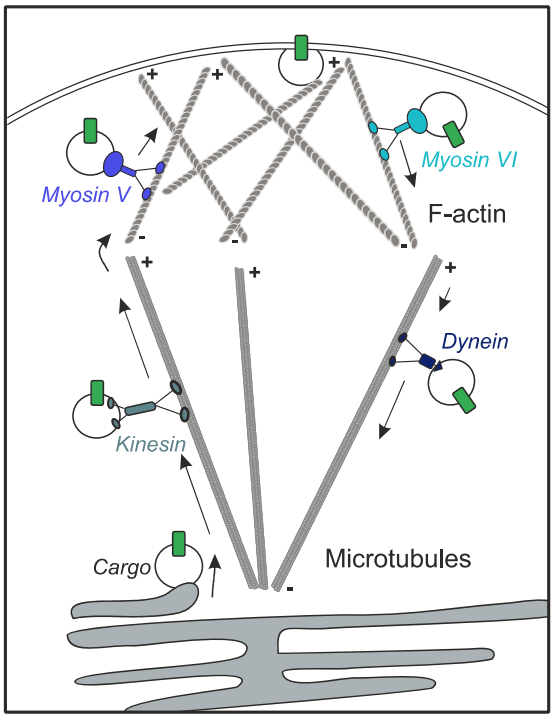

Figure 1.9: Vesicular transport along the cytoskeletal network. During the protein transport, vesicles including membrane proteins (cargo) are moved by motor proteins along polarized filaments. Long-range transport along microtubules takes place by kinesins towards the plasma membrane (in plus-end direction) and by dyneins in the inner of the cell (in minus-end direction). Along F-actin myosin V transports cargo outwards to the surface (plus-end direction) and myosin VI inwards (minus-end direction).

1.2.3.1 Actin filaments

Actin filaments are two-stranded helical polymers of the protein actin with a diameter of 5-9 nm which exists in two principal forms, globular, monomeric (G-actin), and filamentous polymeric (F-actin). The filaments are dispersed throughout the cell but most highly concentrated in the cortex beneath the plasma membrane (Alberts 2008). Actin filaments possess an inherent polarity, with a general distribution of plus ends located at the cell membrane (Figure 1.9). During polymerization monomers are rapidly added to the filament at its plus end. The motor proteins belonging to the myosin family are responsible for vesicular trafficking processes along F-actin (Lanzetti 2007, Semenova et al. 2008, Smyth et al. 2012). Myosin motor proteins use ATP-hydrolysis-mediated conformational changes to move along actin filaments. The members myosin V and VI are known to be involved in membrane transport of vesicle or protein cargoes in mammalian cells (Krendel and Mooseker 2005, Mehta et al. 1999, Seabra and Coudrier 2004). Myosin V walks towards the plus end of cortical actin filaments (Langford 2002), whereas myosin VI moves along actin filaments to

the minus end (Wells et al. 1999) (Figure 1.9). This movement from the plasma membrane towards the cell interior implicates a role of myosin VI in trafficking during endocytosis of membrane proteins (Altman et al. 2007, Aschenbrenner et al. 2004, Chibalina et al. 2007, Dance et al. 2004).

1.2.3.2 Microtubules

Microtubules are long, straight, hollow cylinders with an outer diameter of 25 nm, built from α-tubulin and β-tubulin heterodimers. They are polarized with minus ends attached to a perinuclear microtubule-organization center (MTOC) radiating with the plus ends to the cell boundary (Alberts 2008, Hale et al. 2011, Jordan and Wilson 2004) (Figure 1.9).

Microtubules serve as tracks for members of two families of motor proteins, the kinesins and dyneins. Kinesins use the chemical energy of ATP to drive conformational changes that generate motile force for anterograde transport of cellular cargo and therefore are involved in long-range transport toward the cell surface (Hirokawa et al. 2009) whereas dynein is a minus-end-directed motor and mediates movement towards the cell interior (Roberts et al. 2013, Vale 2003). Due to this, dynein is thought to facilitate the inward movement of endocytotic vesicles from early to late endosome (Aniento et al. 1993, Flores-Rodriguez et al. 2011).

1.3 Movement of particles

The interior of a cell is a compilation of separate intracellular compartments organized in a liquid matrix, the cytosol that performs most of the intermediary metabolism. The cytosol includes more than the half of the cell's cytoplasm and all synthesized proteins and macromolecules have to move through it, covering micrometer distances, to reach their target location (Alberts 2008). This complex and volume-occupied solution environment leads to a macromolecular crowding within the cell that imposes constraints to the transport of molecules inside the cell (Ando and Skolnick 2010, Luby-Phelps 2000). Diffusion by itself does not explain the directionality of such transport process and long-range movements are mainly achieved by the active transport mediated by the motor proteins along cytoskeletal components.

1.3.1 Normal diffusion and directed motion

Particles suspended in fluids show a continual random displacement due to collision with fast-moving molecules in the surrounding solvent. This transport phenomenon is called 'Brownian motion', after the botanist Robert Brown (1827). It describes a so called normal diffusion based on random movements. For a huge number of particles located within the same space the Brownian motion leads to a spreading of a particle over time from one region of space to another (Hall and Hoshino 2010). Because the Brownian motion is a stochastic process, on average the particles go nowhere. In a system with a concentration gradient the molar flux of a solute due to diffusion is described by Fick's law and it is proportional to the concentration gradient using a constant coefficient of diffusion (Dix and Verkman 2008).

In the absence of a concentration gradient, normal diffusion is usually described by Einstein's equations of Brownian motion (Einstein 1905). Albert Einstein linked the diffusion coefficient utilized by Fick to Browns observations with regard to the system properties governing the individual spherical particle displacement over time intervals (Hall and Hoshino 2010).

The mean square displacement (MSD) of the particles over time can then be set proportional to the diffusion coefficient. For Brownian diffusion the MSD of a particle increases linearly with time according to the following equation:

$$MSD(t) = 2nDt \tag{1}$$

where D is the diffusion coefficient and n the number of dimensions. For a particle in three dimensional space the formula is:

$$MSD(t) = 6Dt \tag{2}$$

Due to this characteristic the MSD value is used to characterize complex dynamical processes in biological systems. The MSD is defined as the square of the displacement of a particle in three dimensions over a specific time interval, averaged over the available time points:

$$MSD(t) = \frac{1}{N-t}\sum_{i=1}^{N-t}((x_i - x_{i+t})^2 + (y_i - y_{i+t})^2 + (z_i - z_{i+t})^2) \tag{3}$$

where *N* is the total number of frames and *t* is the frame interval (Michalet 2010).

Equation 2 is a model, which describes a motion in a homogeneous solvent. In inhomogeneous environments, e.g. in the crowded cell cytoplasm with fixed or mobile obstacles, more complex equations are necessary to describe the movement of particles. This type of diffusion is designated as anomalous diffusion (Dix and Verkman 2008) and its mean square displacement does not increase linearly with time (Equation 4). After Bouchaud and Georges (1990) the diffusion of a particle moving among various traps is described as:

(4) $$MSD(t) = 6Dt^{\alpha}$$

The value of α defines the deviation from normal diffusion which corresponds to a value of one. If $0 < \alpha < 1$ the MSD curve lies below normal diffusion and is called anomalous subdiffusion and if $1 < \alpha \leq 2$ the MSD values fall above the ones obtained for normal diffusion and is known for anomalous superdiffusion (Figure 1.10). In both cases the respective particle does not move freely but is restricted or accelerated by a variety of active transport processes (Bouchaud and Georges 1990, Dix and Verkman 2008).

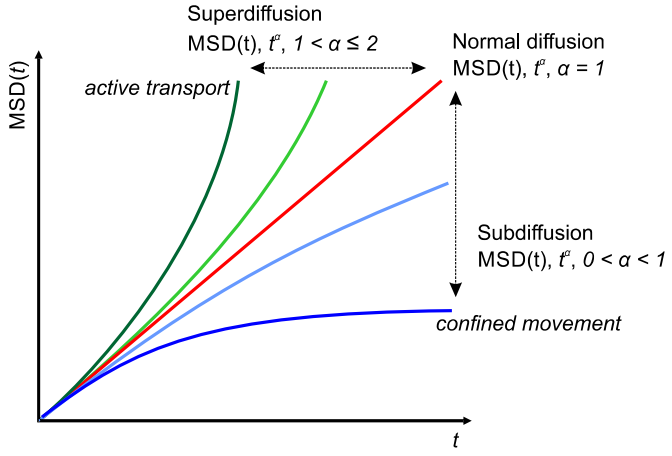

Figure 1.10: MSD curves of different types of motion. The type of motion as well as the corresponding α-exponent is indicated for each line graph. The red line corresponds to a normal diffusion. In blue and green the types of anomalous diffusion are shown for subdiffusion and superdiffusion, respectively. The lowest mean square displacement of a moving particle is defined as confined movement and the highest as active transport. Graphic modified after Ruthardt et al. (2011).

Anomalous subdiffusion describes the decreasing diffusive movement of cytoplasmic macromolecules in a maze-like environment where the molecular mobility is reduced due to the concentration of obstacles in the crowded solution (Banks and Fradin 2005, Saxton 1993, Weiss et al. 2004). This renders the particles a confined diffusion due to the high crowded environment and its behavior is reflected by a flat MSD curve.

The superdiffusional movement comes about by an external force that results in increased MSD of the particle as compared with normal diffusion (Saxton 2009). For the intracellular movement of vesicles this implies the movement driven by motor proteins along cytoskeletal tracks. If $\alpha = 2$ the particle is only moved by active transport. However it is known that transition may occur between these different types of motion (Neri et al. 2013, Saxton 2008).

1.3.2 Single particle tracking

Single particle tracking (SPT) allows determining the position of a particle at any given time and, thus, the determination of MSD curves (Hall and Hoshino 2010). This technique involves the selective labelling of individual proteins with fluorophores such as fluorescent proteins or organic dyes to follow their movements with high temporal and spatial resolution when using fast imaging techniques (Saxton and Jacobson 1997).

This can be done for instance with spinning disk laser confocal microscopy that permits the fast imaging of living cells with low exposition times, and therefore low cytotoxicity. Based on a rotating pinhole disk, multiple spots on the sample are scanned simultaneously. Because the cells can be imaged at different focal planes over time the use of spinning disk imaging associated with the single particle tracking analysis provide a suitable tool to study the transport dynamics of heterogeneous systems (Dupont et al. 2013, Nakano 2002). The quantitative analysis of trajectories obtained by connecting the determined position of individual particles at consecutive time points allows the characterization of the type of movement for that particle (Sbalzarini and Koumoutsakos 2005).

Various implemented algorithms have been developed to extract the position of fluorescently labelled molecules, heterologously expressed inside the cell, from merged images of all focal planes (z-stack) (Jaqaman et al. 2008, Kalaidzidis 2007, Lund et al. 2014, Ruthardt et al. 2011, Sbalzarini and Koumoutsakos 2005, Woll et al. 2013). Nevertheless, the general procedure for particle detection is shared by the different algorithms and it can be divided in two steps. In the first step the fluorophores are localized within all frames of the three-dimensional stack of images over time by detection of intensity peaks. Hereafter a tracking

step follows in which all detected objects found in step one are connected from frame to frame for calculating the corresponding trajectories (Saxton 2009) (cf. Figure 3.38). Both steps are challenging tasks due to the high particle density and background fluorescence, and optimization of the acquisition conditions, including expression system is of central importance. At high particle densities fast particles become difficult to connect to the local nearest-neighbor, because particle may appear, disappear or merge (Serge et al. 2008). Therefore trajectories may merge or split with trajectories from different particles. This problem can be solved in heterologous cell systems by adaption of the amount of proteins being expressed. The other challenge is to find the suitable brightness of the fluorophores. On the one hand the fluorescence must not be too high in order to avoid background threshold and failed detection, but on the other hand they have to be bright and photostable enough to be detected during a time-lapse record (Cole 2014). So the selection of an appropriate fluorescence protein is of high importance (Shaner et al. 2013, Shaner et al. 2005). All this optimization where done during my studies. To interpret individual dynamics of the resulting trajectories each trajectory is analyzed separately. Various parameters describing particle's motion, including displacement length, average speed and diffusion coefficients can be calculated from the positions of the particle at any given time point.

2 Materials and methods

2.1 Molecular biology

For heterologous expression of proteins in mammalian cells, the cDNA encoding the protein under study was subcloned preserving the proper reading frame into a destination vector by standard molecular biology techniques.

2.1.1 Vectors

For protein expression in HEK293 or Flp-In T-REx cells, several vectors were used (Table 2.1):

Table 2.1: Vectors used in this project.

Vector	Resistence	Origin	Promotor
pcDNA3.1 (+)	ampicillin/neomycin	SV40	CMV immediate early promoter
pcDNA3.1 (-)	ampicillin/neomycin	SV40	CMV immediate early promoter
pEYFP-N1	kanamycin/neomycin	SV40	CMV immediate early promoter
pEGFP-N1	kanamycin/neomycin	SV40	CMV immediate early promoter
pcDNA5/FRT/TO	ampicillin/hygromycin	SV40	CMV immediate early promoter

2.1.1.1 pcDNA3.1 (+) and pcDNA3.1 (-)

pcDNA3.1 (+) and pcDNA3.1 (-) vectors are high-level expression vectors in mammalian cells. They include the strong and ubiquitously active human cytomegalovirus immediate-early (CMV) promoter. A multiple cloning site in forward (+) or reverse (-) orientation is completed by a polyadenylation signal for enhanced mRNA stability. Its origin is SV40. Neomycin and ampicillin resistance genes can be used for transformants selection.

2.1.1.2 pEYFP-N1

The vector pEYFP-N1 is used for fusing EYFP to the C-terminus of a target protein. It encodes an enhanced yellow-fluorescent variant of the *Aequorea Victoria* green fluorescent

protein (GFP) that was genetically modified to incorporate amino acids substitutions at four positions (S65G, V68L, S72A, T203Y). The excitation maximum is at 513 nm and the emission spectrum has a peak at 527 nm. The vector contains a CMV promotor, a SV40 origin and a neomycin as well as a kanamycin resistance gene for transformants selection.

2.1.1.3 pEGFP-N1

The pEGFP-N1 vector encodes the fluorescent protein EGFP. It was used for fusing EGFP to the C-terminus of the protein under study. It encodes a red-shifted GFP mutant1 variant of wild-type GFP (excitation maximum = 488 nm; emission maximum = 507 nm). It contains the double-amino-acid substitution of F64L and S65T and has been optimized for brighter fluorescence in mammalian cells. The vector contains a CMV promotor. Its origin is SV40. Neomycin and kanamycin resistances genes can be used for transformants selection.

2.1.1.4 pcDNA5/FRT/TO

The pcDNA5/FRT/TO vector also has a CMV promoter for high expression in mammalian cells. Additionally, it includes a flip-in recombinase site for gene integration in Flp-In T-REx host cell genome, as well as ampicillin and hygromycin resistance genes for selection. This vector was used for inducible expression of the $Ca_V\beta$ under the control of tetracycline.

2.1.2 Construction of plasmids

The Software VectorNTI (InforMax Inc) was used to design cloning strategies and analyse cDNA and protein sequences. For inserting the gene of interest into a desired vector, the coding region of the gene was amplified by polymerase chain reaction (PCR) and purified. To insert the PCR product into the recipient plasmid, both double stranded cDNAs are digested with the same restriction enzymes in order to generate compatible ends that facilitate covalently ligation of vector and gene of interest. The ligation mix was introduced into recombinant bacteria by transformation, purified and finally used for transfection of mammalian cells.

2.1.3 Polymerase chain reaction (PCR)

The PCR method was applied to amplify the gene of interest and to incorporate restriction sites compatible with the desired destination vector. The PCR was carried out with the KOD Hot Start DNA Polymerase Kit (Merck Millipore) according to the manufacturer's protocol.

The PCR mixture was composed as follows:

Table 2.2: Composition of the PCR reaction mixture.

Component	Volume	Final Concentration
10X Buffer for KOD Hot Start DNA Polymerase	5 µl	1X
25 mM $MgSO_4$	3 µl	1.5 mM
dNTPs (2 mM each)	5 µl	0.2 mM (each)
H_2O bidest	ad 50 µl	
Sense Primer (10 µM in H_2O)	1.5 µl	0.3 µM
Antisense Primer (10 µM in H_2O)	1.5 µl	0.3 µM
Template DNA (10 ng)	10 ng	
KOD Hot Start DNA Polymerase (1 U/µl)	1 µl	0.02 U/µl
Total volume	50 µl	

The following temperature cycles were used during the PCR reaction. The annealing temperature was modified according to the primers used:

Table 2.3: Thermocycling conditions for PCR.

Step		Temperature	Time
	Polymerase activation	95°C	2 min
40 Cycles:	Denaturation	95°C	20 s
	Annealing	57°C – 61°C	20 s
	Extension	70°C	50 s
	Hold	8°C	

After the PCR was terminated, the PCR products were purified using the NucleoSpin Gel and PCR Clean-up Kit (Macherey-Nagel) according to the manufacturer's instructions. The PCR fragment was eluted, subjected to restriction digestion and stored in H_2O until use. The following table presents the primers used in this project:

Table 2.4: List of primers used for cloning processes.

Number	Primer	Direction
1	AAAAAAACCGGTAATGCAGTGCTGCGGGCTGGT	sense
2	AAAAAAACCGGTCCTTGGCGGATGTATACATCCC	antisense
3	AAAAAAACCGGTAATGGTGAGCAAGGGCGAGGAGGA	sense
4	AAAAAATCTAGATTACTTGTACAGCTCGTCCATG	antisense
5	CTGGCTAGCGTTTAAACTTAAGCT	sense
6	GTACCGATTTCGGATCCCATCTGCATCTCATCGAAGTTGA	antisense
7	TCAACTTCGATGAGATGCAGATGGGATCCGAAATCGGTAC	sense
8	TCGAACGTGCTCCTCCGGGTCAGCGTGCTCAGCCAGCGCG	antisense
9	CGCGCTGGCTGAGCACGCTGACCCGGAGGAGCACGTTCGA	sense
10	CTTGCATTCAGCCTCAGTCTGTTTGG	antisense
11	CTGGCTAGCGTTTAAACTTAAGCT	sense
12	CTTGCATTCAGCCTCAGTCTGTTTGG	antisense
13	GGTGGGAGGTCTATATAAGC	sense
14	CATCCTCATTCTCAGGGTCGATGTCCTTCTCCCGCAACTTCT GGAAATCT	antisense
15	AGATTTCCAGAAGTTGCGGGAGAAGGACATCGACCCTGAG AATGAGGATG	sense
16	AACACACACTGAACCACGTGCTTT	antisense
17	GGTGGGAGGTCTATATAAGC	sense
18	AACACACACTGAACCACGTGCTTT	antisense
19	AAAAAAAAGCTTATGCAGTGCTGCGGGCTGGTACAT	sense
20	AAAAAAGGATCCCTTGTACAGCTCGTCCATGCCGCC	antisense
21	AAAAAAAAGCTTATGCTGGATCGCCAGCTGGTGAGC	sense
22	AAAAAAGGATCCAGCACCAGTTGAGTGGCGGCCCTC	antisense

2.1.4 Restriction digestion

To insert the PCR product into the recipient plasmid, both double stranded cDNAs are digested with the same restriction enzymes that recognize specific palindromic DNA sequences of 4-8 base pairs and hydrolyze the covalent bond between base pairs. Short complementary single stranded hanging ends, the so called sticky ends, are generated that

promote ligation using a Ligase enzyme. Restriction reactions were done in a total volume of 30 µl or 10 µl for preparative or analytical analysis, respectively (Table 2.5). Restriction digestions were carried out for 30-60 min at 37°C. All FastDigest restriction enzymes and the reaction buffers were purchased from ThermoScientific.

Table 2.5: Composition of the restriction digestion mixture

Component	Analytic	Preparative
FastDigest Enzyme I	0.2 µl	1 µl
FastDigest Enzyme II	0.2 µl	1 µl
10X FastDigest Green Buffer	1 µl	3 µl
Plasmid DNA	1 µg	3 µg
H_2O bidest	ad 10 µl	ad 30 µl
Total volume	**10 µl**	**30 µl**

For further usage of the restricted DNA fragments or in order to control their size, all restriction digestion mixtures were separated by gel electrophoresis.

2.1.4.1 Separation of nucleic acids in agarose gels

Gel electrophoresis is a simple method to separate and analyze nucleic acids. Depending on its length linearized DNA fragments from the digestion mix were separated by the sieve function of the agarose gel matrix, while applying an electric field. The percentage of agarose amount within the gel determines the minimal size of DNA fragments which can be separated. Since the size of the DNA fragments and vectors, generated in this project ranges between 700 bp and 8000 bp, 1 % - 1.5 %-agarose gels were used for their separation. DNA samples were electrophoretically separated for 20 min at 120 V in TAE buffer. To visualize DNA bands fresh molten agarose was mixed with SYBR Safe DNA Gel Stain (1X; Invitrogen). This transilluminator intercalates into nucleic acids and can be detected at 530 nm, after exciting at 280 nm using the Biorad Gel DocTM XR+ System (Bio-Rad, Munich). The size of the separated DNA fragments was estimated by comparison with the DNA ladder λ DNA/ EcoRI+HindIII Marker (ThermoScientific) or the DNA ladder GeneRuler 1 kb (ThermoScientific) molecular mass markers using.

2.1.4.2 Isolation of DNA fragments from preparative agarose gels

After gel electrophoresis, the desired DNA fragments were isolated by excising the respective DNA-bands from the agarose gel (visualized with UV light using the Biorad Gel DocTM XR+ System (Bio-Rad)) using a razor blade. The DNA was purified from the agarose gel using the NucleoSpin Gel and PCR Clean-up (Macherey-Nagel) according to the manufacturer's instructions. The DNA was eluted with H_2O and used for further cloning steps.

2.1.5 Ligation of DNA fragments

In order to produce a vector bearing the gene of interest, the restricted and cleaned PCR product was covalently linked to a compatibly digested vector backbone using the T4 DNA ligase. This enzyme catalyzes the formation of covalent phosphodiester linkages. After ligation, the inserted DNA is physically attached to the backbone and the complete plasmid can be transformed into bacterial cells for propagation.

The process of the ligation was carried out using the Rapid DNA Ligation Kit (ThermoScientific) according to the manufacturer's instructions. In molar ratio, three DNA fragments of the insert are mixed with one fragment of template vector, 5X Rapid Ligation Buffer and T4 DNA Ligase (Table 2.6) and incubated for 5 min at 22°C. For correct determination of the necessary amount of insert DNA the ligation calculator from the University of Düsseldorf (http://www.insilico.uni-duesseldorf.de/Lig_Input.html) was used.

Table 2.6: Composition of DNA ligation mixture.

Component	Volume/Amount
Linearized vector DNA	50 ng
Insert DNA (at 3:1 molar excess over vector)	
5X Rapid Ligation Buffer	4 µl
T4 DNA Ligase, 5 U/µl	1 µl
H_2O bidest	ad 20 µl
Total volume	**20 µl**

After ligation was done the mix was transformed into bacteria for further amplification of the plasmid. Antibiotic selection was used for selecting the transformed bacteria.

2.1.6 Transformation of TOP 10 F competent cells

For transformation, 50 µl of competent TOP 10 F cell suspension (Invitrogen) were mixed with 5 µl of plasmid DNA and incubated on ice for 20 min. After a heat shock at 42°C the suspension was again incubated on ice. After 10 min, 200 µl LB medium was added, followed by a 45 min incubation period at 37°C while shaking. Then cells were plated on LB agar containing the required antibiotics and incubated overnight at 37°C.

Table 2.7: Composition of LB media and LB agar.

	Substance	Final concentration
LB media:	NaCl	10 g/l
	tryptone	10 g/l
	yeast extract	5 g/l
LB agar:	NaCl	10 g/l
	$MgSO_4 \cdot 7H_2O$	2 g/l
	NZ amine	10g/l
	yeast extract	5 g/l
	agarose	7.5 g/l

Colonies were picked and incubated in 5 ml LB-medium in presence of the required antibiotics for Mini preparation. Amplified vectors were isolated with Kits for plasmid recovery.

2.1.7 DNA isolation from bacterial cultures

For plasmid DNA purification, different Kits were used, depending on the culture volume of the bacterial culture. For Mini preparation, the NucleoSpin Plasmid Kit from Macherey-Nagel and for HiSpeed Plasmid Maxi Quiagen Kits were used following manufacturers' instruction. DNA was eluted in H_2O when used for further processing and in TE buffer when stored for longer time.

The concentrations of the purified vectors were measured with the NanoDrop photometer (NanoDrop 2000, ThermoScientific).

After vector recovery, size and quality of the purified DNA was checked by a control restriction (cf. 2.1.4). If the DNA showed the right band pattern after enzymatic restriction and agarose gel electrophoresis, the vector was sequenced.

2.1.8 Sequencing

The identity of the newly synthetized cDNAs was verified by DNA sequence analysis. Sequencing was performed by eurofins Genomics (Ebersberg, Germany).

2.1.9 Construction of a concatamer including $Ca_V1.2$ and $Ca_V\beta$ subunits

In order to express stochiometrically $Ca_V1.2$ and $Ca_V\beta$ subunits, a new plasmid was generated in which $Ca_V\beta$ coding region was covalently linked to the carboxyl terminus of $Ca_V1.2$. To select transformants the $Ca_V1.2$-$Ca_V\beta$ concatamer was followed by EYFP fluorescence protein. To engineer this concatamer construct a plasmid containing $Ca_V1.2$ in frame with an EYFP at the C-terminus was cut between $Ca_V1.2$ and EYFP (cf. 2.1.4). For placing the DNA encoding for $Ca_V\beta2a$ in this gap suitable restriction sites were inserted by PCR using the primers 1 and 2 (cf. Table 2.4). TOP 10 F competent cells were used to propagate the new plasmid (cf. 2.1.6).

2.1.10 Modification of the fluorescence tag of $Ca_V1.2$ subunit

To visualize the intracellular trafficking of $Ca_V1.2$ by fluorescence microscopy the protein was tagged either with a fluorescence protein covalently linked or with an epitope-tag able to bind fluorescent ligands, such as HaloTag-Ligands.

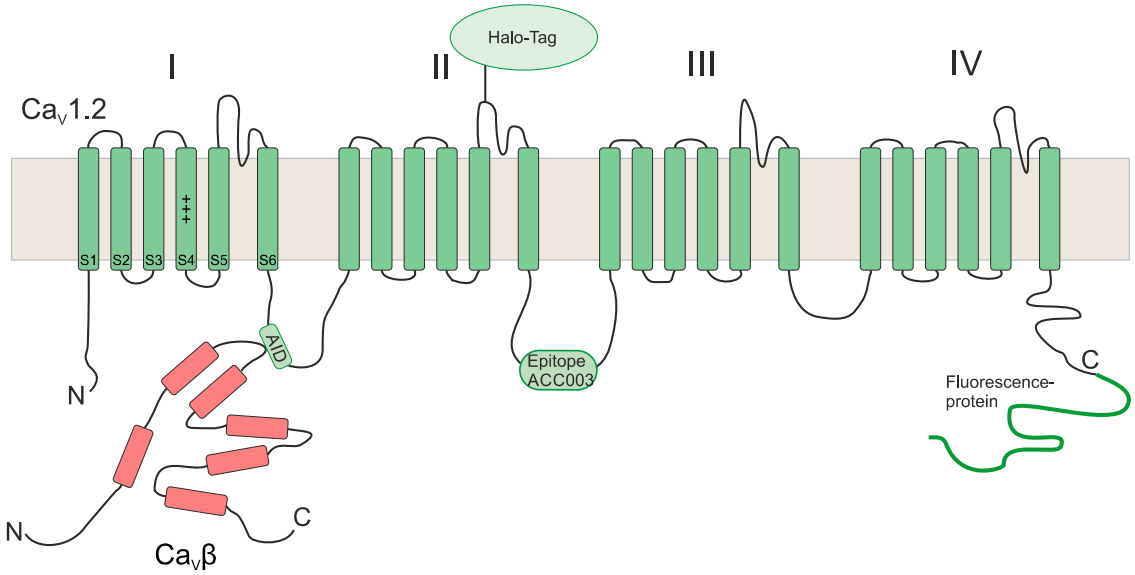

Figure 2.1: Membrane topology of a folded $Ca_V1.2$ protein with all used modifications. The highly conserved binding site for the $Ca_V\beta$ subunit, the AID (α-interaction domain) located within the intracellular linker connecting domains I and II is shown. The fluorescent protein was fused to the C-terminus of $Ca_V1.2$ while the HaloTag fusion tag was inserted within the extracellular loop between S5 and S6 of domain II. The antibody used to detect $Ca_V1.2$ recognizes an epitope within the intracellular loop connecting domins II and III.

Three fluorescent proteins, EYFP, EGFP and mNeonGreen, differing in their physical properties were tested as fusion partner for $Ca_V1.2$. Since the existing combination of $Ca_V1.2$ and EYFP was not photostable enough for our purpose, EYFP was replaced by EGFP. Therefore, the gene encoding for the $Ca_V1.2$ was excised from the existing plasmid $Ca_V1.2$-EYFP and inserted with HindIII and AgeI into a pEGFP-N1 vector.

For further optimization the EGFP was exchanged by a mNeonGreen (AlleleBiotech, with license), a more bright green fluorescent protein. Therefore the EGFP gene was excised and the gene encoding mNeonGreen with recombinant restriction sites (primers 3 and 4, Table 2.4) was inserted at the N-terminus of $Ca_V1.2$ with the restriction sites AgeI and XbaI.

2.1.11 Insertion of a HaloTag protein fusion tag into a $Ca_V1.2$-encoding plasmid

To selectively label channels that have being internalized, a HaloTag protein fusion tag (Promega) was fused to $Ca_V1.2$ within an extracellular loop in domain II (Figure 2.1). The HaloTag is a modified haloalkane dehalogenase (H273P) that can bind virtually in an irreversible fashion to diverse synthetic ligands.

Overlapping PCR was carried out to obtain three fragments. Fragment one contains the part of $Ca_V1.2$ from the N-terminus to the linker between loop II and III sites (primers 5 and primer 6 (Table 2.4)), fragment two the HaloTag fusion tag (primers 7 and 8) and the third fragments included the second part of $Ca_V1.2$ till the C-terminal end (primers 9 and 10). In the fourth PCR the three fragments were overlapped (primers 11 and 12). Afterwards the generated fragment was digested and cloned into a pcDNA3.1 (+) vector containing $Ca_V1.2$ with the restriction sites PmlI and HindIII.

2.1.12 Deletion of the AID-site

In order to investigate the trafficking with regard to the association between $Ca_V1.2$ and $Ca_V\beta$ subunits, the AID site within $Ca_V1.2$ was deleted in both constructs (pEGFP-$Ca_V1.2$-mNeonGreen and pcDNA3.1(+)$Ca_V1.2$-HaloTag). The cloning was also done using overlapping PCR. Two PCR reactions were set up to generate two PCR products encompassing either the channel region upstream or downstream the AID site (primers 13 and 14 and primers 15 and 16, Table 2.4). A third PCR reaction was performed using these two PCR products as template with primers 17 and 18 (Table 2.4).

The insert was finally subcloned into pEGFP-$Ca_V1.2$-mNeonGreen and pcDNA3.1 (+)-$Ca_V1.2\alpha$-HaloTag using BamHI/EcoRI and PmlI/HindIII, respectively.

2.1.13 Construction of plasmids for generating stable cell lines

Generation of stable inducible cell lines for expression of $Ca_V\beta2a$ coupled to mCherry and $Ca_V\beta2b$ to mRFP were performed. After adding recombinant restriction sites by PCR the DNA was inserted into a pcDNA5/FRT/TO vector. For $Ca_V\beta2a$ the primers 19 and 20 were used in PCR, for $Ca_V\beta2b$ the primers 21 and 22 were used (Table 2.4). Both inserts were ligated into their respective vectors using HindIII and BamHI.

2.2 Cell culture

2.2.1 Cell lines

In this study three different cell lines were used, HEK293, Flp-In T-REx and HL-1 cells.

2.2.1.1 HEK293

Human embryonic kidney (HEK) 293 cells are originally derived from a healthy aborted fetus. The cell line was generated by Graham and van der Eb in the 1970s (Graham et al. 1977) by transformation of normal HEK cells with sheared adenovirus 5 DNA. The transformation resulted in the incorporation of approximately 4.5 kb from the viral genome into human chromosome 19 of the HEK cells.

2.2.1.2 Flp-In T-REx

The Flp-In T-REx cell line is derived from 293 human embryonic kidney cells (Graham et al. 1977) and allows the rapid creation of stable mammalian cell lines which homogenously express the proteins of interest in an inducible manner. The Flp-In T-REx host cell line contains an integrated Flp Recombination Target site (FRT) as well as a tetracycline repressor. Cells are resistant to zeocin and blasticidin. For integration into the chromosomal DNA the pcDNA5/FRT/TO expression vector containing the gene of interest was cotransfected with a plasmid (pOG44) expressing the Flp recombinase. The expression vector linked to the hygromycin resistance integrates at the FRT site within the host cell genome via Flp recombinase mediated DNA recombination from pOG44. Once integrated in the genome, the Tet repressor protein controls the Tet-Operon region of the integrated pcDNA5 by repressing the gene expression. The expression can be induced by the addition of tetracycline to the culture medium (Figure 2.2).

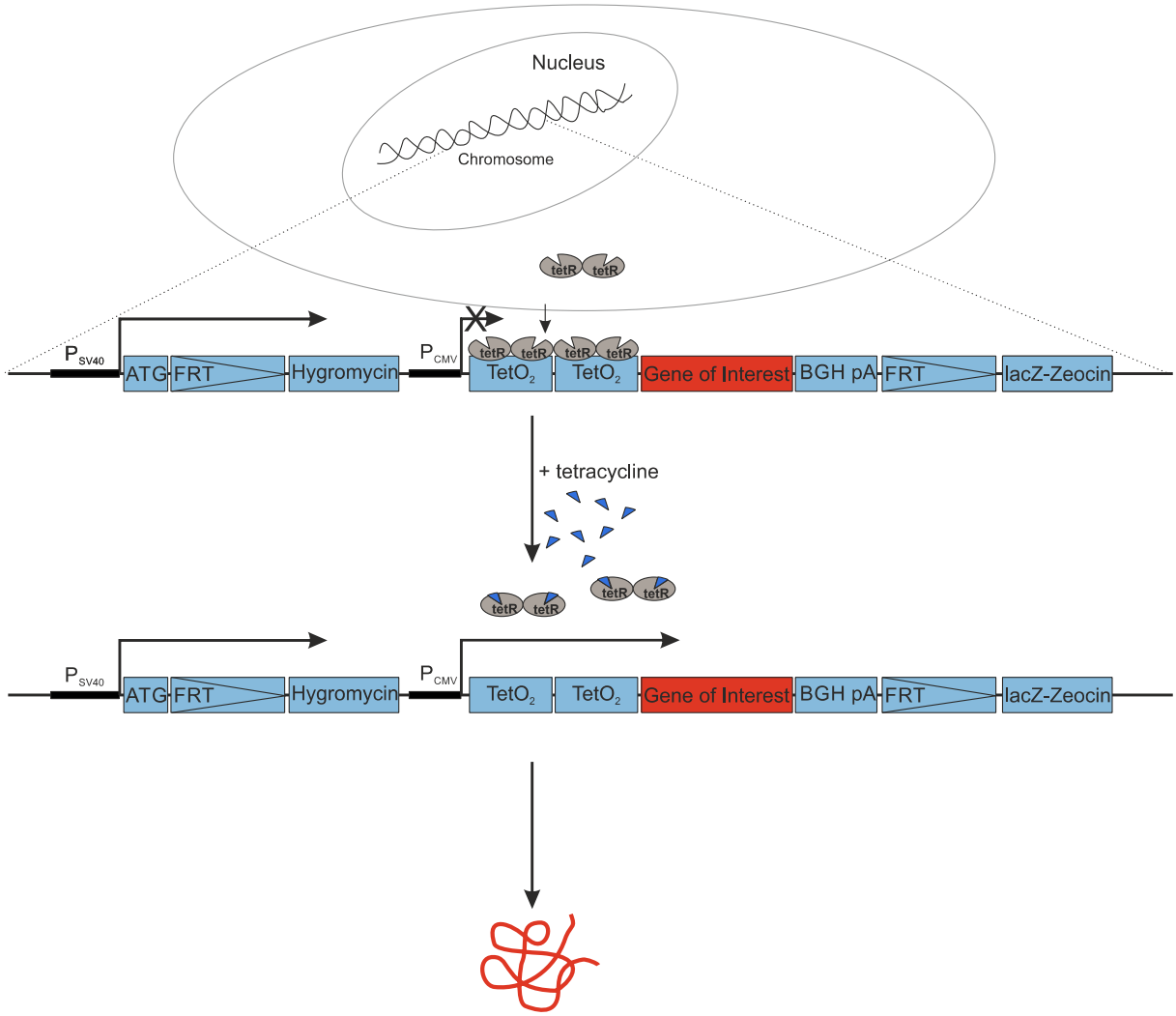

Figure 2.2: Diagram of the Flp-In T-REx system. After addition of tetracycline the repressor is released from the tetracycline operator 2 ($TetO_2$) and transcription of the gene of interest is turned on.

2.2.1.3 HL-1, a murine cardiac muscle cell line

Voltage-gated calcium channels are essential for heart function. The cardiac muscle cell line HL-1 is originally derived from the AT-1 mouse atrial cardiomyocyte tumor lineage and was generated by Claycomb et al. (1997) (Claycomb, 1997). Cells were a kind gift from Prof. W.C. Clycomb, LSU Health Sciences Center. It can be repeatedly passaged maintaining a cardiac-specific phenotype, including expression of $Ca_V1.2$, the most prominent voltage activated calcium channel expressed in cardiac muscle. Therefore it offers the possibility to investigate endogenously voltage-activated calcium channels.

2.2.2 Cell culturing conditions

HEK293 cells were grown in MEM medium (GlutaMAX, (Gibco)), supplemented with 10% (v/v) FBS (Gibco), 5 ml Antibiotic/Antimycotic (100X; Gibco) and 5 ml MEM not essential amino acids (Gibco), at 37°C and 5% CO2 in a humidified atmosphere. Media was exchanged every 2-3 days and cells were splitted twice a week when a confluency of 90% was reached.

Flp-In T-REx stable cell lines were grown in DMEM medium (high glucose, GlutaMAX, 3.7 g/L sodium bicarbonate (Gibco)) supplemented with 10% (v/v) FBS (Gibco), 5 ml Antibiotic/Antimycotic (100X; Gibco), 2mg/ml Hygromycin and 2mg/ml Blasticidin. Hygromycin and Blasticidin were stored at 7 °C.

HL-1 cells were grown in Claycomb media supplemented with 10% fetal bovine serum (SigmaAldrich), 10 µM norepinephrine (SigmaAldrich), 2 mM L-glutamine (SigmaAldrich) and 100 U/ml penicillin/streptomycin (ThermoFisher Scientific) at 37°C in 5% CO_2. Exchange of media was done every 24–48 h.

2.2.3 Splitting and seeding cells

HEK293 cells and Flp-In T-REx cells were grown until approximately 90% confluency, washed with PBS and detached from the petri dishes by treatment with 0.8 ml of 0.05% trypsin/EDTA (Gibco) for approximately 5 minutes at 37°C. The activity of trypsin was neutralized by addition of 10 ml serum-containing culture media. The cell suspension was collected in 15 ml centrifuge flasks (Greiner BioOne) and centrifuged for 5 min at 200 g (Sigma 3k12 centrifuge, B Braun Biotech). After discarding the supernatant the cell pellet was resuspended in fresh media. The number of cells per ml cell suspension was determined by using a Neubauer-hemocytometer. For maintenance of the cells, they were seeded onto 10 cm-dishes at two different densities depending on the time elapsed for the next splitting. On Fridays cells were seeded at a density of 8 x 10^5 cells per dish and splitted on coming Monday and on Mondays at a density of 4 x 10^5 cells per dish to be splitted next Friday. For transfection cells were seeded either onto 3.5 cm dishes or 18 mm coverslips at a density of 2 x 10^5 or 1 x 10^5 cells per dish respectively, both coated with poly-L-Lysine (PLL), and used the next day.

For maintenance of the HL-1 cell line, cells were grown in T25 flask (Tissue Culture Flask, BD Falcon) pre-coated with gelatin/fibronectin and seeded at a density of 2.5 x 10^5, 5 x 10^5 and 10 x 10^5 cells per flask filled with 5 ml media. Cells were splitted upon reaching more than 90% confluency with 0.05% trypsin/EDTA. They were briefly rinsed with 1 ml prewarmed trypsin/EDTA solution by pipetting the solution onto the bottom of the flask and quickly removing it by aspiration. Cells were then incubated with 1 ml trypsin/EDTA solution for approximately 2 min at 37°C until cells detach from the bottom of the flask. The activity of trypsin was neutralized by adding 5 ml of culture media, supplemented with serum. The cell suspension was centrifuged in 15 ml tubes for 5 min at 500 g and after removing the supernatant the cell pellet was resuspended in 3 ml fresh pre-warmed culture media. The number of cells per ml cell suspension was determined by using a Neubauer-hemocytometer. For transfection and immunostaining, cells were seeded on 18 mm coverslips, pre-coated with gelatin/fibronectin at a density of 4 x 10^4 cells per coverslip and used for the next day.

2.2.3.1 Coating with Poly-L-Lysine (PLL)

Sterile 18 mm glass coverslips were placed in wells of 4-multiwell plates (ThermoScientific) or 24-multiwell plates (Greiner Bio-One). Each well was filled with 500 µl of a 1:10 dilution of the PLL stock solution (1 mg/ml, SigmaAldrich). When using 3.5 cm dishes with glass bottom (ibidi) 750µl of PLL-dilution was added per dish. After 2 h incubation at 37°C, all glass bottoms were washed twice with PBS before adding serum-containing growth media.

2.2.3.2 Coating with gelatin/fibronectin

Coating of T25 flasks and sterilized 18 mm glass coverslips with gelatin (0.02%)/fibronectin (5µg/ml) (Sigma) was performed over night at 37°C. Coverslips were placed in wells of 4- or 24-multiwell plates and filled with 300 µl gelatin/fibronectin. T25 flasks were coated using 2 ml gelatin/fibronectin solution.

2.2.4 Transfection techniques

2.2.4.1 Calcium Phosphate transfection

The Calcium Phosphate Transfection method for introducing DNA into mammalian cells is based on forming calcium phosphate-DNA precipitates. These bind strongly to the surface of the cell monolayer and enhance uptake of DNA by endocytosis (Chen and Okayama (1987)). Cells were grown on 5 cm dishes and transfected at 70% confluent cells. The desired amount

of DNA was diluted in 124 µl H_2O and 41 µl 1 M $CaCl_2$-solution. Then 165 µl 2X BBS buffer (50 mM BES, 280 mM NaCl, 1.5 mM Na_2HPO_4 (2 H_2O), pH 6.95) were added. After 20 min incubation time at room temperature (RT) the transfection solution was added dropwise to the dish. Cells were incubated at 37°C and 5 % CO_2 for 20-22 h. Then cells were washed with PBS/EDTA to remove precipitates and then splitted either in multiwell plates or 35 mm dishes.

2.2.4.2 Liposome-mediated transient and stable transfection

The liposome-mediated transfection is based on the merge of phospholipid bilayer liposomes with the cell membrane to transfer genetic material into a cell. Since the genetic material is negatively charged, lipofection generally uses a positively charged lipid to form an aggregate. Here Lipofectamine 2000 Transfection Reagent (Invitrogen) was used. This is added in a ratio of 2:1 to the desired amount of DNA diluted in OptiMEM (Gibco) and incubated 30 min at RT. The complete mix is then added dropwise to the cells in standard culture medium for 1 h, then the culture media was changed. For confocal microscopy, cells were transfected either in ibidi 35 µm dishes with glass bottom or in multiwell-plates onto sterile glass coverslips.

2.2.5 Generating of Flp-In T-REx expressing cell lines

To generate a stable Flp-In T-REx cell line, the gene of interest (here Ca_Vβ2a-mCherry and Ca_Vβ2b-mRFP) were subcloned into the pcDNA5/FRT/TO expression vector (see 2.1.13). Cells were cotransfected with a 9:1 w/w ratio of pOG44: pcDNA5/FRT/TO plasmids by liposome-mediated transfection. After 1 h cells were washed with culture media and then again fresh culture media was added. For transfectant selection, cells were trypsinized and splitted in fresh media containing 100 µg/ml hygromycin B and 10 µg/ml blasticidin (ThermoFisher) 48 h after transfection. After approximately 2 weeks 10 hygromycin-resistant foci were picked and grown upon 80% confluency. With tetracycline induction pools of cells were checked for expressing quality and those showing the brightest fluorescence were freezed (see 2.2.6).

2.2.5.1 Induction of inducible Flp-In T-REx cell lines

To induce the expression of the Ca_Vβ integrated in the genome of two Flp-In T-REx cells (cf. 2.2.5), cells were incubated with media containing 1 µM of tetracycline. In order to investigate the effect of Ca_Vβ on Ca_V1.2 that has been already translated i.e. post

transcriptional stage, cells were transfected with a plasmid encoding fluorescently labelled $Ca_V1.2$ and expression of $Ca_V\beta$ was induced 24 h after transfection for at least 8 h. After this time cells were imaged by confocal microscopy (Figure 2.3).

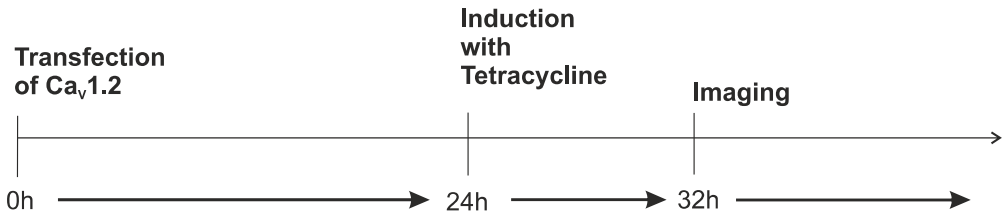

Figure 2.3: Experimental procedure for the induction of the $Ca_V\beta$- expression in inducible Flp-In T-REx cell lines. Cells that were transiently expressing $Ca_V1.2$ were induced with tetracycline 24 h after transfection cells to allow transduction of the channel protein.

2.2.6 Freezing cells

For long-term-storage of Flp-In T-REx cells, cells were harvested at the logarithmic growth-phase from a 10 cm plate culture. About 2 x 10^6 cells per ml DH10 medium containing 10% DMSO were fast frozen in liquid nitrogen. Grown cells were washed with PBS and trypsinized 5 minutes at 37°C. Cells from every 10 cm dish were admitted to 8 ml of serum-containing culture media. The cell suspension was collected in a 50 ml tube and centrifuged for 5 min at 200 g (Sigma 3k12 centrifuge). The supernatant was removed and the cell pellet was resuspended in 10 ml fresh culture media. Cryovials (Nunc Cryotube Vials, ThermoFisher) containing 100 µl DMSO were filled with 900 µl of the cell suspension and frozen in liquid nitrogen during 4 h. Frozen cells were stored at -150°C.

2.2.7 Thawing cells

After 20 passages, HEK293 and Flp-In T-Rex cells were discarded and a new aliquot thawed for further culturing. Cells were taken from -150°C and immediately warmed at 37°C with continuous agitation. Defrosted cell suspension was added to 9 ml prewarmed culture media supplemented with serum in a 15 ml tube. After centrifugation for 5 min at 200 g (Sigma 3k12 centrifuge), cells were resuspended in 9 ml fresh prewarmed culture media and plated onto two 10 cm dishes.

2.3 Microinjection

Microinjection is a mechanical process to inject a liquid substance into a living cell. With the aim of studying the acute effect of $Ca_V\beta$ on $Ca_V1.2$ function, recombinant β-subunit covalently linked to a fluorescence protein was microinjected in cells already expressing the channel protein. With the use of a glass capillary adherent cells are penetrated to introduce the purified protein in their cytoplasm. For microinjection experiments transfected and non-transfected HEK293 cells were seeded in 35 mm dishes with glass bottom and grid (ibidi). Prior to the experiment the culture media was discarded and cells were washed twice and stored in imaging solution (ES, 120 mM NaCl, 5 mM KCl, 2 mM $CaCl_2•H_2O$, 2 mM $MgCl_2•H_2O$, 10 mM HEPES, 10 mMD-Glucose•H_2O; pH 7.4). The glass capillary (Femtotips I 1 µm outer Ø, Eppendorf) was filled with the fluorescence labelled $Ca_V\beta$ protein dissolved in protein buffer.

With the help of a micromanipulator (InjectMan 4, Eppendorf) in combination with a microinjector (FemtoJet 4x, Eppendorf) the purified protein was injected within the adherent cells. With an angle of 45° the mechanically arm, holding the capillary was moved above the 35 mm dish. The capillary holder with the filled capillary was carefully brought into the focal plane of the microscope (Nikon Eclipse Ti) by means of movements in the x-, y- and z-plane controlled by a joystick. For the fine adjustment a higher magnification was needed in order to position the tip of the capillary just touching the top of the cell membrane in the perinuclear region. At this point a Z-limit for the capillary movement corresponding to the injection was set (Figure 2.4). Before each injection, the capillary had to be lifted until no contact with the cell was achieved. The injection was performed semi-automatically with the settings described in Table 2.8. After injection cells were analyzed with a confocal laser scanning microscope (see 2.7).

Table 2.8: Settings for semi-automatical microinjection. Settings of the FemtoJet to microinject HEK293 cells perinuclear with purified fluorescence labelled protein.

Settings	
Injection pressure	150 hPa
Compensation pressure	40 hPa
Injection time	0.2 s

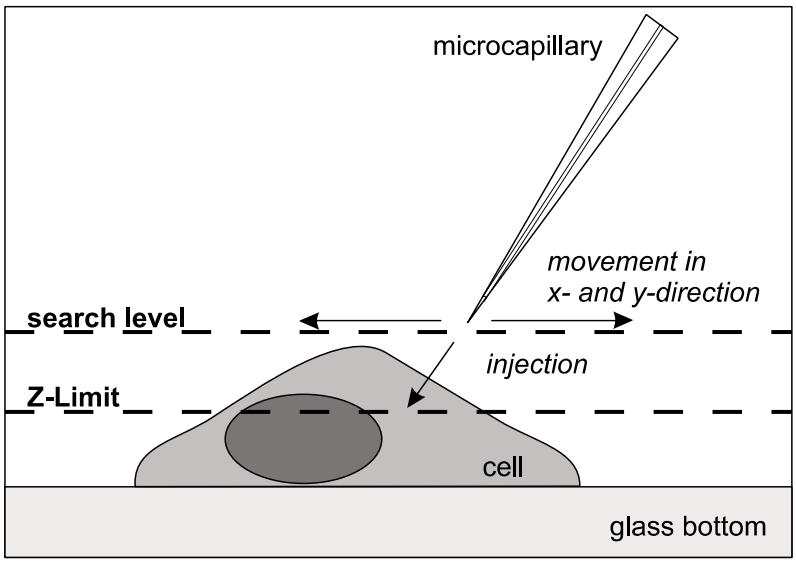

Figure 2.4: Principle of semi-automated microinjection. Purified fluorescently labelled proteins are injected into the perinuclear region of adherent cells. Graphic modified from Eppendorf user guide 027.

2.4 Pharmacological blocking

To inhibit the trafficking pathway of proteins at defined stages during their transport from the ER to the plasma membrane different pharmaceuticals were used.

2.4.1 Nocodazole

Nocodazole is an antimitotic agent that directly binds to β−tubulin and inhibits the polymerization of microtubules by preventing the formation of interchain disulfide linkages between the tubulin monomers. Pharmacological disruption of the microtubule network was achieved by incubating the cells 2-20 h at 37°C in culture media containing 33 µM nocodazole (Sigma). The stock solution of nocodazole, 5 mg/ml in DMSO was stored at -20°C.

2.4.2 Cytochalasin D

Cytochalasin D belongs to a class of fungal metabolites that have the ability to block polymerization of actin, by binding with high affinity to the growing ends of actin filaments (F-actin) and preventing addition of monomers (G-actin). Cells were incubated with 10 µM cytochalasin D (Sigma) dissolved in fresh culture media for 2 h at 37°C. The stock solution of cytochalasin D, 5 mg/ml in DMSO was stored at -20°C.

2.5 Immunochemistry

For immunostaining cells were grown onto glass coverslips, fixed for 5-10 min with 4% paraformaldehyde in PBS for 10 min at 37°C, and washed twice with PBS for 5 min each. The first antibody was diluted in a blocker solution (CT, 5% Chemiblocker (EMD Millipore), 0.5% Triton X-100 in PBS) and cells were incubated with primary antibody solution for 1 h at RT. Cells were washed twice for 10 min with PBS and then incubated with the secondary antibody solution for 30 min at RT in the dark and finally washed again with PBS two times for 10 min. The coverslips were mounted upside down on glass slides using Aqua Polymount (Polysciences), air dried in the dark overnight and stored at 4°C until use. The antibodies used and their corresponding dilution are listed in Table 2.9.

Table 2.9: Primary and secondary antibodies (and phalloidin) used in this project for immunochemical staining.

1st antibody	Antigen	Species	Dilution	Origin
Anti-Ca_V1.2-ATTO488	Ca_V1.2	rabbit	1:200	alomon labs
Anti-β-Tubulin	Tubulin	mouse	1:500	Invitrogen
Anti-α-Tubulin	Tubulin	mouse	1:500	Sigma
Anti-Rab7	Rab7	mouse	1:250	Santa Cruz
Anti-Rab11	Rab11A	mouse	1:250	Santa Cruz
Anti-GCC1	GRIP; coiled-coil domain-containing protein1	rabbit	1:200	Sigma
Anti-SEC16A	SEC16A	rabbit	1:500	Sigma
Anti-Clathrin	Clathrin Heavy Chain	mouse	1:100	BD Bioscience
Anti-EEA1	Early Endosom Antigen 1	mouse	1:100	Santa Cruz
Phalloidin488	Actin	-	1:500	Invitrogen
Phalloidin647	Actin	-	1:500	Invitrogen

2nd antibody	Anti	Species	Dilution	Origin
Cy3	mouse	donkey	1:200	Dianova
Cy3	rabbit	donkey	1:200	Dianova
Cy5	mouse	donkey	1:200	Dianova
Cy5	rabbit	donkey	1:200	Dianova

2.6 Live cell staining

2.6.1 SiR-Tubulin and SiR-Actin

SiR-Tubulin and SiR-Actin (Spirochrome) are both based on the fluorophore silicon rhodamine (SiR; excitation maximum = 652 nm; emission maximum = 674 nm). While the active component of SiR-Tubulin is the microtubule binding drug Docetaxel, of SiR-Actin is the actin binding natural product jasplakinolide. Both dyes are cell permeable and thus, can be used for labelling the tubulin- and actin-based cytoskeleton in living cells. The labelling reaction was carried out for 30 min at 37°C in DMEM media without phenol red (high glucose, 3.7 g/L sodium bicarbonate (Gibco) supplemented with 4 mM GlutaMAX and 10% (v/v) FBS) using 500 nM of SiR-Tubulin or SiR-Actin. Imaging of labelled cells was done with confocal microscopy. The 1 mM stock solutions were stored at -20°C.

2.6.2 CellMask

The plasma membrane of living cells was labelled using CellMask Deep Red plasma membrane stain (ThermoScientific). Cells were grown on glass coverslips or in 35 mm dishes with glass bottom and labelled for 2 min, to avoid internalization of the dye, at room temperature with a 0.5 X working solution from the provided 1000X stock solution prepared in warm cultured media. Cells were then washed with OptiMEM media and imaged with confocal laser scanning microscopy at 660 nm excitation and 677 nm emission wavelengths. The 1000X stock solution was stored at -20°C.

2.6.3 ER-Tracker

To stain the endoplasmic reticulum in living cells the ER-Tracker Red (BODIPY TR Glibenclamide, ThermoFisher) was used. Glibenclamide binds to the sulphonylurea receptors of ATP-sensitive potassium channels, which are prominent in the ER membrane. The labelling was done with a 1 µM working solution in fresh media for 20 min at 37°C. After two washing steps with OptiMEM imaging of labelled cells was done with a laser scanning microscope (excitation maximum = 587 nm, emission maximum = 615 nm). The 1 mM stock solution was stored at -20°C.

2.6.4 HaloTag ligands

Cells, expressing HaloTag fusion proteins can be fluorescently labelled, specifically and irreversibly, using several commercially available fluorescent HaloTag ligands. Cell-permeable fluorescent ligand TMR and cell-impermeable fluorescent ligands AlexaFluor488 and AlexaFluor660 were used as described (Table 2.10). Stock solutions are stored at -20°C.

Table 2.10: Concentration, labelling time and fluorescent properties of HaloTag ligands used in this project.

HaloTag ligand	[Stock solution]	[Working solution]	Excitation maximum	Emission maximum
AlexaFluor488	1 mM	100 nM	499 nm	518 nm
TMR	5 mM	100 nM	552 nm	578 nm
AlexaFluor660	3.5 mM	100 nM	654 nm	690 nm

Two strategies, standard and pull chase, were followed to label $Ca_V1.2$ fused to a HaloTag expressed in HEK-derived cells. In the standard protocol, transfected cells were labelled by incubation with 100 nM of HaloTag ligand for 15 min at 37°C and washed twice with fresh culture media. Cells were either used immediately for live imaging or fixed for confocal laser scanning visualization. The pulse chase experiment consists of two sequential labelling with two different HaloTag ligands and was aimed to differentiate channels that are on their way to the plasma membrane (secretory pathway) from channels assembled in the plasma member or that have been subjected to internalization.

Cells were first stained with the cell impermeable ligand for 15 min and after two washes cells were labelled with a cell permeable ligand (Figure 2.5).

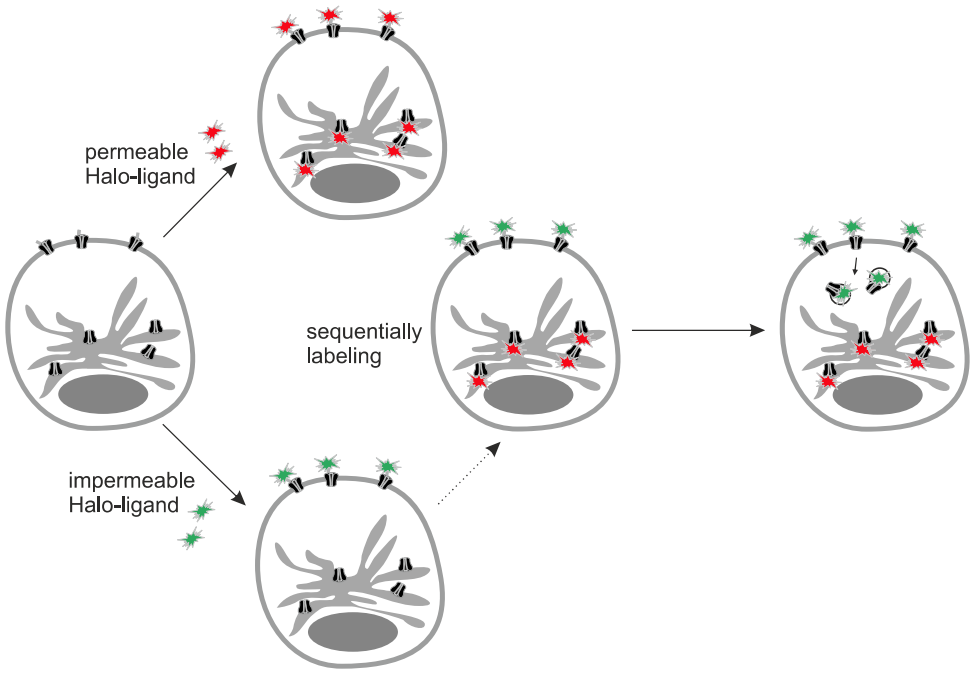

Figure 2.5: HaloTag labelling. Principle of the sequential labelling of HaloTag fusion proteins with cell permeable (red) and cell impermeable (green) HaloTag fluorescent ligands.

2.7 Laser scanning confocal microscopy

The confocal laser scanning microscope (TCS SP5 II, Leica Microsystems) was equipped with an Argon laser (458, 488 nm) and three Helium-Neon lasers (543, 594, 633 nm). Pictures were acquired with a 20x/0.70 oil or a 63x/1.32-0.6 oil immersion objective at 1024x1024 pixels and a line average of four. Acquisitions were done using the Leica LAS AF software.

2.7.1 Image analysis

Images from cells expressing two different fluorescent proteins were analyzed to determine the degree of colocalization between the two labelled proteins. In multi-color fluorescence microscopy, each signal is separated into specific channels corresponding to the level of fluorescence emission signal of each fluorophore after being excited. Colocalization between the fusion proteins was evaluated using the intensity correlation coefficient-based (ICCB) analysis to evaluate the Mander's coefficient embedded in the PlugIn "JACoP" (Bolte and Cordelieres 2006). This coefficient estimates the proportion of the amount of each fluorophore colocalized with the other one for each pixel independent on the intensities of the signals (Manders et al. 1993). It is calculated as follows:

$$(1) \qquad M_1 = \frac{\sum_i Ch1_{i,coloc}}{\sum_i Ch2_i}$$

where $Ch1_{i,coloc}$ =$Ch1_i$ if $Ch2_i > 0$ and $Ch1_{i,coloc} = 0$ if $Ch2_i = 0$;

$$(2) \qquad M_2 = \frac{\sum_i Ch2_{i,coloc}}{\sum_i Ch1_i}$$

where $Ch2_{i,coloc}$ =$Ch2_i$ if $Ch1_i > 0$ and $Ch2_{i,coloc} = 0$ if $Ch1_i = 0$.

M_1 is defined as the ratio between the sum of the fluorescence intensities of pixels from channel 1 (Ch1) that overlap a component from channel 2 to the total intensity in channel 2 (Ch2). M_2 is defined conversely for channel 2. Therefore, the coefficient is an indication of the contribution of each channel to the colocalization. The value for the overlapping fractions varies from 0 (no colocalization) to 1 (complete colocalization). As the coefficient is sensitive to noise before analysis an individual threshold has to be set for each image to avoid false positives by means of a high background.

2.7.2 Statistical data analysis

Statistical analysis and comparisons for the overlapping fractions were conducted using the software GraphPad Prism 5 and the software MatLab. Statistical differences between the test series were analyzed using either One-Way ANOVA followed by post hoc Bonferroni's Multiple Comparison test ($p \leq 0.001$) or a Mann-Whitney rank test ($p \leq 0.001$).

2.8 Spinning Disk confocal microscopy

Spinning Disk confocal microscopy was used to follow the movement of fluorescent particles in vivo inside the cell. The spinning disk unit was equipped with a confocal laser scanning microscope (Nikon Eclips Ti) combined with a Confocal Scanner Unit (CSU-W1, Yokogawa) and five lasers with excitation wavelength 405 nm, 445 nm, 488 nm, 561 nm and 640 nm. Using an optical beam splitter the channels excitation by 488 nm and 561 nm could be measured simultaneously. Images were acquired with a 100x/1.49 oil immersion objective at 512x512 pixels. The software Andor IQ2 was used for acquisition of all settings. For all time-lapse recordings the exposure time was set to 300 ms and the interval of the frame rate to

0 ms. The laser power and the number of focal planes (z-frames) were set individually for every record. Cells were mounted inside StageTop Incubator system (Okolab) on the microscope stage for precise control of the temperature (37°C), humidity (85%), and CO_2-concentration (5%).

2.9 Particle detection, tracking and image analysis.

Single particle tracking analysis was used to characterize the movement of $Ca_V1.2$ channels complexes within the cells. Detection and tracking of fluorescent particles were performed with the 3D tracking module ImarisTrack embedded in Imaris 8 software (Bitplane Scientific). This algorithm allows automatic detection of particles that for our purposes were set for the ones with an estimated diameter of 400 nm and an estimated ellipsoid-diameter of 800 nm in the z-direction. Detected spots were filtered based on the control parameter 'Quality'. This is defined as the intensity at the center of the spot in the corresponding channel, Gaussian filtered by 3/4 of the spot radius minus the intensity of the original channel, Gaussian filtered by 8/9 of the spot radius. Only spots with values higher than the set threshold values were considered for analysis. Appropriate threshold values were confirmed by visual inspection. After detection of the spots in each frame, and therefore each time point, connection between spots in consecutive frames were traced through sequential frames using an Autoregressive Motion Model. A maximum search distance of 1.5 – 2.5 µm in all axes, depending on satisfying trajectories, was defined in order to avoid false connections. If an object could not be detected in some frames this would lead to creation of tracks fractions. The gap-closing algorithm based on a maximal gap size value creates tracks by linearly connecting objects associated with the same track. In this project the maximal gap size value was set to one, so one time points was allowed to be missing while tracking. To correct for tracking errors, trajectory outputs were visually inspected and, as necessary, edited. Generated trajectories were filtered by ‘Track Duration’ the total trajectory duration time. Only trajectories of duration longer than 50 s were chosen for further analysis. The entire pool of trajectories was then filtered by means of the ‘Track Displacement Length’, the net distance traveled (d_{net}). Tracks were separated as possible in trajectories longer than 2 µm displacement length and shorter than a displacement length of 2 µm.

By using the Imaris Plugin Mean-square-displacement (MSD) analysis (produced 2013 by Jean-Yves Tinevez) based on MATLAB (MathWorks) the mean square displacement curves of every single trajectory were calculated and given as sum of all curves in a MATLAB

Figure. For separate analyzation the MSD value was calculated with the equation shown in Table 2.11.

Dynamic parameter of all tracks, calculated as shown in Table 2.11, were exported directly from Imaris for further analysis. Subsequently, the different parameters were used for comparable statistics.

Table 2.11: Quantitative tracking measures used in this study. Equations given for a sample trajectory consisting of *N* points with $p_i = (x_i, y_i, z_i)$ corresponding to *n* frames. A constant frame rate is given by a time interval of Δt seconds between successive frames. The distance between any two points p_i and p_j is taken to be the Euclidean norm $\|p_i - p_{i+j}\|_2$.

Measure for each trajectory	Definition
Total duration time	$t_{tot} = (N-1)\Delta t$
Displacement length traveled	$d_{net} = \|p_1 - p_N\|_2$
Instantaneous speed	$s_i = \|p_i - p_{i+1}\|_2 / \Delta t$
Mean speed	$\bar{s} = \frac{1}{N-1}\sum_{i=1}^{N-1} s_i$
Mean square displacement	$MSD(t) = \frac{1}{N-t}\sum_{i=1}^{N-t}\|p_i - p_{i+t}\|_2^2$

2.9.1 Fitting of MSD curves

The calculated MSD curves for every single track were fitted according to three models describing the movement of particle (Lund et al. 2014).

Brownian diffusion describes the random motion of particles suspended in a fluid. This motion is described mathematically as

(1) $MSD(t) = 6Dt$

where D is the diffusion coefficient and t the time lag. Based on the assumption that calcium channels are transported through the cell the first analytical model describes the movement of a particle as diffusion plus flow:

(2) $MSD(t) = 6Dt + v^2t^2$

where D is the diffusion coefficient, v the velocity and t the time lag.
The second model implements the factor of an anomalous diffusion:

(3) $MSD(t) = 6D_\alpha t^\alpha$

The anomalous exponent could either be $0 < \alpha < 1$ for anomalous subdiffusion or $1 < \alpha \leq 2$ for anomalous superdiffusion.
The third model combines the anomalous diffusion with the directed component:

(4) $MSD(t) = 6D_\alpha t^\alpha + v^2t^2$

All three models were used to find the best fit for each track and to further compare calculated values of diffusion coefficients, velocities and α-values. Fitting was done with MATLAB.

2.10 Software

Table 2.12: Software used in this project.

Software	Purpose	Producer
Word Professional Plus 2010	Word processor	Microsoft
Excel Professional Plus 2010	Data analysis	Microsoft
Matlab 2013a and 2016b	Numerical computing environment for data analysis	MathWorks
Imaris 8	Image analysis	Bitplane Scientific
Andor IQ	Live cell imaging	Andor
LAS AF	Microscope imaging	Leica
Image J	Image processing	National Institute of Health
Corel Draw X6	Vector graphics editor	Corel Cooperation
GraphPad Prism	2D graphics and statistics	GraphPad Software, Inc
Vector NTI	Bioinformatics, Cloning	InforMax Inc
Ligation Calculation	Calculation of 1:3 molar relation	http://www.insilico.uni-duesseldorf.de/Lig_Input.html

3 Results

The aim of this study was to characterize the intracellular transport of the $Ca_V1.2$ L-type voltage-gated calcium channels in heterologous expression system as well as in native conditions using the HL-1 cardiac derived cell line. Therefore, the membrane compartments where the channels reside during its itinerary to and from the plasma membrane were examined by colocalization analysis. In addition, the movement of the channel within the cell was evaluated using single particle tracking analysis to generate trajectories for the channels' transport. The quantitative analysis of the resulting trajectories provided information about the mode of motion, diffusion coefficient and velocity of channel-containing vesicles.

Accordingly, the result section is divided in two main subsections describing the vesicular trafficking pathway of voltage activated calcium channels, including their biosynthetic anterograde secretory as well as retrograde pathway after internalization and the analysis of the trajectories.

3.1 Dependence of $Ca_V1.2$ early secretory pathway on $Ca_V\beta$

Every synthetized plasma membrane protein is first inserted in the ER membrane from where only correctly folded proteins enter the secretory pathway to be transported in vesicles to the plasma membrane.

In order to investigate the secretory transport of $Ca_V1.2$, several cellular stations were examined, starting with the release of the channel from the ER to its final insertion into the plasma membrane via the *trans*-Golgi network sorting machinery and the vesicular transport along cytoskeletal tracks. Different markers for specific labelling of diverse cellular components, including, ER, Golgi, endosomal compartments and cytoskeleton, were used and their colocalization with fluorescently labelled $Ca_V1.2$ subunits analyzed. Quantification of the degree of colocalization was done using the Mander's overlap coefficient.

Hereinafter, from every set of labelling one representative image is shown and the fluorescence intensities plot along a linear region of interest (ROI) for both emission channels is included.

It is well established that the association of $Ca_V\beta$ with $Ca_V1.2$ is required to release the channel from the ER, but how long the pore-forming subunit remains competent for exiting the ER exit and whether $Ca_V\alpha_1$ and $Ca_V\beta$ dissociates after leaving the ER remains unknown. These questions are addressed in my thesis.

We also observed that fluorescently labelled $Ca_V1.2$ subunit requires the presence of $Ca_V\beta$ for ER exit. Images from HEK293 cells transfected with a plasmid encoding for $Ca_V1.2$ coupled to mNeonGreen show that the channel accumulates intracellularly with predominant perinuclear localization. Cells expressing the fluorescently labeled $Ca_V1.2$ channel stained with the ERTracker for ER and the CellMask dye for cell membrane, shows that in the absence of $Ca_V\beta$, $Ca_V1.2$ is not targeted to the plasma membrane but instead it accumulates in the ER (Figure 3.1A). Thus to study transport of $Ca_V1.2$ in heterologous expressing systems both subunit must be co-transfected. To facilitate the multi-fluorescence imaging, the expressed $Ca_V\beta$ was not coupled to a fluorescence protein. Cells expressing $Ca_V1.2$ together with $Ca_V\beta$ were clearly distinguishable from cells expressing the channel alone (Figure 3.1).

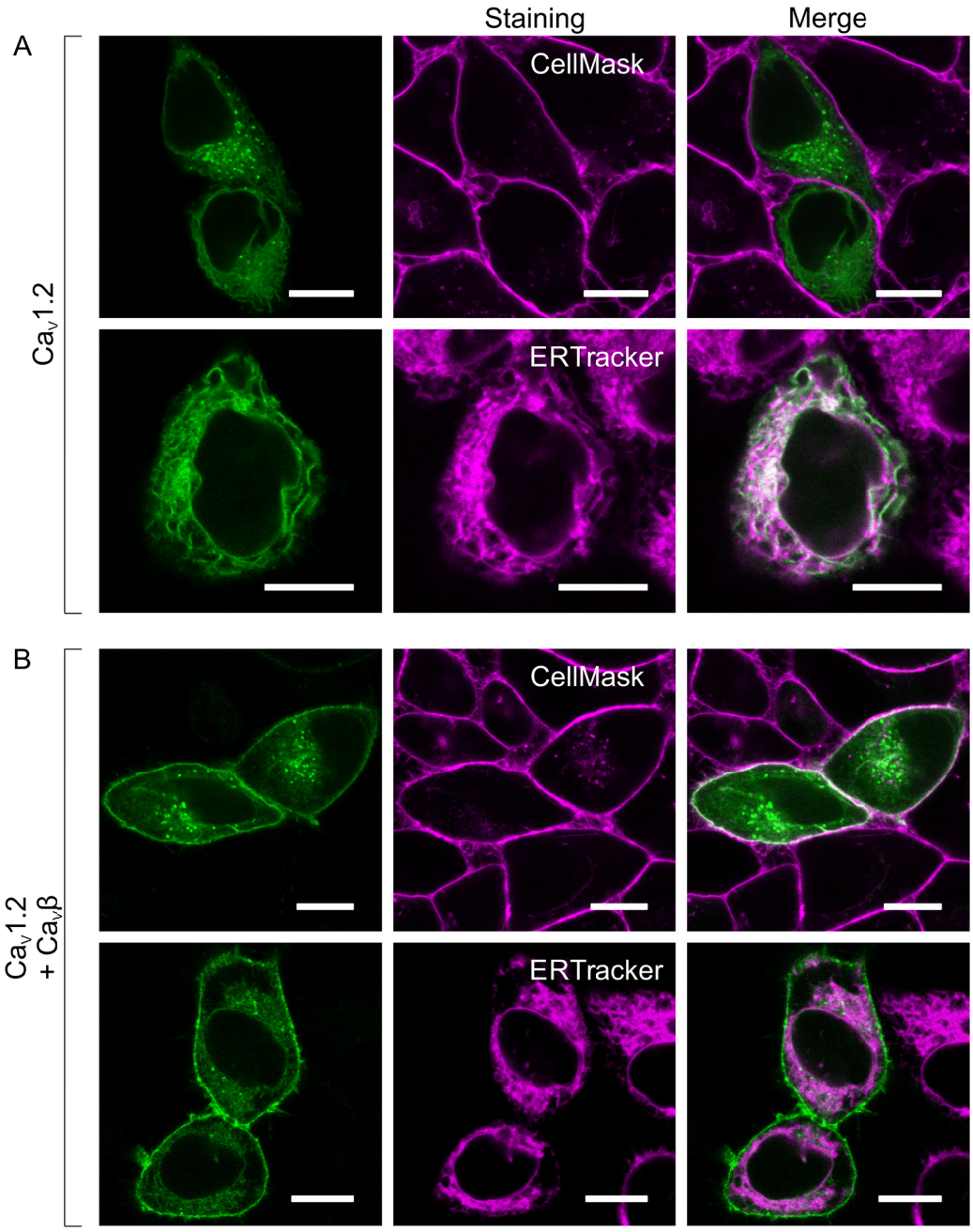

Figure 3.1: $Ca_V1.2$ accumulates in the ER in the absence of $Ca_V\beta$. Laser scanning confocal images of HEK293 cells A) transfected with $Ca_V1.2$-mNeonGreen or B) cotransfected with $Ca_V\alpha1.2$mNeonGreen and $Ca_V\beta$ unlabelled in the left column, respectively (green). 24 h after transfection, cells were labelled with CellMask (upper row), a membrane marker or ERTracker (lower row), a marker for endoplasmic reticulum in the middle column (magenta). The right column shows the merge of transfection and labelling. The overlap is reflected in white colour. Scale bars = 10 µm.

In the laser scanning confocal images (Figure 3.1) $Ca_V1.2$ alone shows a clear white overlap with the ERTracker but not with CellMask, whereas $Ca_V1.2$ expressed together with $Ca_V\beta$ overlaps with the plasma membrane, and fewer channels are located in the inner of the cell. Figure 3.2 shows the fluorescence intensity plot across the cell for the ER, plasma membrane and $Ca_V1.2$ signals. As expected the CellMask fluorescence intensity results in two peaks at the plasma membrane location while the ER signal shows a more continuous distribution within the cell. The fluorescence intensities of ERTracker and $Ca_V1.2$ without $Ca_V\beta$ have a common course, whereas the fluorescence intensities of $Ca_V1.2$ and CellMask show no positive correlation (Figure 3.2A). However in images from cells coexpressing $Ca_V1.2$ and $Ca_V\beta$, the fluorescence intensity curve for $Ca_V1.2$ demonstrates the two-peak distribution of the CellMask but no joint course with the ERTracker. Together these results confirm that $Ca_V\beta$ is required for ER exit and cell surface expression of the $Ca_V1.2$ subunit and suggest that ER exit mediated by $Ca_V\beta$ is relatively efficient.

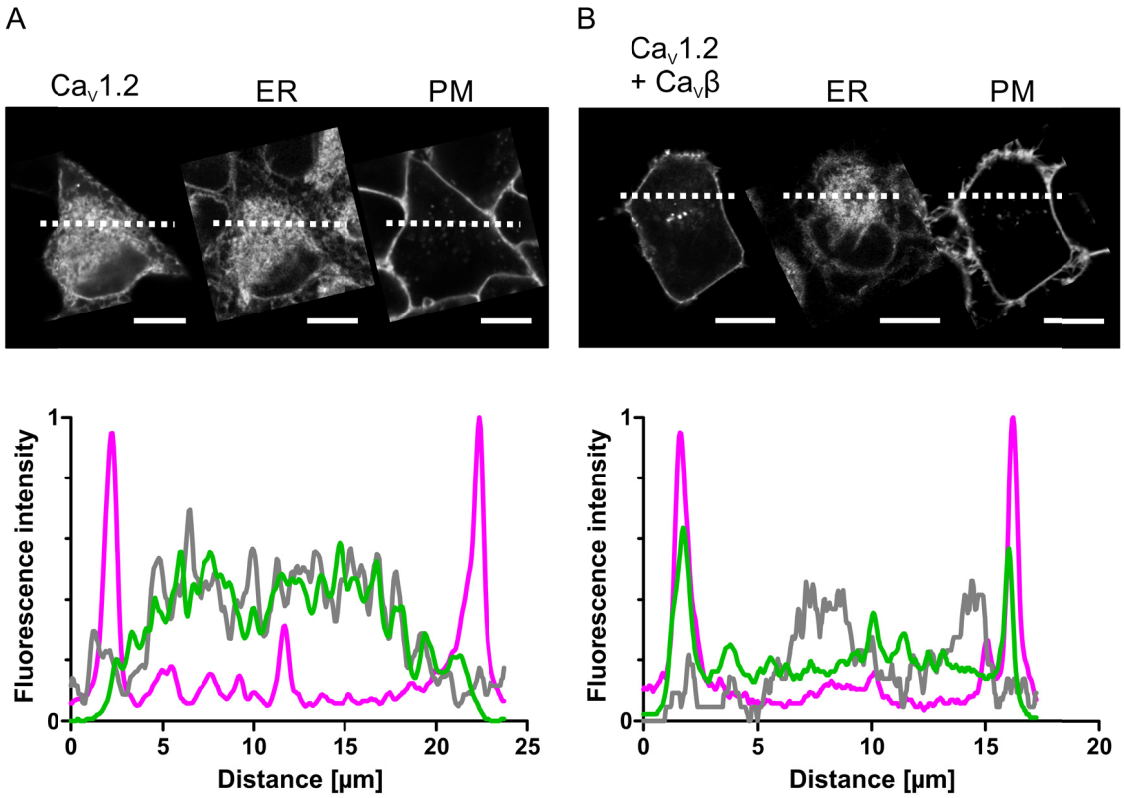

Figure 3.2: Fluorescence intensity of $Ca_V1.2$ in the presence of $Ca_V\beta$ coincides with the plasma membrane. HEK293 cells transfected with A) $Ca_V1.2$-mNeonGreen and B) $Ca_V1.2$-mNeonGreen and unlabeled $Ca_V\beta$. Both cells are stained with ER Tracker (ER) and CellMask (PM). The dotted line shows the linear region of interest (ROI). The graphs below the images visualize the fluorescence intensities of all images along the ROI. $Ca_V1.2$ is shown in green, the ER in grey and the plasma membrane (PM) in magenta. Overlapping curves show a colocalization. Scale bars = 10 µm.

The plasma membrane localization of $Ca_V1.2$ was used as the criteria in this study to validate the expression of unlabelled $Ca_V\beta$ in cotransfected cells.

In order to investigate the time course of $Ca_V1.2$ expression at the level of protein, cells transfected either with $Ca_V1.2$ alone or together with $Ca_V\beta$ were seeded on coverslips at a defined density of 1 x 10^5 cells per coverslip, and fixed at seven time points after transfection (10, 15, 20, 35, 40, 44, 60 h). To be able to correlate $Ca_V1.2$ with $Ca_V\beta$ expression levels, $Ca_V\beta$ was coupled to an mRFP fluorescent protein. All fixed cells were imaged with laser scanning confocal microscopy and 10 images from different fields of view of the glass coverslips were taken. The total number of non-fluorescent and of fluorescent cells per image of 0.6 mm^2 were counted using the software ImageJ and plotted against the time (Figure 3.3).

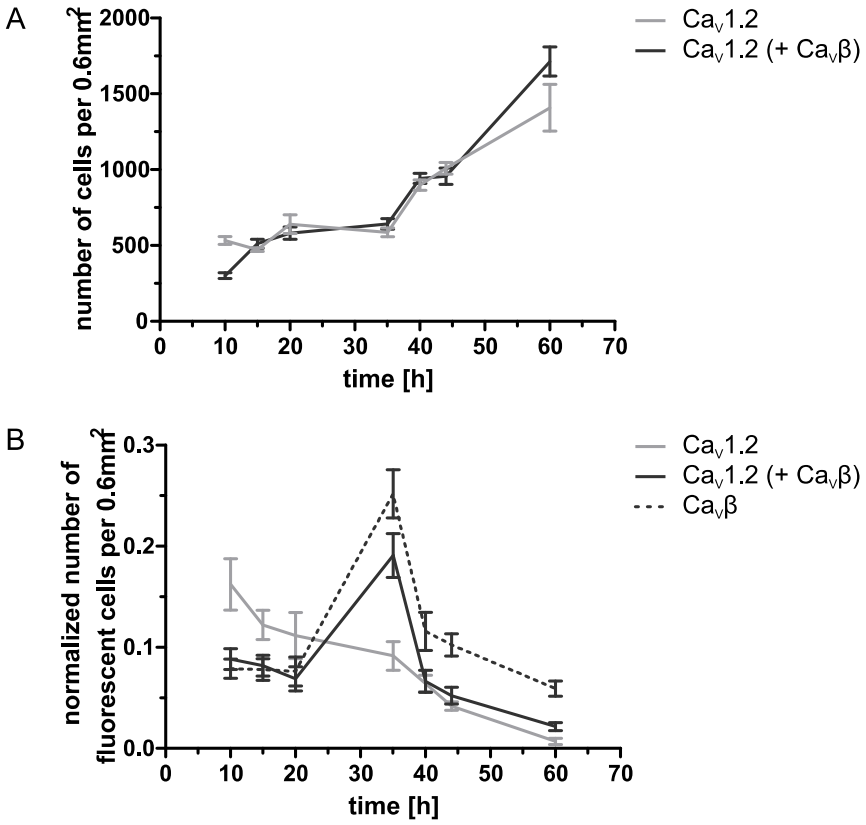

Figure 3.3: The number of cells expressing fluorescent $Ca_V1.2$ decreases in the absence of $Ca_V\beta$. The time course of the number of cells per 0.6 mm^2 at different time points after transfection with either $Ca_V1.2$ alone (light grey line) or together with $Ca_V\beta$ (dark grey line) are plotted. A) The total number of cells per 0.6 mm^2 and B) the number of cells normalized to the total number of cells per 0.6 mm^2 expressing fluorescent $Ca_V1.2$. Fluorescent $Ca_V\beta$ is shown by the dotted dark grey line. All values are plotted with SEM.

The growth curves of cells expressing either $Ca_V1.2$ alone or with $Ca_V\beta$ are very similar (Figure 3.3A). The curves show a lag period of around 35 hours. This result shows that during this experimental elapsed time expression of $Ca_V1.2$ alone or with $Ca_V\beta$ is not differentially affecting cell survival.

The number of fluorescent cells was normalized to the respective total number of cells. Since the plasmid encoding the proteins of interest is only transiently expressed, it is not passed to the next generation and the percentage of fluorescent cells decreases at around 35 h after transfection. However, differences are observed in cells expressing $Ca_V1.2$ alone or with $Ca_V\beta$. The number of cells expressing fluorescently labelled $Ca_V1.2$ alone (light grey line) does not significantly changes within the first 35 h after transfection. When coexpressing $Ca_V1.2$ with $Ca_V\beta$ the number of fluorescent cells for both subunits increases, reaching a peak at 35 h after transfection when cells are not being divided. This indicates that the time transfected cells starts to translate the fluorescent labelled channel extends over 35 h after transfection. Then a maximum of expressing cells is reached and no more cells start to translate the channel, but notice that the number of cells expressing $Ca_V1.2$ alone does not increase in the same time. This suggests that in the absence of $Ca_V\beta$ the channel is being rapidly degraded from the ER and $Ca_V\beta$ prevents $Ca_V1.2$ from this degradation. This result is consistent with previous hypotheses (Altier et al. 2011).

3.1.1 Injection of purified $Ca_V\beta$ into cells expressing $Ca_V1.2$

To observe the effect of acute exposition of $Ca_V\beta$ on $Ca_V1.2$, I followed a different strategy to bring fluorescently labelled protein into cells already expressing the pore-forming subunit. Recombinant $Ca_V\beta2a$ subunit requires higher concentration of NaCl (> 300 mM), however a shorter derivative, containing the two highly conserved domains SH3 and GK (SH3-GK) is stable at lower NaCl concentration (Stolting et al. 2015) and thus appropriate to be used for injection into the intracellular space and cell healthiness. The SH3-GK was expressed in *E.coli* and after purification it was labelled *in vitro* (kindly provided by Nadine Jordan) with AlexaFluor647 following the manufacturer's instruction (Invitrogen). SH3-GK-AlexaFluor647 purified protein was injected within the perinuclear region of adherent HEK293 cells expressing $Ca_V1.2$ fluorescently labelled with YFP and imaged with laser scanning confocal microscopy (Figure 3.4).

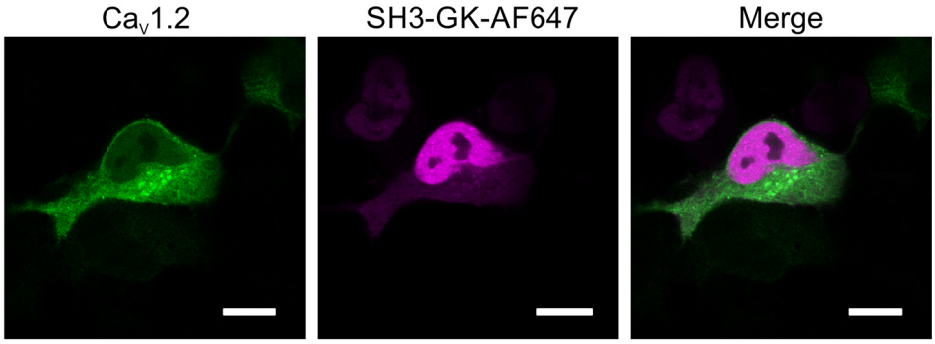

Figure 3.4: Injection of $Ca_V\beta$ in $Ca_V1.2$ expressing cells results in a translocalization of $Ca_V\beta$ to the nucleus. Laser scanning confocal images of HEK293 cell expressing $Ca_V1.2$ (green, left picture), injected with the two conserved domains SH3 and GK of $Ca_V\beta$ labelled to AlexaFluor647 (SH3-GK-AF647). The injected protein is exclusively located in the nucleus (middle picture). Scale bar = 10 µm.

Cells injected with SH3-GK-AlexaFluor647 showed an exclusive localization of the protein in the nucleus. $Ca_V1.2$ distribution was not affected by the injected SH3-GK-AlexaFluor647 and no cell showed a plasma membrane staining. To exclude impacts of the dye AlexaFluor647 and molecular mass of the injected protein, cells were injected with the dye alone (AF647) and with Immunoglobin G coupled to AlexaFluor647 (IgG-AF647) with a molecular mass of around 150 kDa (Figure 3.5).

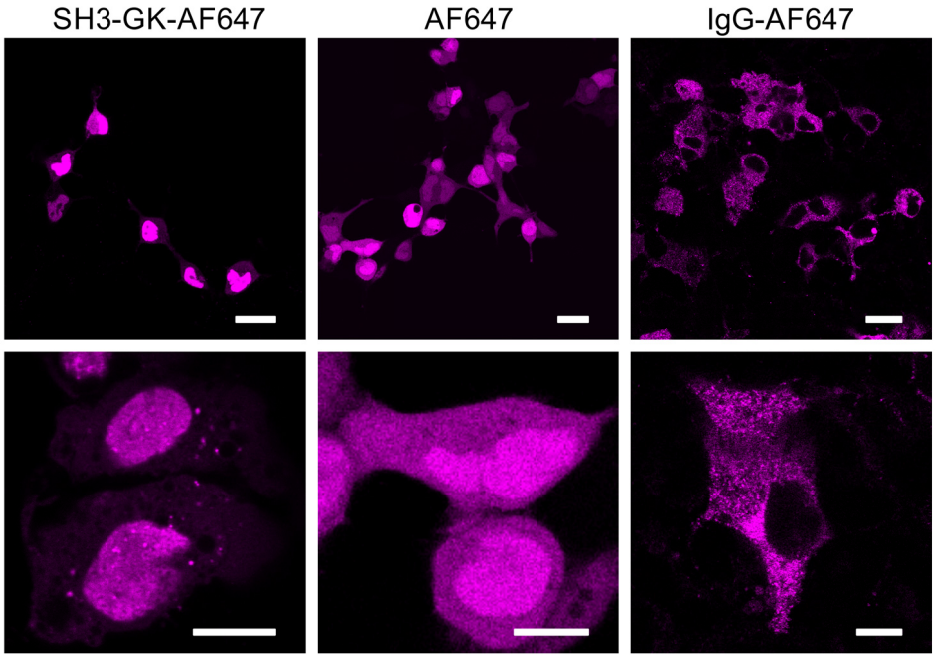

Figure 3.5: Injection controls. Laser scanning confocal images of HEK293 cells injected with $Ca_V\beta$ AlexaFluor647 (SH3-GK-AF647) in the left column, with AlexaFluor647 (AF647) in the middle column and with Immunoglobin G coupled to AlexaFluor647 (IgG-AF647) in the right column. The upper row always has a scale bar = 25 µm, the lower row shows a higher magnification with a scale bar = 10 µm.

Due to the fact that large proteins (> 40 kDa) are not able to actively pass through nuclear pores, it was expected that IgG-AF647 with a molecular mass of 150 kDa is not translocated to the nuclei. Indeed, cells injected with IgG-AF647 resulted in a pointed distribution outside the nucleus while cells injected with AlexaFluor647 alone (1.25 kDa) showed an equal distribution of the dye over the whole cell including the nucleus. $Ca_V\beta$-SH3-GK coupled to AlexaFluor647 has a molecular mass of around 60 kDa and it is expected to be excluded from the nuclei, however, is has been demonstrated that other $Ca_V\beta$ isoforms can be translocated to the nucleus but the mechanism responsible for this translocation is unknown (Miranda-Laferte et al. 2014). The results showing that SH3-GK-AlexaFluor647 is found in the nucleus imply that a potential nuclear export signal either is missing in this shorter construct or a posttranslational modification necessary for this is being inhibited in the recombinant protein. Although these results are very interesting for further studies related to nuclear localization of $Ca_V\beta$ injection, I discarded this strategy based on protein injection as a valuable tool for studying trafficking of $Ca_V1.2$.

3.1.2 Inducible cell line for $Ca_V\beta$

The next step to investigate the dependence of $Ca_V1.2$ already transduced on $Ca_V\beta$ was to induce the expression of $Ca_V\beta$ after the expression of $Ca_V1.2$. Therefore Flp-In T-REx-cells containing the inducible gene of $Ca_V\beta$2a-mCherry were transfected with $Ca_V1.2$-mNeonGreen. Before and after induction of the expression of $Ca_V\beta$2a-mCherry cells were imaged with laser scanning confocal microscopy (Figure 3.6).

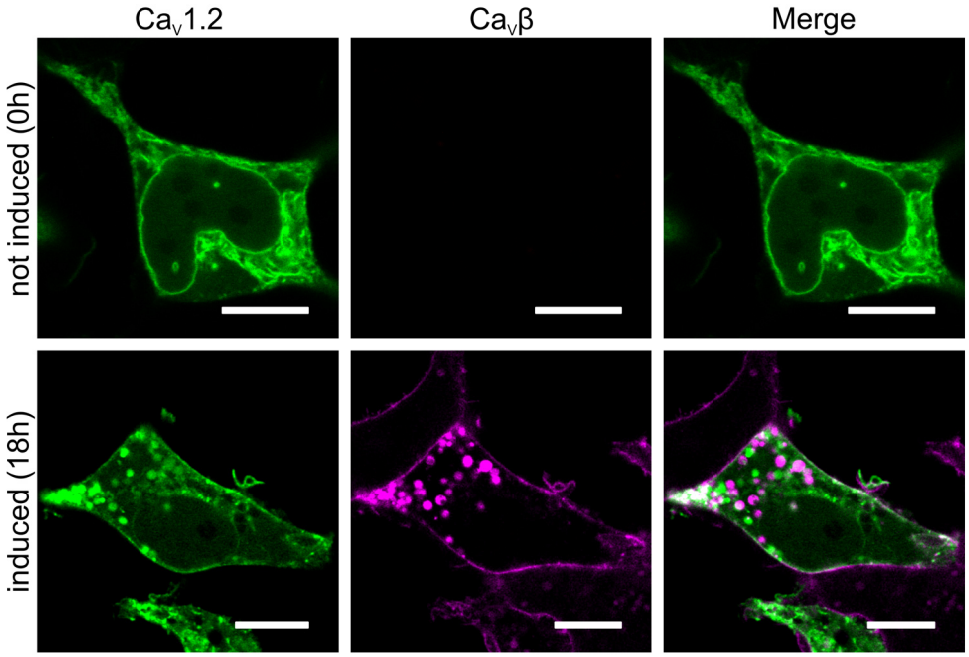

Figure 3.6: Inducing Flp-In T-REx Ca$_V$β2a-mcherry cells results in a release of the already expressed channel from the ER and its transport to the plasma membrane. Laser scanning confocal images of Flp-In T-REx-Ca$_V$β2a-mcherry cells transfected with Ca$_V$1.2 coupled to mNeonGreen (green, left column). The upper row shows a cell before induction and the lower row after 18 h induction time with tetracycline. The middle column shows Ca$_V$β2a-mcherry (magenta) and the right column the merge. Scale bars = 10 µm.

Before induction of Ca$_V$β expression Ca$_V$1.2-mNeonGreen is located only in the inner of the cell. To determine the temporal dependency of Ca$_V$1.2 residing in the ER on Ca$_V$β, cells were imaged every 10 min after induction with the spinning disk confocal microscope under stable cell culturing conditions (37°C and 5% CO_2). Around 10 h after induction Ca$_V$β is expressed at the protein level and Ca$_V$1.2 retained in the ER starts to move towards the plasma membrane. A clear membrane staining of both subunits can be recognized 18 h after induction (Figure 3.6). This shows that Ca$_V$1.2 and Ca$_V$β do not necessary need to be transduced at the same time. For a certain time period the α_1-subunit remains in the ER in a conformation that is competent for association with Ca$_V$β.

In summary, Ca$_V$β is required for Ca$_V$1.2 ER exit but cotranslation is not mandatory for the release. A permissive encounter is allowed for at least 30 hours, in which the translated α-subunit remains responsive until it is degraded in the absence of Ca$_V$β. This suggests that Ca$_V$β is the limiting step for the channels biosynthetic pathway.

3.2 Biosynthetic secretory pathway of $Ca_V1.2$

In order to follow the pathway of the channel after being released from the ER, different staining methods in living and in fixed cells were used.

The first step in the biosynthetic secretory pathway is the release of the channel at specific location within the ER, the ER-exit sites (ERES). Cells transfected with the $Ca_V1.2$ alone or together with $Ca_V\beta$ were stained with an antibody for SEC16, a marker protein for ERES. From ERES folded proteins are brought to the Golgi network, where they are sorted to their final destination. GCC1, a marker for *trans*-Golgi-system was used to study this step during the channels journey.

To make sure that ERES and Golgi can be differentiate despite their spatial proximity cells were first stained with both markers (Figure 3.7)

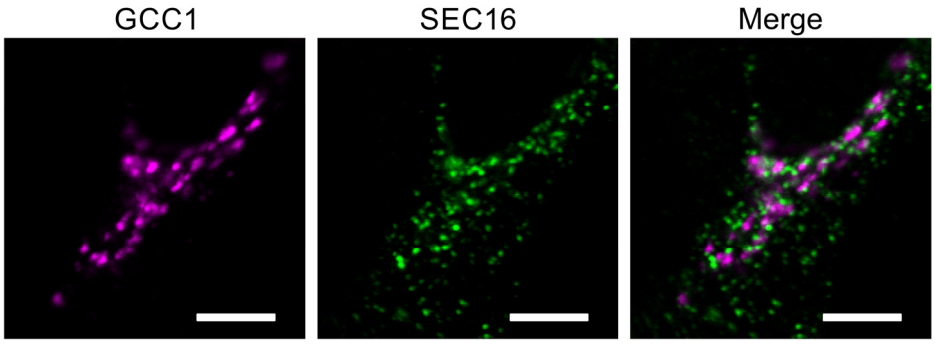

Figure 3.7: The resolution of ERES- and Golgi-marker is high enough to differentiate between the compartments. Laser scanning confocal images of HEK293 cells fixed and immunochemically stained with antiGCC1 (magenta), a *trans*-Golgi marker and antiSEC16 (green), a marker for ER exit sites. Scale bars = 5 µm.

Figure 3.7 shows that both markers are distributed punctuated within the cytoplasm of the cell, though mainly in the perinuclear region. However no overlap of SEC16 and GCC1 can be detected. Therefore, we assume that the resolution is high enough to distinguish between ERES and Golgi and we used SEC16 and GCC1 as markers to investigate the early biosynthetic secretory pathway of $Ca_V1.2$.

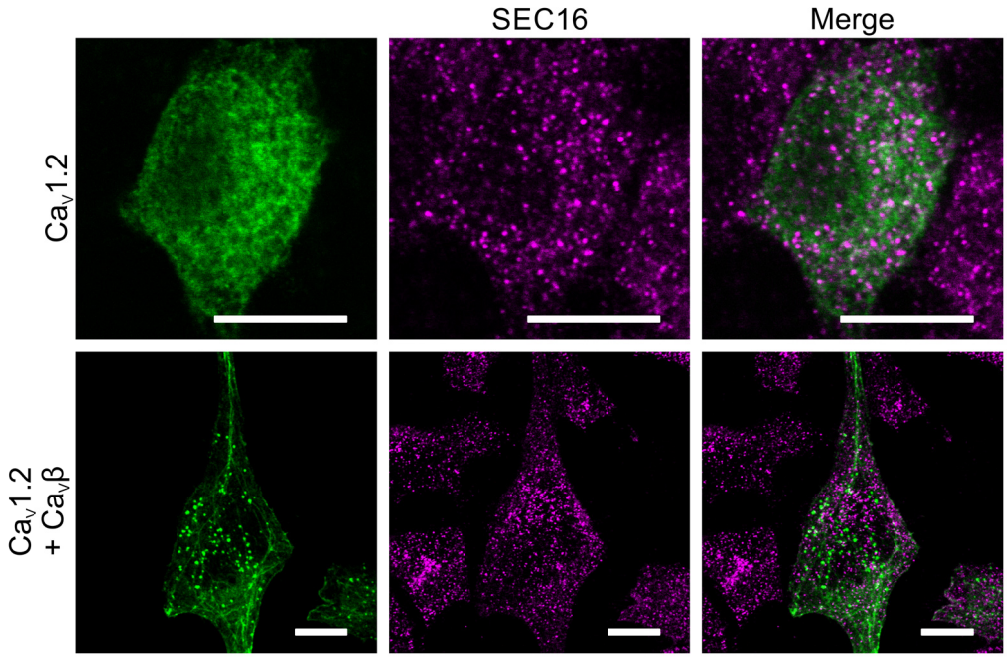

Figure 3.8: $Ca_V1.2$ shows no colocalization with ERES, either with or without $Ca_V\beta$. Laser scanning confocal images of HEK293 cells expressing $Ca_V1.2$-mNeonGreen (upper row, green) or $Ca_V1.2$-mNeonGreen and $Ca_V\beta$ (unlabelled) (lower row, green), fixed and stained with antiSEC16 (magenta). The right column shows the merge. Scale bars = 10 µm.

As shown previously, $Ca_V1.2$ expressed alone accumulates in the ER. Consistently, in fluorescence images neither apparent colocalization between ERES and $Ca_V1.2$ nor spatial correlation in the fluorescence emission intensity plots along linear ROIs for both channels were observed (Figure 3.8 and Figure 3.9). These indicate that in the absence of $Ca_V\beta$, the channel is not translocated to the ERES and suggest a new mechanism by which $Ca_V\beta$ promotes release of $Ca_V1.2$ from the ER i.e. through mobilization of $Ca_V1.2$ to the ERES. However, no colocalization of $Ca_V1.2$ and SEC16 in cells coexpressing both subunits, $Ca_V1.2$ and $Ca_V\beta$ was observed (Figure 3.8 and Figure 3.9). The respective fluorescence intensities, given in Figure 3.9 show no common course, as if no channel localizes within the ER exit sites neither in combination with the β-subunit. Since ER exit through ERES is a mandatory step for targeting of membrane proteins to the plasma membrane, we assumed that $Ca_V\beta$ is very efficient in releasing the channel from the ER, so this step could not be observed. A hint for this also comes from experiments shown above, where $Ca_V\beta$ appeared to be required for an efficient and fast ER exit of $Ca_V1.2$ (Figure 3.1).

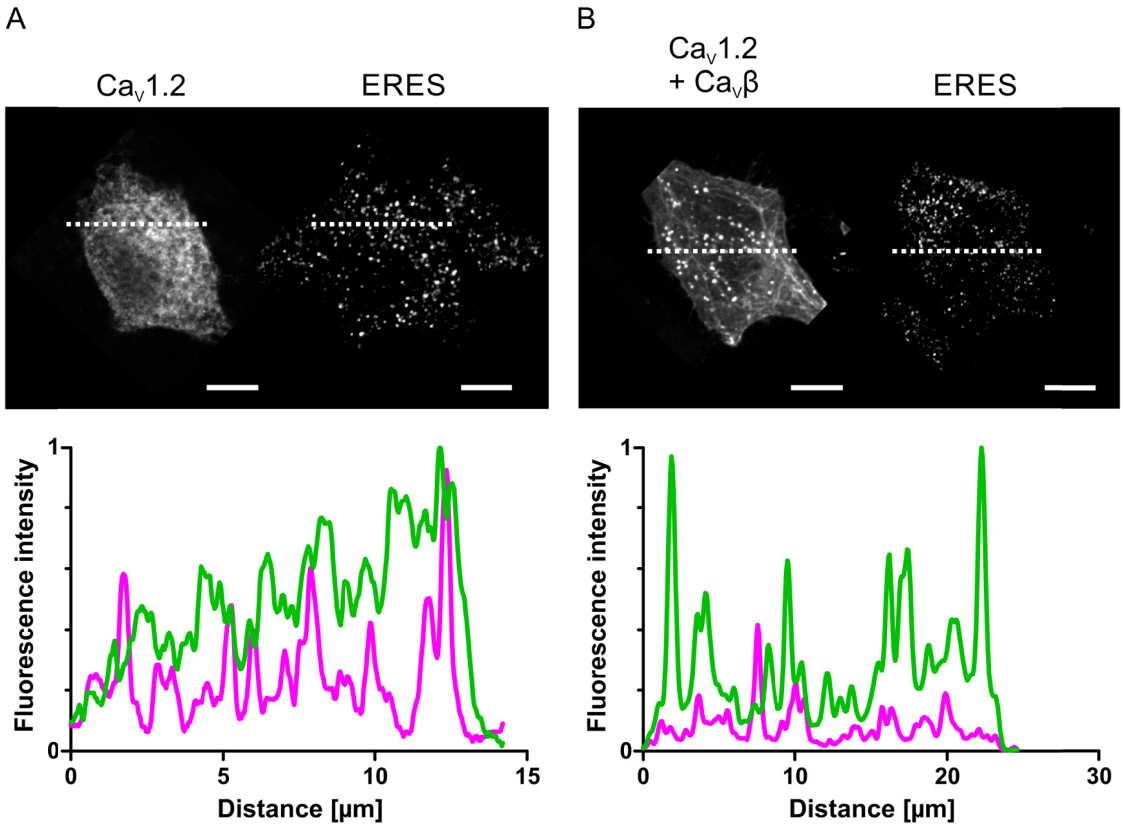

Figure 3.9: Fluorescence intensities of $Ca_V1.2$ gives no overlap with ERES. HEK293 cells transfected with A) $Ca_V1.2$-mNeonGreen and B) $Ca_V1.2$-mNeonGreen and unlabelled $Ca_V\beta$. Both cells are stained with antiSEC16 (ERES) The dotted line shows the linear region of interest (ROI). The graphs below the images visualize the fluorescence intensities of all images along the ROI. $Ca_V1.2$ is shown in green, antiSEC16 in magenta. Scale bars = 10 µm.

Colocalization experiments in HEK293 cells expressing either both subunits or only $Ca_V1.2$ alone and stained with antiGCC1 showed no colocalization of GCC1 with the channel alone, but a well-defined colocalization of GCC1 with $Ca_V1.2$ coexpressed with $Ca_V\beta$ as evidenced in the merge image by the white color (Figure 3.10).

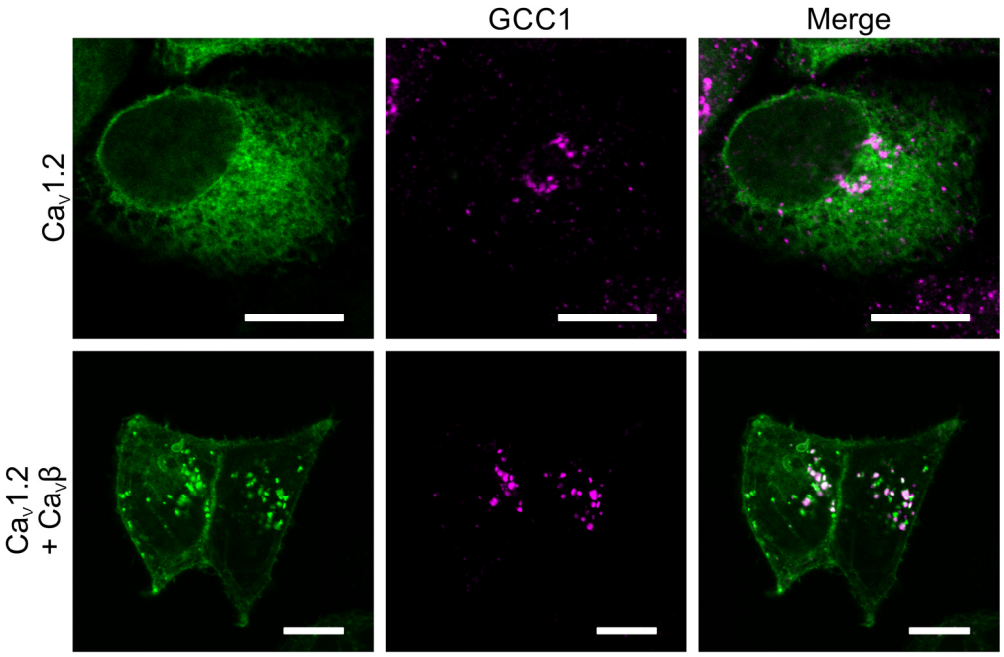

Figure 3.10: $Ca_V1.2$ is localized in the Golgi only in the presence of $Ca_V\beta$. Laser scanning confocal images of HEK293 cells expressing $Ca_V1.2$-mNeonGreen (upper row, green) or $Ca_V1.2$-mNeonGreen and $Ca_V\beta$ (unlabelled) (lower row, green), fixed and stained with antiGCC1 (magenta). The right column shows the merge. Scale bars = 10 µm.

In agreement with this, the fluorescence intensity curves of the Golgi marker with the respective curve of the channel with and without β-subunit along linear ROIs confirm that without $Ca_V\beta$ the channel shows no colocalization with the Golgi-marker while in cotransfected cells the fluorescence intensities of $Ca_V1.2$ and GCC1 show a very similar spatial distribution with overlapping peaks (Figure 3.11). This emphasizes the conclusion that $Ca_V1.2$ enters the Golgi system only in the presence of $Ca_V\beta$ and the lack of colocalization with ER exit sites is likely due to a very efficiently release from the ER (cf. Figure 3.9 right column), visible in completely distinct curves.

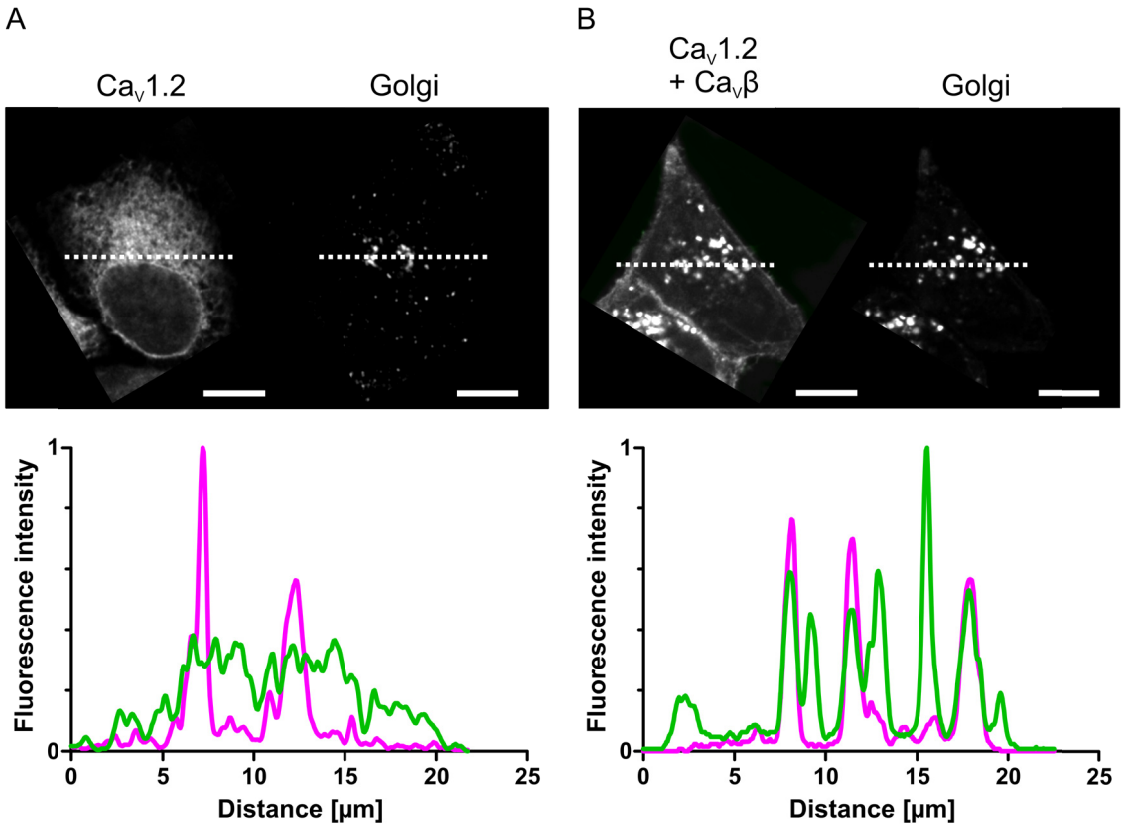

Figure 3.11: Localization of $Ca_V1.2$ with Golgi in the presence of $Ca_V\beta$ is supported by overlapping fluorescence intensities. HEK293 cells transfected with A) $Ca_V1.2$-mNeonGreen and B) $Ca_V1.2$-mNeonGreen and unlabelled $Ca_V\beta$. Both cells are stained with antiGCC1 (Golgi). The dotted line shows the linear region of interest (ROI). The graphs below the images visualize the fluorescence intensities of all images along the ROI. $Ca_V1.2$ is shown in green, antiGCC1 in magenta. Overlapping curves show a colocalization. Scale bars = 10 µm.

To quantify the effect of $Ca_V\beta$ during the early secretory pathway the Mander's overlap coefficient (MOC) of the labelled $Ca_V1.2$, in the presence and absence of $Ca_V\beta$, and the markers for the above used compartments, ER, ERES, and Golgi was calculated. For comparison, the correlation coefficient for the channel and the plasma membrane marker was also included. To evaluate the MOC, only the values of $Ca_V1.2$–fluorescence overlapping the respective fluorophores of the compartment were considered. Since the individual compartments differ in their structure, size, pattern and spatial distribution, their overlapping fractions to $Ca_V1.2$ could not be compared. Figure 3.12A summarizes the MOC analysis for the different organelles in the presence and absence of $Ca_V\beta$. The differences in the MOC values in the presence and absence of $Ca_V\beta$ for each compartment are shown in Figure 3.12B.

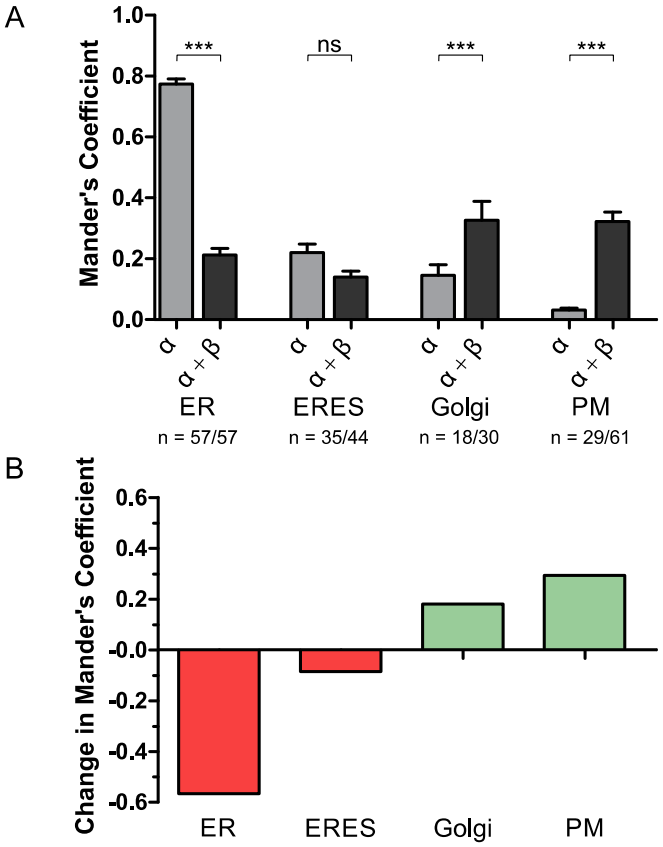

Figure 3.12: Colocalization of $Ca_V1.2$ with ER, ERES, Golgi and plasma membrane. A) Fraction of $Ca_V1.2$-fluorescence overlapping the respective compartment endoplasmic reticulum (ER), ER exit sites (ERES), Golgi and plasma membrane (PM) given by the Mander's overlap coefficient. Bars in light grey indicate $Ca_V1.2$ alone and bars in dark grey indicate $Ca_V1.2$ coexpressed with $Ca_V\beta$. Each bar represents the mean of n analyzed cells (given below the bars) with the 95% confidence interval. Statistical differences induced by the presence of $Ca_V\beta$ were tested with One-Way ANOVA followed by post hoc Bonferroni's Multiple Comparison test ($p \leq 0.001$). Stars represent statistical significances between the two series; ns = no significant. B) Changes in Mander's coefficient induced by the presence of $Ca_V\beta$ corresponding to the upper graph (A). Red bars indicate a loss of overlapping fraction of $Ca_V1.2$ to the respective compartment, green bars indicate a profit.

We have observed before (Figure 3.1) that in the absence of $Ca_V\beta$, virtually all channel expressed accumulates in the ER and neither further intracellular transport nor plasma membrane targeting take place. Consistently, under these conditions the major overlapping proportion of $Ca_V1.2$ can be found with the ER and the smallest with the plasma membrane, reaching mean values of MOC of 0.8 and 0.07, respectively. For ERES and Golgi, a MOC value of around 0.2 was estimated in cells expressing only $Ca_V1.2$ subunit. Compared to computer-simulated image sets with exactly known degrees of colocalization from a colocalization benchmark source (Zinchuk and Grossenbacher-Zinchuk 2014, Zinchuk et al. 2013) a MOC value of 0.2 was estimated for two color channels with 0% colocalization. Thus

a MOC below 0.2 may result from a random co-presence of two fluorophores in one pixel. Since the MOC does not examine similar structures of the fluorescently labelled components but only fluorophores within the same pixel the widespread distribution of $Ca_V1.2$ through the whole cell in the absence of $Ca_V\beta$ might give partially overlap of the fluorescences with the punctual arrangement of the marker proteins only due to a co-occurrence of two possibly unrelated fluorophores in the same pixel. A hint therefore could be given by the qualitative analysis in which $Ca_V1.2$ alone with ER, ERES or Golgi showed no colocalization. But whether the small fraction of channels colocalizing with ERES in the absence of $Ca_V\beta$ reflects unspecific coloalization or a type of leaky transport of $Ca_V\alpha$ remains elusive.

In the presence of $Ca_V\beta$ the overlapping fraction of $Ca_V1.2$ shows a different organelle distribution that is consistent with the entering of the channel to the biosynthetic pathway until being inserted into the plasma membrane. While the MOC for $Ca_V1.2$ with the plasma membrane increases significantly from 0.07 to 0.32 the one for ER decreases from 0.8 to 0.21. In agreement with the plasma membrane insertion, the degree of colocalization with the Golgi also increases.
The effect of $Ca_V\beta$ on the early biosynthetic pathway can best be described by the gain and loss of overlapping fractions with the respective compartments (Figure 3.12B). The fraction of $Ca_V1.2$ overlapping with ER decreases significant by nearly 70% in the presence of $Ca_V\beta$. A slight decrease is detected also between the overlapping fractions of $Ca_V1.2$ with ER exits sites, but this difference is not statistically significant. However, the overlapping proportion of $Ca_V1.2$ with the Golgi system, as well as the plasma membrane increases with the presence of $Ca_V\beta$.

All together the above results indicate that during the biosynthetic pathway $Ca_V1.2$ remains within the ER until $Ca_V\beta$ provides its release for further translocation to the Golgi system where it is sorted out to the plasma membrane.

3.3 Transport of $Ca_V1.2$ along cytoskeletal components

Membrane proteins need to be packed into vesicles in order to be transported towards the plasma membrane. This vesicular transport of membrane proteins is assumed to occur along cytoskeletal filaments of cells, microtubules formed by tubulin as well as actin filaments (F-actin). It is believed that long range transport is mediated by microtubules while short-range movement, in particular, prior plasma membrane insertion, is mediated by F-actin.

Since only in cells expressing both α- and β-subunits the channel can be transported to the plasma membrane, hereinafter, the biosynthetic trafficking pathway after leaving the Golgi apparatus was followed only in cotransfected cells with $Ca_V1.2$-mNeonGreen and unlabelled $Ca_V\beta$. The presence of the latter is verified by the membrane staining resulting from $Ca_V1.2$ inserted into the cell surface (cf. Figure 3.1).

To investigate transport of $Ca_V1.2$ along cytoskeletal components, microtubules and F-actin were stained with SiR-Tubulin and SiR-Actin, respectively (cf. 2.6.1). Figure 3.13 shows a representative cell transfected with $Ca_V1.2$-mNeonGreen and unlabelled $Ca_V\beta$ and stained alive with SiR-Tubulin:

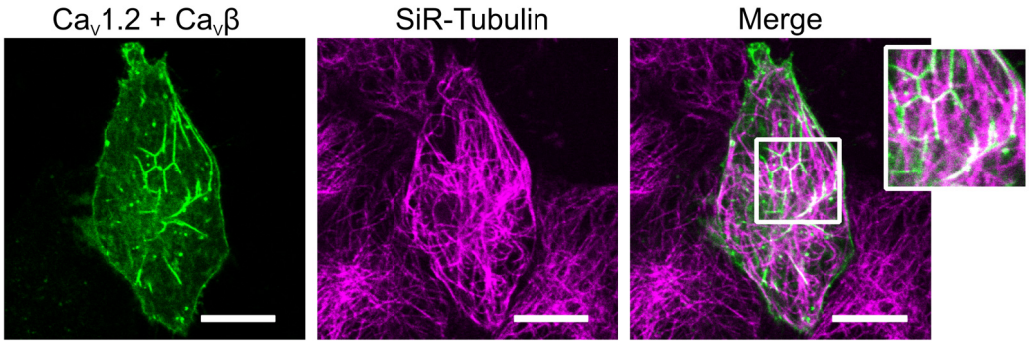

Figure 3.13: Filament-like $Ca_V1.2$ partially overlaps with SiR-Tubulin. Laser scanning confocal images of living HEK293 cell tranfected with $Ca_V1.2$-mNeonGreen (green) and unlabelled $Ca_V\beta$ (left image) and stained with SiR-Tubulin 24 h after transfection. The merge picture and the magnification shows a partially colocalization. Scale bars = 10 µm.

As expected, the channel shows membrane staining verifying the presence of $Ca_V\beta$. $Ca_V1.2$ is also found intracellularly in filament-like structures (Figure 3.13). SiR labelled tubulin in living cells distributes through the entire cell from a perinuclear region to the cell periphery

forming an intricate network (Figure 3.13 middle image). The filament–like structures formed by $Ca_V1.2$ appears to partially follow the distribution of tubulin filaments.

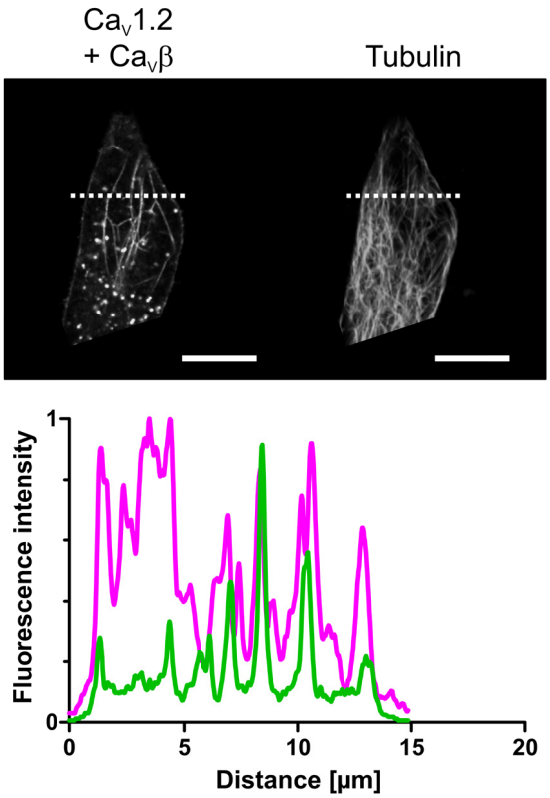

Figure 3.14: Fluorescence intensity of $Ca_V1.2$ overlaps partially with SiR-Tubulin. HEK293 cell transfected with $Ca_V1.2$-mNeonGreen and unlabelled $Ca_V\beta$, stained with SiR-Tubulin (Tubulin). Due to the crowdedness of the microtubule network and for better visualization here a different cell than in Figure 3.13 was used. The dotted line shows the linear region of interest (ROI). The graph below the image visualizes the fluorescence intensities of all images along the ROI. $Ca_V1.2$ is shown in green, the cytoskeleton marker in magenta. Overlapping curves show a colocalization. Scale bars = 10 µm.

Despite the crowdedness of the cytoskeletal network the fluorescence intensity plot across a ROI for SiR-Tubulin stained cells showed partial spatial overlap with the emission fluorescence of Cav1.2-mNeonGreen (Figure 3.14). Furthermore, the MOC estimated for the degree of colocalization between $Ca_V1.2$ and tubulin increases from 0.18 to 0.51 upon coexpression of $Ca_V\beta$ (Figure 3.15). These results insinuate that $Ca_V1.2$ uses microtubule tracks for delivery to the plasma membrane.

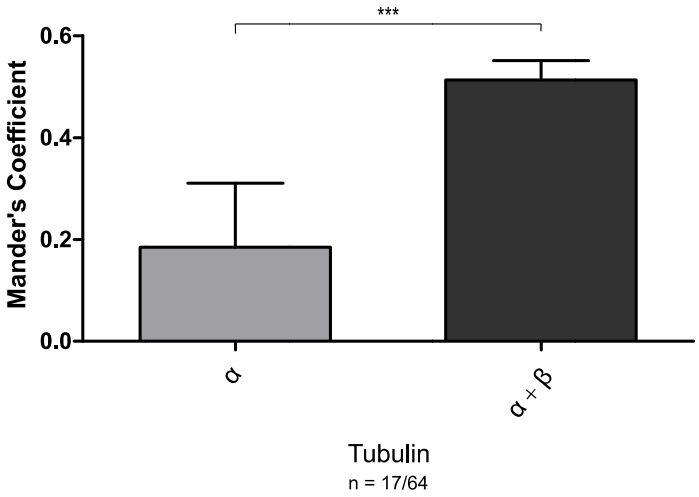

Figure 3.15: Colocalization of $Ca_V1.2$ with tubulin increases in the presence of $Ca_V\beta$. Fractions of $Ca_V1.2$-fluorescence overlapping the SiR-Tubulin-fluorescence given by the Mander's overlap coefficient. Bars indicate either $Ca_V1.2$ alone (α) or $Ca_V1.2$ coexpressed with $Ca_V\beta$ (α+β). Each bar represents the mean of n analyzed cells (given below the bars) with the 95% confidence interval. Statistical differences between the overlap in presence or absence of $Ca_V\beta$ were tested with One-Way ANOVA followed by post hoc Bonferroni's Multiple Comparison test ($p \leq 0.001$). Stars represent statistical significances between the two series.

Living HEK293 cells expressing both, $Ca_V1.2$ and $Ca_V\beta$, were also stained with SiR-Actin Figure 3.16.

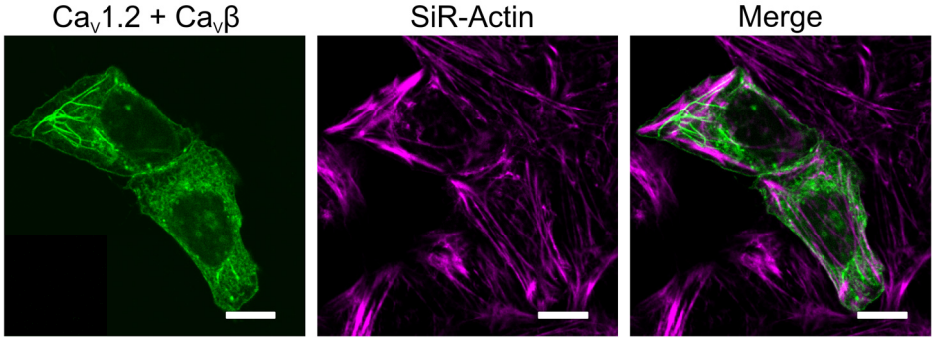

Figure 3.16: $Ca_V1.2$ shows no colocalization with SiR-Actin. Laser scanning confocal images of living HEK293 cells tranfected with $Ca_V1.2$-mNeonGreen (green) and unlabelled $Ca_V\beta$ (left image) and stained with SiR-Actin 24 h after transfection. The merge picture (right) shows no colocalization. Scale bars = 10 µm.

SiR-Actin appears to distribute more prominent near the plasma membrane and in comparison with microtubules, no apparent overlap between F-actin and $Ca_V1.2$ was visible (Figure 3.16 and Figure 3.17). However, recent studies from our group showed a direct interaction between $Ca_V\beta$ and F-actin and we proposed that a small fraction of the channels' population is

transiently associated with F-actin and this association supports recycling (Stolting et al. 2015).

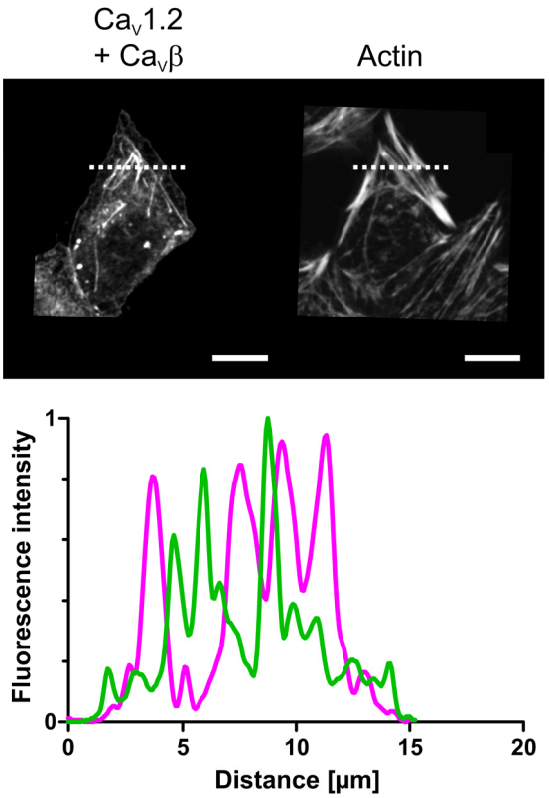

Figure 3.17: Fluorescence intensity of $Ca_V1.2$ distributes differently than SiR-Actin. HEK293 cell transfected with $Ca_V1.2$-mNeonGreen and unlabeled $Ca_V\beta$, stained with SiR-Actin (Actin). The dotted line shows the linear region of interest (ROI). The graphs below the images visualize the fluorescence intensities of all images along the ROI. $Ca_V1.2$ is shown in green, the cytoskeleton marker in magenta. Overlapping curves show a colocalization. Scale bars = 10 µm.

3.3.1 Pharmacological blocking of the cytoskeleton

To study the effect of altering the cytoskeletal network transport of $Ca_V1.2$, the polymerization of actin filaments and microtubules was blocked pharmacologically in heterologous expressing HEK293 cells. Treated cells were stained with SiR-Actin and SiR-Tubulin and subsequently imaged by laser scanning confocal microscopy.

In the absence of the microtubule depolymerizing drug, nocodazole, the tubulin-filaments are intact and marker proteins for ERES and Golgi (SEC16 and GCC1) showed a compact juxtanuclear distribution. Cotransfected HEK293 cells were treated with 33 µM nocodazole for 18 h, fixed and stained immunochemically with antibodies for tubulin, SEC16 (ER exit sites) and GCC1 (Golgi). Laser scanning confocal images are shown in Figure 3.18.

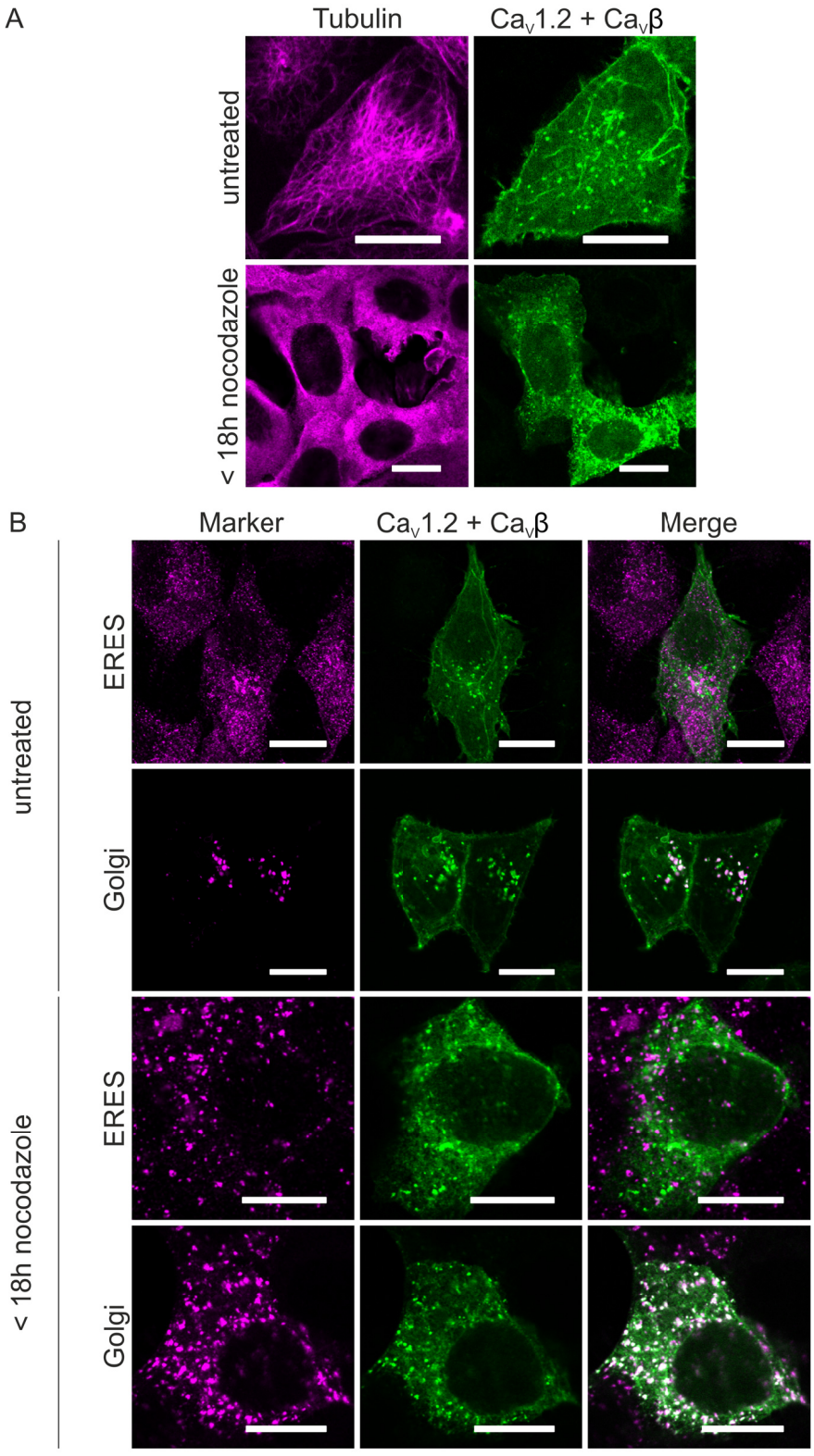

Figure 3.18: Nocodazole-treatment affects microtubules as well as compartments of the early secretory pathway. Laser scanning confocal images of HEK293 cells cotransfected with $Ca_V1.2$ fluorescently labelled with mNeonGreen and unlabelled $Ca_V\beta$ (middle column, green). Cells were untreated or pharmacology treated with 33 µM nocodazole, fixed and immunochemically stained with A) antiTubulin or B) antiSEC16 (ERES) or antiGCC1 (Golgi), respectively (all magenta). Scale bars = 10 µm.

After 18 h treatment microtubules had completely depolymerized and tubulin-fragments are evenly distributed over the whole cytoplasm. The lack of apparent colocalization between the channel and ERES is not modified by nocodazole treatment. The ER exit sites that in untreated cells appeared spread over a large area become randomly scattered throughout the cytoplasm. The compact structure of the Golgi complex disappeared and scattered structures can be observed. This observation is consistent with previous reports showing that an intact microtubule-based cytoskeleton is necessary for maintaining the *trans*-Golgi network organization (Cole et al. 1996). Despite of this, we observe that disruption of the tubulin network does not inhibit mobilization of channels to the Golgi as observed by a high degree of colocalization with the Golgi marker GCC1. This suggests that ER-Golgi transport is independent of tubulin network.

In contrast, after nocodazole treatment the filament-like structures formed by $Ca_V1.2$ and the membrane staining vanished, suggesting that the vesicular transport toward the plasma membrane is mediated by microtubules (Figure 3.18).

A comparison of the degree of colocalization in nocodazole treated and non-treated cells using Mander's overlap coefficient is charted in Figure 3.19.

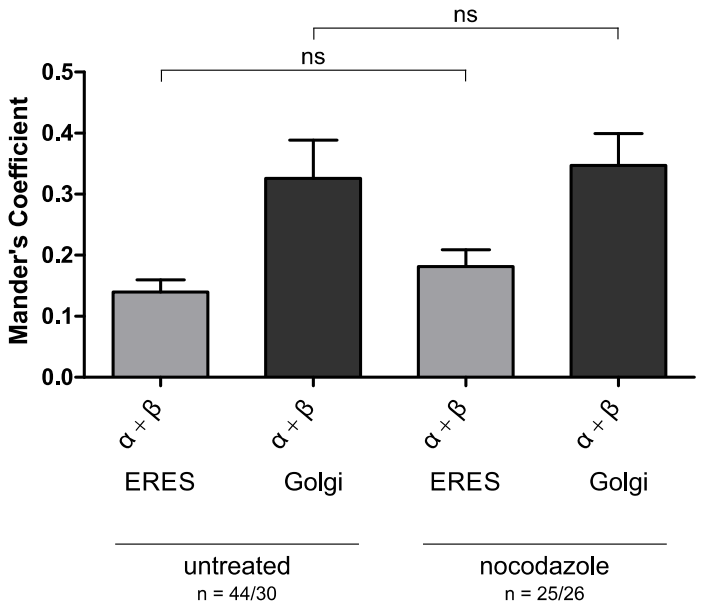

Figure 3.19: Colocalization of $Ca_V1.2$ with ERES and Golgi is not altered after nocodazole treatment. The graphic shows the fraction of $Ca_V1.2$-fluorescence (in presence of $Ca_V\beta$ (α + β)) overlapping the respective compartments ER exit sites (ERES) and Golgi in untreated and pharmacology treated cells with 33 µM nocodazole given by the Mander's coefficient. Each bar represents the mean of n analyzed cells (number given below the bars) with the 95% confidence interval. Statistical differences to the treatments were tested with One-Way ANOVA followed by post hoc Bonferroni's Multiple Comparison test ($p \leq 0.001$). ns = no significant.

The MOCs of untreated cells were compared with values from pharmacology treated cells with nocodazole. The mean values of the overlapping proportion of $Ca_V1.2$ in presence and absence of the microtubule disrupting drug remains unchanged for ERES and Golgi.

We conclude that translocation of the channel from the ER to Golgi does not require an intact microtubule-based cytoskeleton but transport to the plasma membrane requires a competent microtubule network.

To assess the role of F-actin in the transport of $Ca_V1.2$ along microtubules, cells were incubated with 10 µM of the actin polymerization inhibitor cytochalasin D and stained either for F-actin or tubulin. The cytochalasin D treatment effectively disrupted actin filaments (Figure 3.20 upper row). And most notably, colocalization of $Ca_V1.2$ with microtubules was preserved (Figure 3.20).

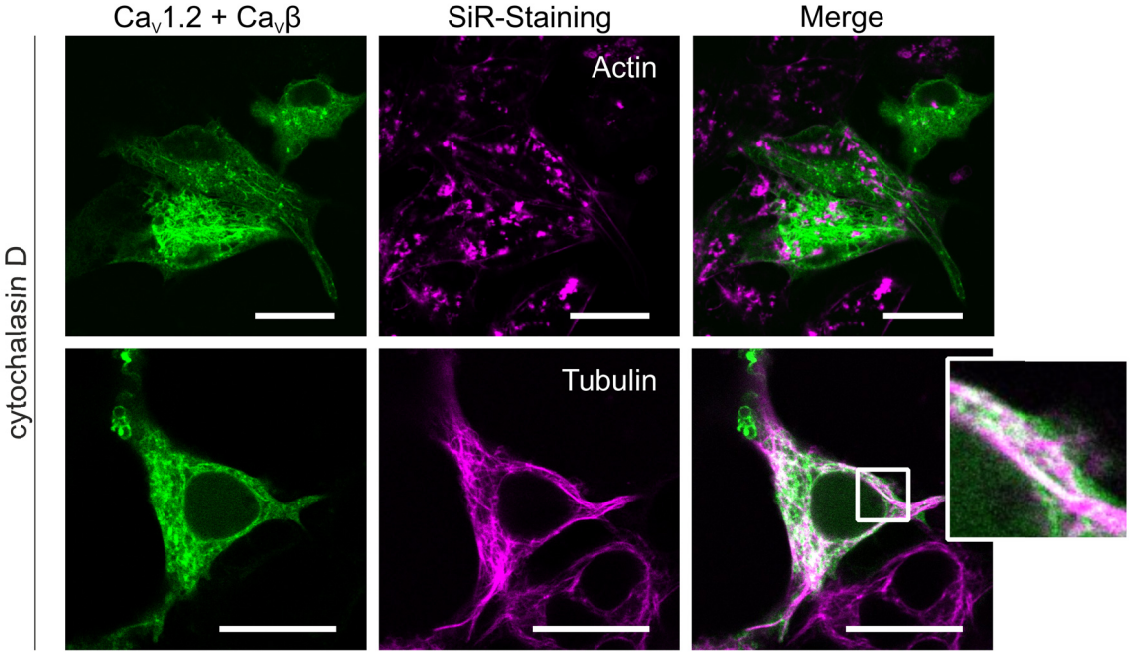

Figure 3.20: Actin disruption leads to a preserved colocalization of $Ca_V1.2$ with microtubules. Laser scanning confocal images of HEK293 cells cotransfected with $Ca_V1.2$ fluorescently labelled with mNeonGreen and unlabelled $Ca_V\beta$ (left column, green). Cells were pharmacology treated with 10 µM cytochalasin D, an actin blocker and stained with SiR-Actin and SiR-Tubulin (magenta), respectively. The merge of $Ca_V1.2$ and the cytoskeleton-marker is shown in the right column. Scale bars = 20 µm.

The MOC value of $Ca_V1.2$ with microtubules in the presence and absence of $Ca_V\beta$ was compared before and after treatment with cytochalasin D (Figure 3.21).

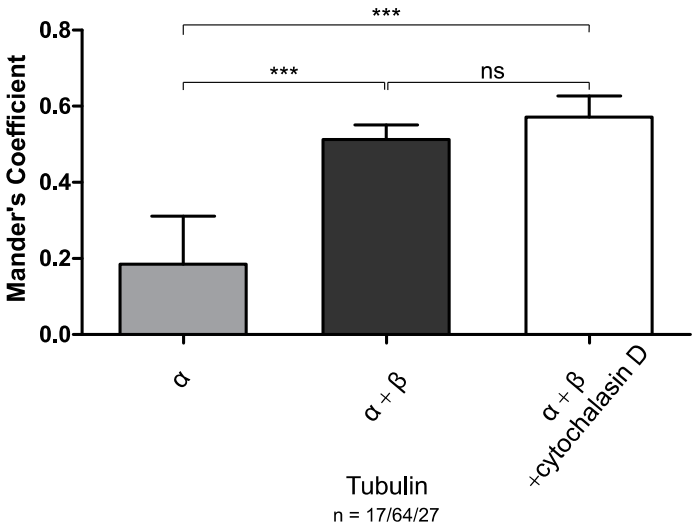

Figure 3.21: Colocalization of $Ca_V1.2$ with tubulin after F-actin disruption does not change. The graphic shows the fraction of $Ca_V1.2$-fluorescence overlapping with the SiR-Tubulin-fluorescence given by the Mander's overlap coefficient. Bars indicate either $Ca_V1.2$ alone (α), $Ca_V1.2$ coexpressed with $Ca_V\beta$ (α+β) and $Ca_V1.2$ and $Ca_V\beta$ after treatment with 10 µM cytochalasin D. Each bar represents the mean of n analyzed cells (given below the bars) with the 95% confidence interval. Statistical differences between the treated and untreated cells in presence or absence of $Ca_V\beta$ were tested with One-Way ANOVA followed by post hoc Bonferroni's Multiple Comparison test ($p \leq 0.001$). Stars represent statistical significances between the two series; ns = no significant.

The degree of colocalization between $Ca_V1.2$ and tubulin is not altered by F-actin disruption suggesting that transport along microtubules is independent from actin cytoskeleton. This is consistent with the separated spatial distribution of both components with actin being predominantly beneath the plasma membrane and tubulin irradiating from the cell center towards the periphery.

3.4 Retrograde trafficking of $Ca_V1.2$

Proteins inserted in the plasma membrane, undergo a quality control that determines their life time at the cell surface, the life span and their fate: recycling or degradation (Babst 2014). Endocytosed membrane proteins are packed into early endosomes from where they are delivered to recycling endosomes for reinsertion into the plasma membrane or to late endosomes for further degradation into lysosomes. To investigate the backward transport of $Ca_V1.2$ after internalization, we used special marker proteins for the endosomal pathway: Rab5 for early endosome, Rab7 for late endosome, Rab11 for recycling endosome and Lamp1 for lysosomes (Figure 3.22).

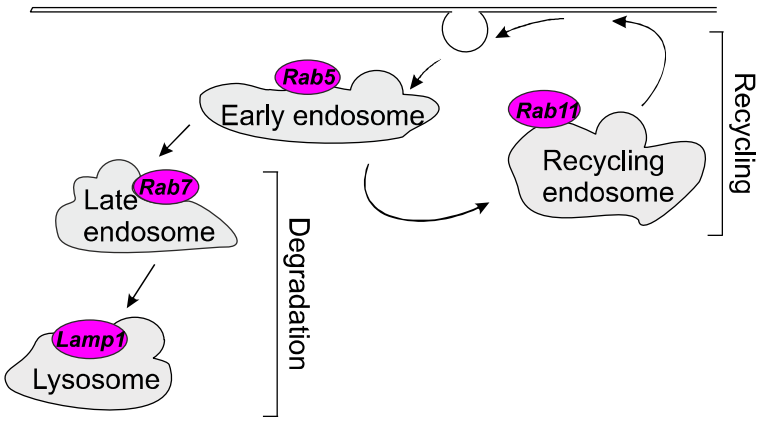

Figure 3.22: Scheme of the endosomal pathway. Marker proteins are marked in magenta: Rab5 for early endosome, and Rab11 for recycling endosome present the recycling pathway, Rab7 for late endosome and Lamp1 for the lysosomes mark the degradation process.

HEK293 cells were cotransfected with three different plasmids each encoding for $Ca_V1.2$-YFP, unlabelled $Ca_V\beta$ and one of the appropriate marker proteins coupled to mRFP and imaged 24 h after transfection. Results are shown in Figure 3.23.

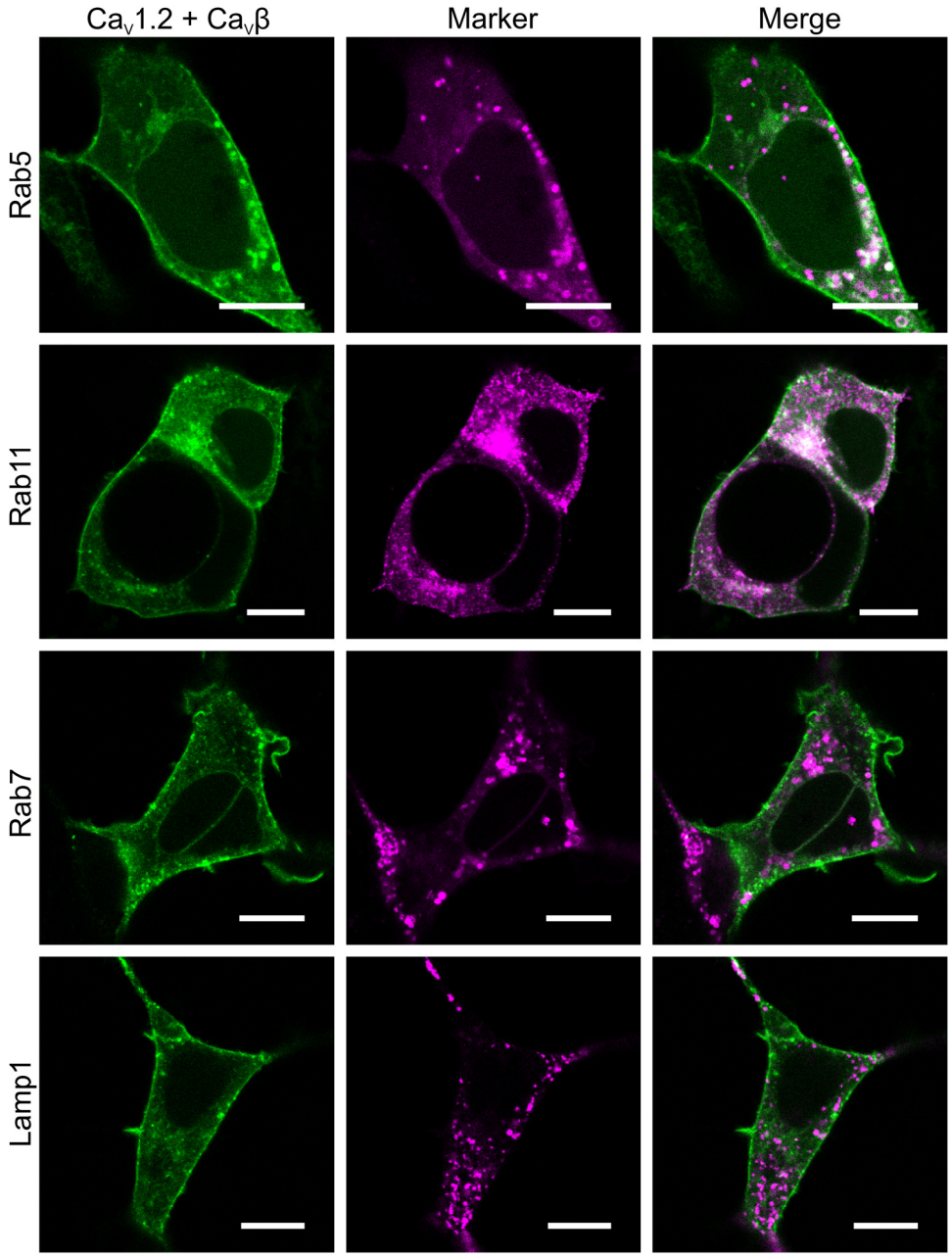

Figure 3.23: Ca$_V$1.2 colocalizes with endosomal marker proteins for early and recycling endosomes. Laser scanning confocal images of HEK293 cells cotransfected with Ca$_V$1.2 fluorescently labelled with mNeonGreen, unlabelled Ca$_V$β (left column, green) and indicated endocytic pathway markes Rab5 (early endosome), Rab7 (late endosome), Rab11 (recycling endosome) and Lamp1 (lysosome) (middle column, magenta). The merge is shown in the right column. Scale bars = 10 µm.

Laser scanning confocal images of transfected HEK293 cells show that Ca$_V$1.2 is located in the plasma membrane of all representative cells confirming the presence of unlabelled Ca$_V$β. All marker proteins present a punctuated pattern throughout the whole cytoplasm. The merge images demonstrate that Ca$_V$1.2 colocalizes with Rab5 and Rab11 but not with Rab7 or Lamp1.

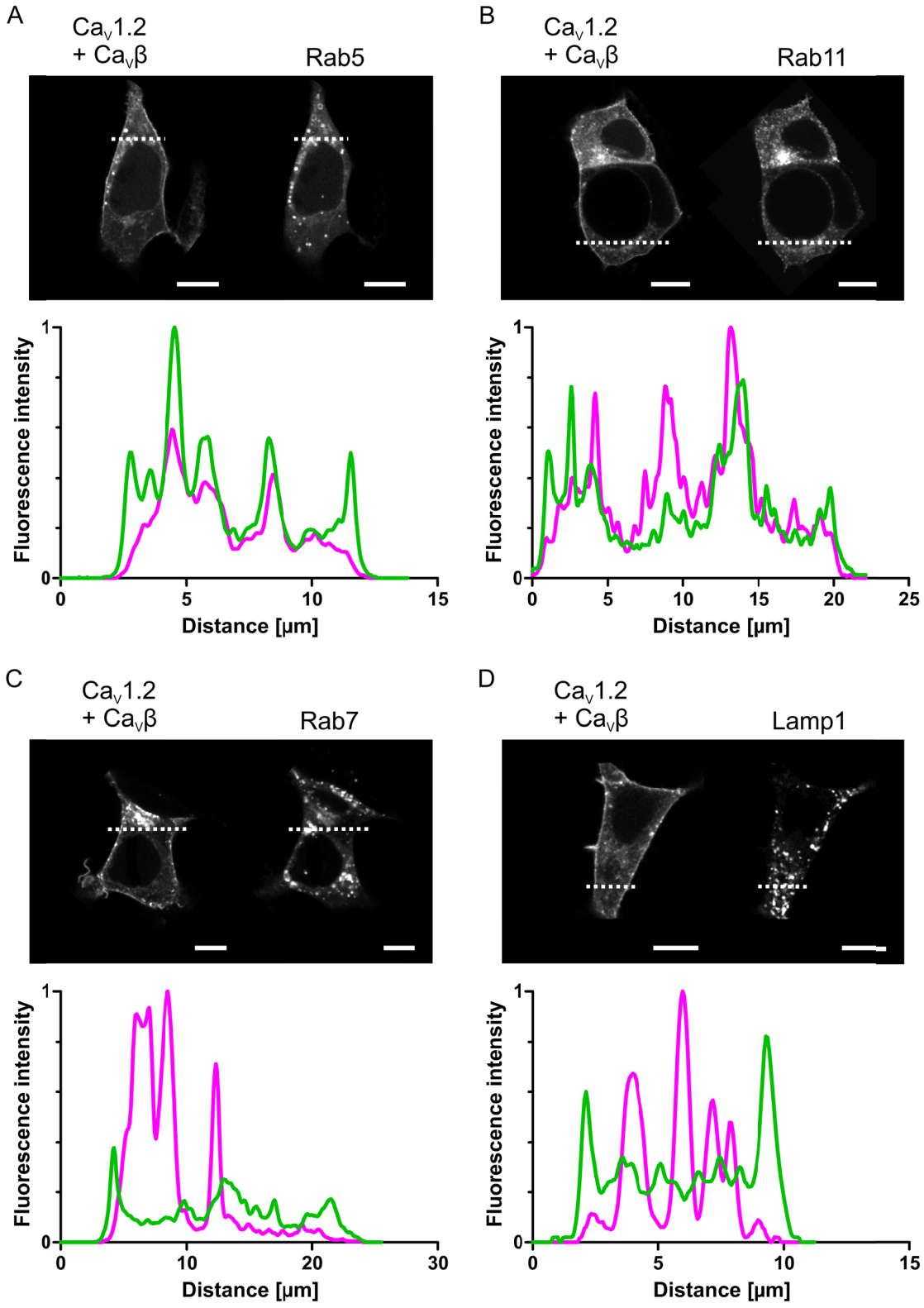

Figure 3.24: The fluorescence intensities of $Ca_V1.2$ and the endosomal markers Rab5 and Rab11 overlap. HEK293 cells transfected with $Ca_V1.2$-mNeonGreen, unlabelled $Ca_V\beta$ and indicated endocytic pathway markes. The dotted line shows the linear region of interest (ROI). The graphs below the images visualize the fluorescence intensities of all images along the ROI. $Ca_V1.2$ is shown in green, the marker in magenta. Overlapping curves show a colocalization. Scale bars = 10 µm.

In agreement with these observations, the fluorescence intensity curves from linear ROIs through the depicted cells for $Ca_V1.2$ together either with Rab5 or with Rab11 show a joint course, whereas the fluorescence intensity curves of $Ca_V1.2$ and Rab7 as well as $Ca_V1.2$ and Lamp1 display different curves progression (Figure 3.24).

For quantitative analysis of the degree of colocalization the mean MOC for the overlap of $Ca_V1.2$ with the endosomal markers in several transfected HEK293 cells were calculated (Figure 3.25).

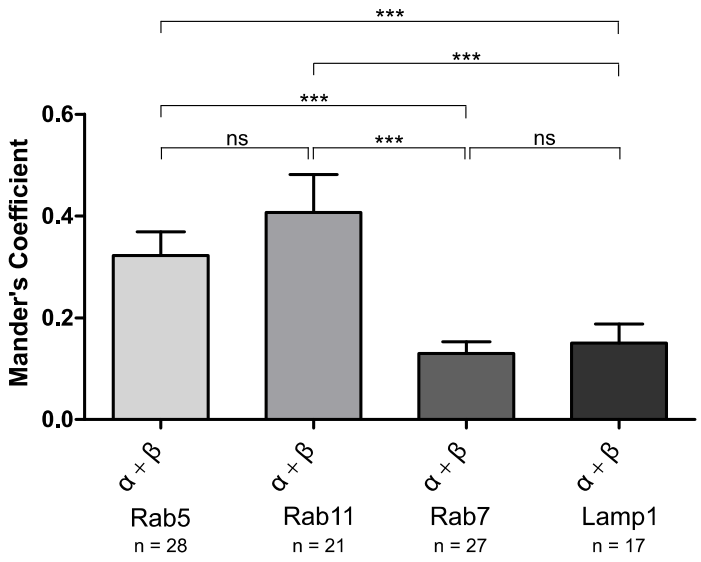

Figure 3.25: $Ca_V1.2$ shows the highest degree of colocalization with endosomal marker proteins Rab5 and Rab11. Fraction of $Ca_V1.2$-fluorescence (in presence of $Ca_V\beta$ ($\alpha + \beta$)) overlapping the respective marker Rab5 (early endosome), Rab7 (late endosome), Rab11 (recycling endosome) and Lamp1 (lysosome) given by the Mander's coefficient. Each bar represents the mean of n analyzed cells (number given below the bars) with the 95% confidence interval. Statistical differences between the fractions were tested with One-Way ANOVA followed by post hoc Bonferroni's Multiple Comparison test ($p \leq 0.001$). Stars represent statistical significances between the two series; ns = no significant.

The highest degree of overlap with $Ca_V1.2$ was found with Rab5 and Rab11. Both mean values vary around 0.4. The values for the overlapping proportions of $Ca_V1.2$ with Rab7 and Lamp1 lie below 0.2. Altogether, these results demonstrate that in our system, regulation of $Ca_V1.2$ cell surface density occurs primarily through recycling and not through lysosomal degradation.

In summary, from our studies on the trafficking pathway of $Ca_V1.2$ heterologously expressed in HEK293 cells, we found that $Ca_V1.2$ requires $Ca_V\beta$ to be released from the ER. Our data support a model by which $Ca_V\beta$ stimulate the mobilization of the channel to the ERES site, and thus allowing the translocation of the channel to the Golgi-network. Translocation to the Golgi does not require an intact microtubule system. After being sorted out from the Golgi-system $Ca_V1.2$ is transported along tubulin filaments towards the plasma membrane in a manner that is independent from the integrity of the actin cytoskeleton. Channels assembled in the plasma membrane are internalized and recycled through to Rab5- and Rab11-mediated pathways. $Ca_V1.2$ along the degradation pathway with either Rab7-positive late endosomes or with lysosomes was not detected, suggesting that degradation directly from the ER must be a main quality control. Therefore, recycling appears to be a key process regulating $Ca_V1.2$ cell surface.

$Ca_V1.2$ is the most prominent voltage-activated calcium channel expressed in cardiac tissue and regulation of its surface expression is essential for normal cardiac function. The density of calcium channels is tightly regulated and abnormalities resulting in alterations of the channel surface density have been related to several cardiac disorders. Previous results reported from our group (Stolting et al. 2015) support the idea that a direct interaction between F-actin and $Ca_V\beta$ promotes surface expression of the channel in HL-1 cardiomyocytes. In the following the endocytic-recycling pathway machinery of $Ca_V1.2$ channels in the murine cardiac muscle cell line HL-1 and the role of the microtubule-based network were investigated. The results show that the pathway defined in heterologous expression system holds true for endogenous expressed $Ca_V1.2$ in HL-1 cells.

3.5 Recycling of endogenously expressed $Ca_V1.2$ in HL-1 cardiomyocytes

To further investigate a potential recycling pathway, implied by the results from heterologous system, HL-1 cells were immunochemically stained with several antibodies for endosomal marker proteins.

During the first step of clathrin-mediated endocytosis vesicles are coated with clathrin proteins and then fused to endosomes for further sorting (Grant and Donaldson 2009). After budding of vesicles from the membrane they are sorted to early endosomes from where they can be diverted to recycling or late endosomes (Figure 3.22). Clathrin function is also crucial in protein secretion from the trans-Golgi network (McMahon and Boucrot 2011). Here, I performed double immunostaining in HL-1 cells for $Ca_V1.2$ and one of the different

endosomal compartments, including clathrin coated vesicles, early, recycling and late endosomes. Unfortunately no lysosomal antibody tested up-to-date showed specifity in HL-1 cells.

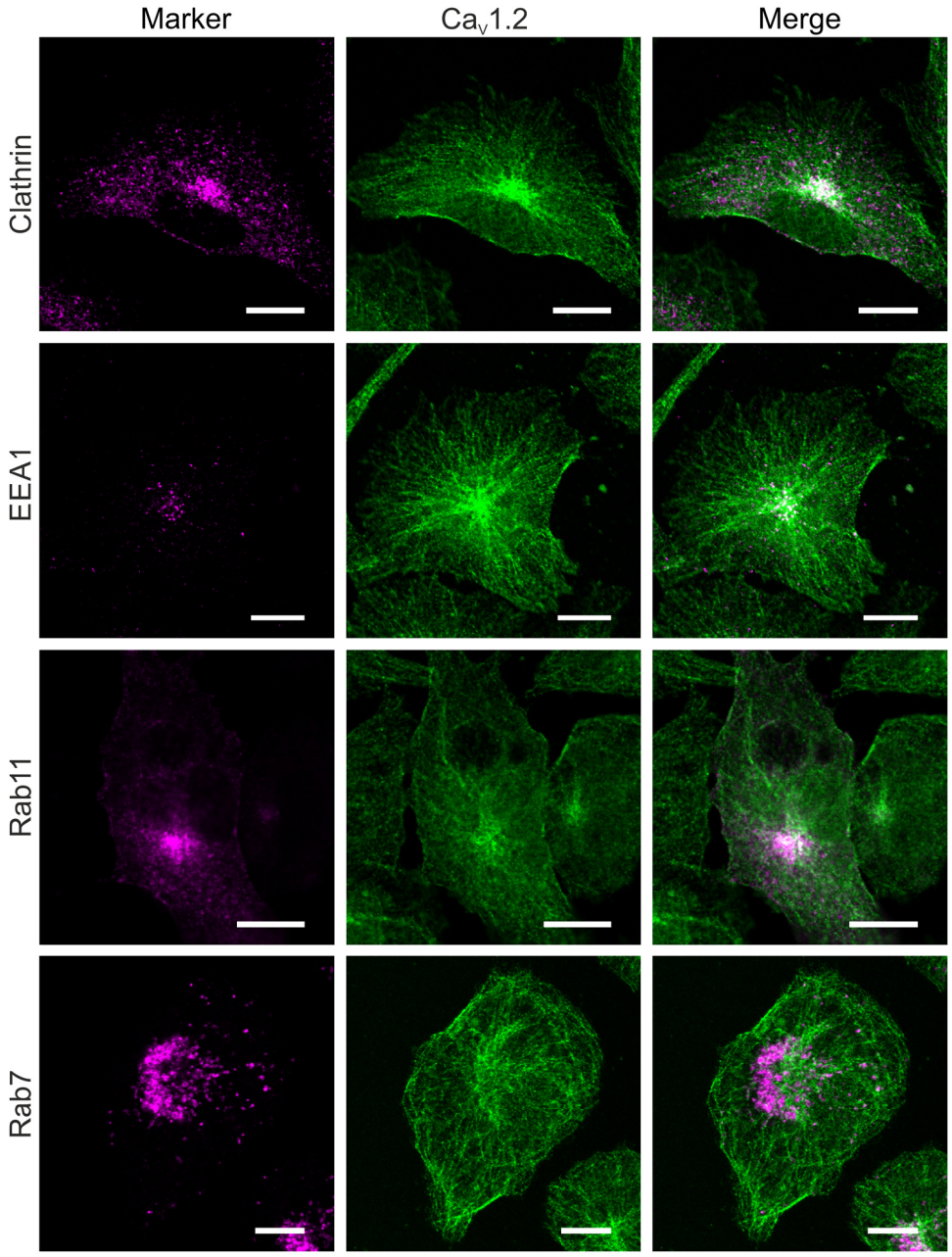

Figure 3.26: Endogenous $Ca_V1.2$ colocalizes with with clathrin, EEA1 and Rab11 but not with Rab7. Laser scanning confocal images of HL-1 immunochemically stained for $Ca_V1.2$ (middle column, green) and indicated marker Clathrin, EEA1 (early endosome antigen1), Rab11 (recycling endosome) and Rab7 (late endosome). The right image shows the merge of $Ca_V1.2$ with the respective marker. Scale bar = 10 µm.

Laser scanning confocal images of HL-1 cells fluorescently labelled for $Ca_V1.2$ (green) and indicated marker proteins (magenta) show an apparent strong colocalization of $Ca_V1.2$ channel with clathrin and Rab11 positive endosomes, a weaker colocalization with EEA1 and no overlap with Rab7 positive endosomes (Figure 3.26).

Especially for the Rab11-staining we had difficulties to find an appropriate antibody for HL-1 cells staining. So we performed control stainings to verify the antibody specificity by transfecting HL-1 cells with Rab11-mRFP-encoding plasmid and treating cells with the Rab11A antibodies (Figure 3.27). The complete overlap with the heterologous expressed Rab11mRFP in the control-staining in HL-1 cells shows the specificity of the D3 antibody (Figure 3.27, lower panel). Another commercially available antibody for Rab11 (A6) gave no colocalization with Rab11-mRFP (Figure 3.27, upper panel). These results validate the use of this antibody and show undoubtedly that Rab11 positive endosomes colocalize with $Ca_V1.2$ in HL-1 cells.

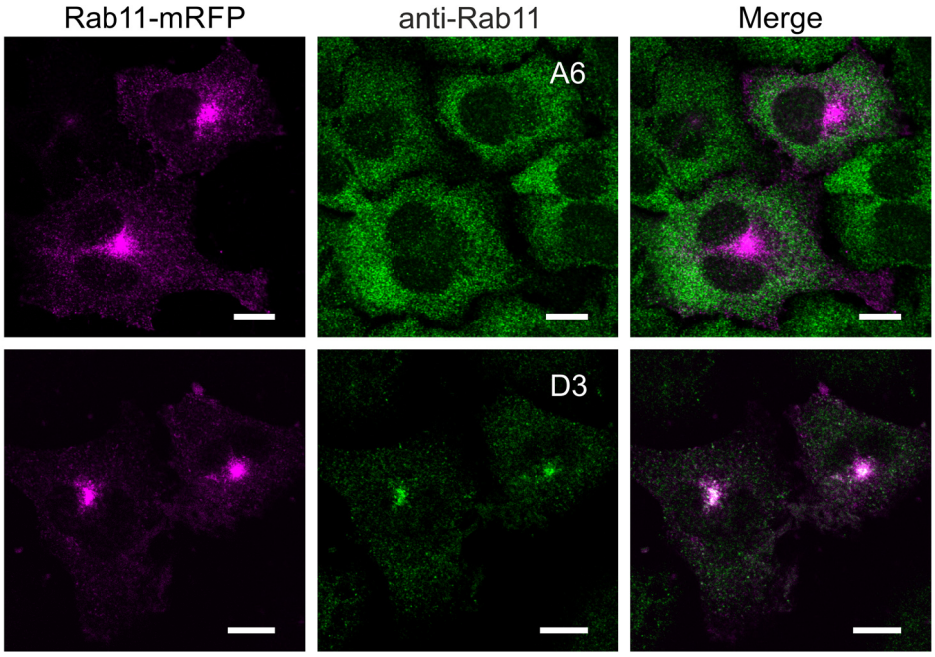

Figure 3.27: Specifity of antibodies for Rab11A. Laser scanning confocal images of HL-1 cells transfected with Rab11-mRFP (left column, magenta) and immunochemically stained for two different antibodies for Rab11A (middle column, green). The right image shows the merge. Scale bar = 10 µm.

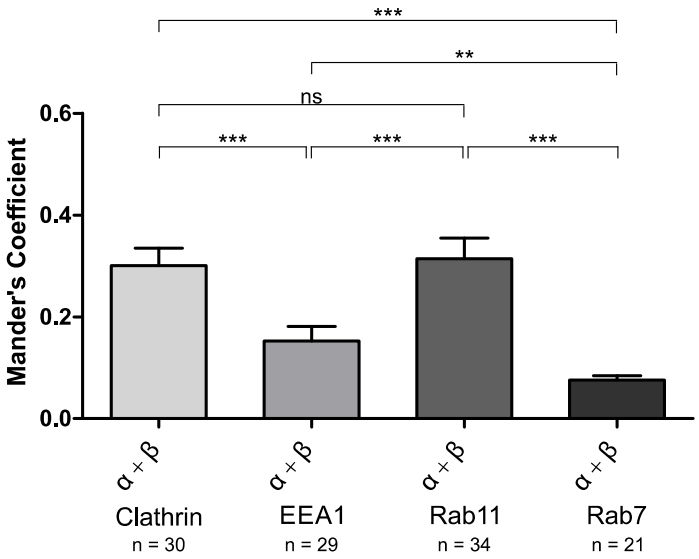

Figure 3.28: Endogenous $Ca_V1.2$ colocalizes in the highest degree with clathrin and Rab11. Fraction of immunochemically stained endogenous $Ca_V1.2$ in HL1-cells overlapping respective marker Clathrin, EEA1 (early endosome antigen1), Rab11 (recycling endosome) and Rab7 (late endosome) given by the Mander's coefficient. Each bar represents the mean of n analyzed cells (number given below the bars) with the 95% confidence interval. Statistical differences between the fractions were tested with One-Way ANOVA followed by post hoc Bonferroni's Multiple Comparison test ($p \leq 0.001$). Stars represent statistical significances between the two series; ns = no significant.

As visually observed the strongest degree of colocalization, as assessed by MOC values, appears between $Ca_V1.2$ and clathrin and $Ca_V1.2$ and Rab11 positive endosomes (Figure 3.28). These values are twice as high as the overlapping proportion with EEA1 and even three times higher as the overlap coefficient for Rab7. The MOC for EEA1 is around 0.2. Concerning to the colocalization benchmark source such low coefficients may due to a random overlap of fluorophores in the same pixel. However this is not necessary valid in cases where the number of the two fluorophores detected greatly differs between each other (Zinchuk and Grossenbacher-Zinchuk 2014). In the case for EEA1 very fewer spots are observed in a tiny region of the cell, while the signal of $Ca_V1.2$ is spread all over the cell.

Despite of these, the above results show that at least part of $Ca_V1.2$ is internalized by clathrin-mediated endocytosis in HL-1 cells, recycled by Rab11 pathways and sorting to late endosomes, and thus we assume to the lysosomal degradation pathway barely take place.

3.6 Role of the cytoskeleton in HL-1 cells

To visualize the transport of $Ca_V1.2$ along cytoskeletal tracks the architecture of actin and tubulin-based cytoskeleton with respect to $Ca_V1.2$ channels were imaged in fluorescently stained HL-1 cells for actin, tubulin and $Ca_V1.2$. While the corresponding antibodies for tubulin and $Ca_V1.2$ were used, to label actin the high affinity Phalloidin toxin was utilized instead of an antibody (cf. 2.5).

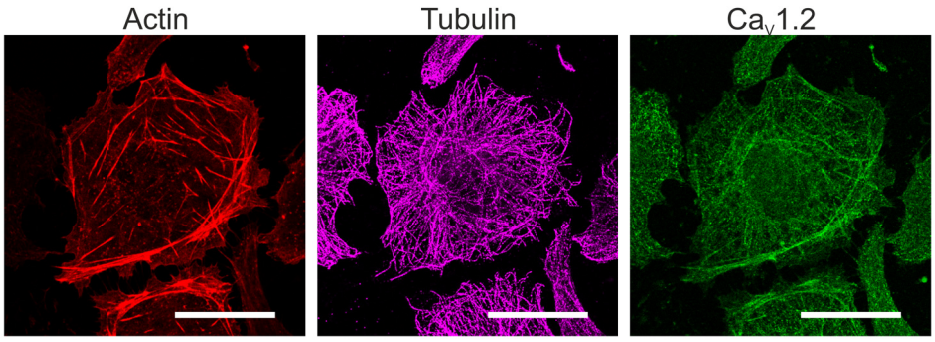

Figure 3.29: Endogenous $Ca_V1.2$ colocalizes with microtubules and actin filaments. Laser scanning confocal images of HL-1 cells immunochemically stained for actin (red), tubulin (magenta) and $Ca_V1.2$ (green). Scale bar = 25 µm.

Confocal images in Figure 3.29 show that the actin filaments concentrate in a narrow area beneath the cell membrane, whereas microtubules demonstrate a radial distribution originating from a perinuclear MTOC (microtubule-organization center) towards the cell periphery. Membrane staining of endogenous $Ca_V1.2$ channels could not be clearly detected by immunostaining but electrophysiological experiments performed in our group confirm the presence of functional $Ca_V1.2$ channels in the plasma membrane (Stolting et al. 2015). $Ca_V1.2$ builds filament-like structures forming a network that closely resembles the spatial distribution of microtubules - as well as of F-actin. This observation is further corroborated by single molecule localization experiments done in our institute on same batch of HL-1 cells immunostained with the same antibodies used for laser confocal images. Super resolution images (kindly provided by Johnny Hendriks) demonstrate that $Ca_V1.2$ indeed distributes along tubulin filaments over relatively long distances (Figure 3.30).

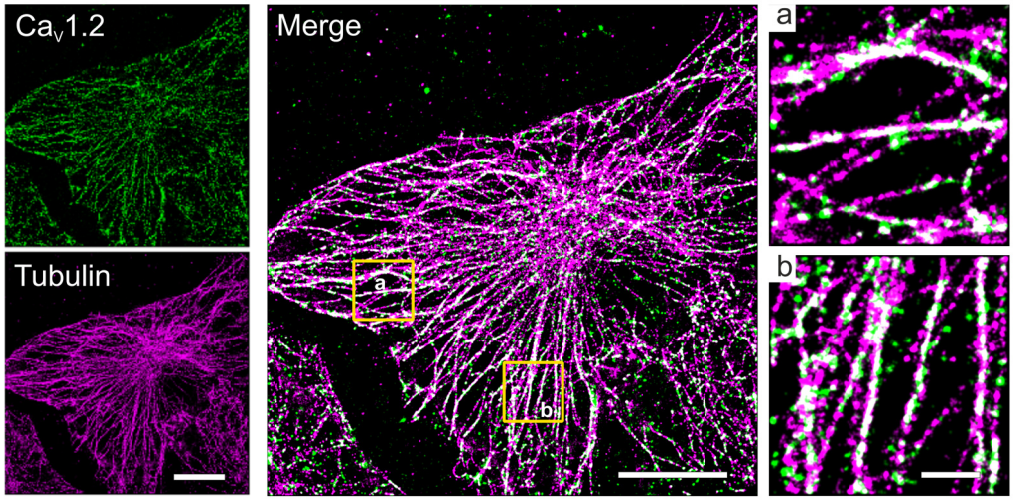

Figure 3.30: Ca$_V$1.2 distributes along microtubules from the perinuclear region to the cell periphery. Single molecule localization microscopy images from a representative HL-1 cell immunostained for tubulin (magenta) and Ca$_V$1.2 (green). The corresponding merge image is shown in the middle panel with enlarged views of the regions marked with squares (right panels). Scale bars = 10µm and 1µm for magnifications (right panel). Pictures kindly provided by Johnny Hendriks.

To determine the extent to which the microtubule-dependent transport of Ca$_V$1.2 plays a role in the channel's trafficking pathway, HL-1 cells were treated with the microtubules disruptor nocodazole. The effectiveness of the nocodazole treatment at different time durations was evaluated by double immunofluorescence labelling of tubulin and Ca$_V$1.2. Results are shown in Figure 3.31.

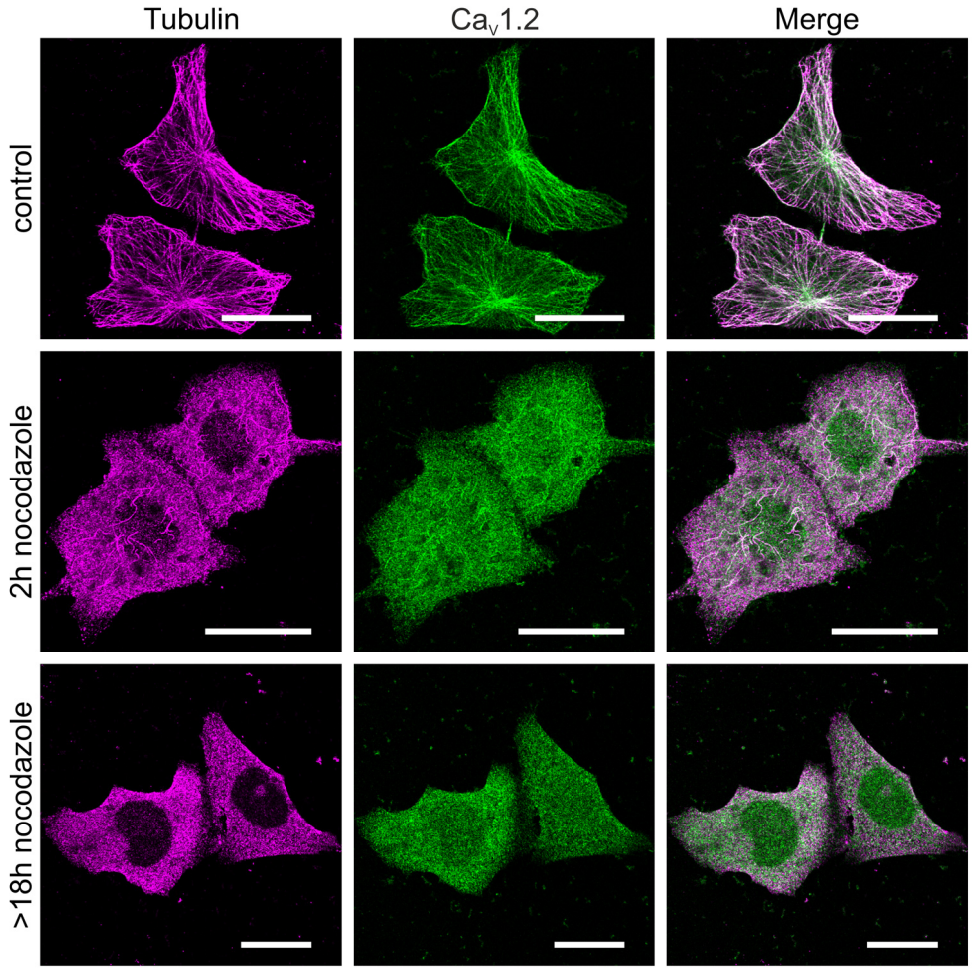

Figure 3.31: Endogenous $Ca_V1.2$ loses filament-like structures after tubulin disruption. Laser scanning confocal images of HL-1 cells untreated (upper row) or pharmacology treated with 33 µM nocodazole for 2 h or > 18 h. All cells are immunochemically stained for tubulin (magenta) and $Ca_V1.2$ (green). The right image shows the merge of $Ca_V1.2$ and tubulin. Scale bar = 25 µm.

Fluorescently labelled microtubules and $Ca_V1.2$ present a joint filament structure (Figure 3.31). After two hours exposition to nocodazole the majority of microtubules was destroyed and the $Ca_V1.2$ filament-like structures vanished. In the long-term treatment (> 18 h) almost no filament assembly was visible.

Effectively disruption of F-actin by treatment with 10 µM cytochalasin D for 6 h does not inhibit the extensive association of channels with the microtubule network. In the presence of cytochalasin D the filament-like structures formed by $Ca_V1.2$ and tubulin are preserved suggesting that the early secretory path and transport along microtubules does not rely on intact F-actin (Figure 3.32).

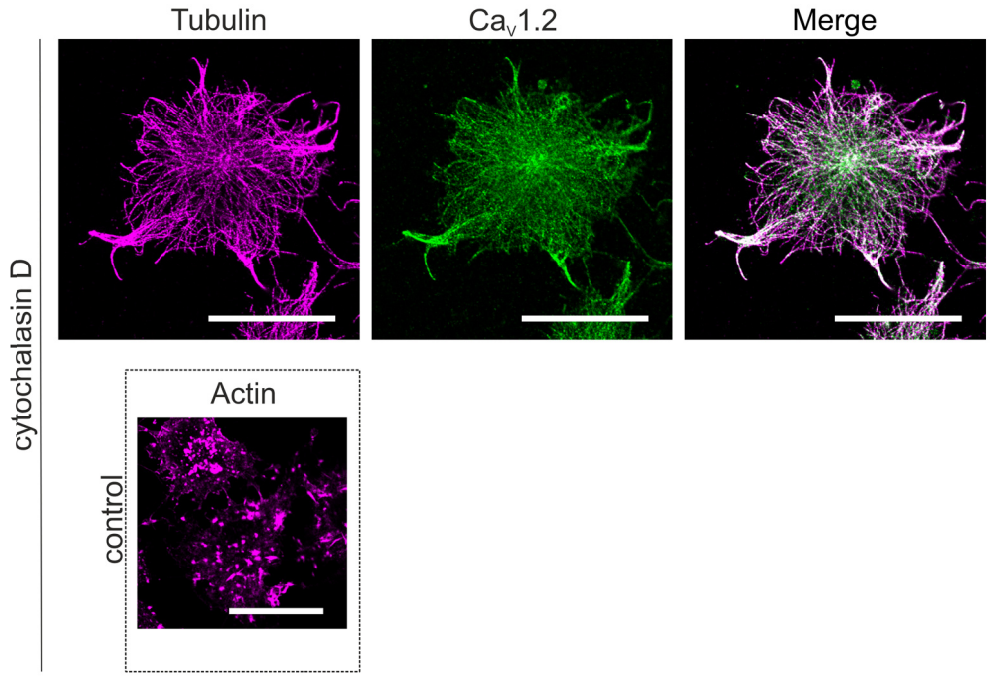

Figure 3.32: Endogenous $Ca_V1.2$ distribution along microtubules is preserved after F-actin disruption. Laser scanning confocal images of HL-1 cells treated for 6 h with 10 µM cytochalasin D and immunochemically stained for tubulin (magenta) and $Ca_V1.2$ (green). The right image shows the merge of $Ca_V1.2$ and tubulin. The upper image shows the control of disrupted actin filaments. Scale bar = 25 µm.

This suggestion is supported by the degree of colocalization, determined by the Mander's overlap coefficient. Overlapping proportions of $Ca_V1.2$ with tubulin in untreated and in pharmacologically treated cells are not altered by treatment of cells with cytochalasin D. Though F-actin appears not required for the secretory transport along microtubules, it does play a role in regulating the number of $Ca_V1.2$ channels in the plasma membrane (Stolting et al. 2015). In contrast to heterologous expressed $Ca_V1.2$ channels, we do observe colocalization between $Ca_V1.2$ and F-actin (cf. Figure 3.29). We have already hypothesized that F-actin mediated recycling of $Ca_V1.2$ is an important step in regulating their surface density in HL-1 cells. Here, I show that indeed recycling of $Ca_V1.2$ is occurring in HL-1 cells.

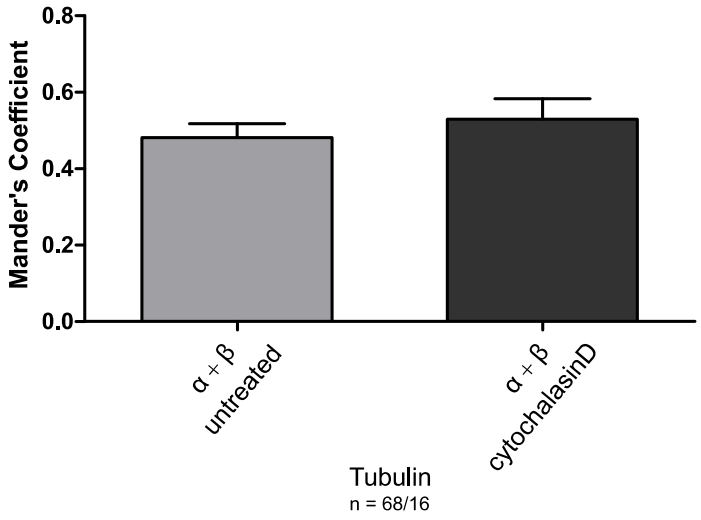

Figure 3.33: Colocalization of endogenous $Ca_V1.2$ with tubulin after actin disruption does not change. Fractions of immunochemically stained endogenous $Ca_V1.2$ in HL1-cells overlapping tubulin in untreated cells or pharmacologically treated cells with 10 µM cytochalasin D given by the Mander's coefficient. Each bar represents the mean of n analyzed cells (number given below the bars) with the 95% confidence interval. No statistical differences between the fractions (One-Way ANOVA followed by post hoc Bonferroni's Multiple Comparison test ($p \leq 0.001$)) could be determined.

3.7 Quantification of trajectories dynamics

3.7.1 Particle detection and tracking

In the previous section, I investigated the transport pathway of $Ca_V1.2$ to and from the plasma membrane. In the following section, my studies aimed to gain insights over the dynamics of the $Ca_V1.2$ intracellular transport.

To characterize the movement of $Ca_V1.2$ channel complexes, living cells were imaged with spinning disk confocal laser scanning microscopy 24 h after transfection with fluorescently labelled $Ca_V1.2$ and Cavβ subunits.
As demonstrated in the above result (cf. 3.1), $Ca_V\beta$ allows the export of the channel from the ER and the vesicular movement of the channel toward the plasma membrane. However, if both subunits are cotransported all the way to the plasma membrane or if they dissociate along the $Ca_V1.2$ transport itinerary remains elusive.

Here, two $Ca_V\beta$ isoforms were used, $Ca_V\beta2a$ and $Ca_V\beta2b$ that differ in their cellular distribution. While $Ca_V\beta2b$ is cytosolic and only membrane targeted in association with $Ca_V1.2$, $Ca_V\beta2a$ undergoes palmitoylation and is targeted to the plasma membrane independent of the α_1-subunit (Chien et al. 1998, Miranda-Laferte et al. 2014). On the basis of their distinct subcellular localization and ability to interact with lipids, we rationalize that these $Ca_V\beta2$ isoforms might have a different impact on the $Ca_V1.2$ transport dynamics.
In the absecence of any $Ca_V\beta$ (2a or 2b) $Ca_V1.2$ does not display directed motion that is in agreement with $Ca_V\beta$ being required for exiting the ER and further translocation to the Golgi network (Figure 3.34A).When expressed alone, neither, $Ca_V\beta2a$ nor $Ca_V\beta2b$ resulted in vesicle movement that could be tracked (Figure 3.34B and C). In contrast, in cells coexpressing $Ca_V1.2$ and $Ca_V\beta$ moving particles emerge that can be observed with both emission channels, and are amenable for single particle tracking analysis (Figure 3.34D and E).

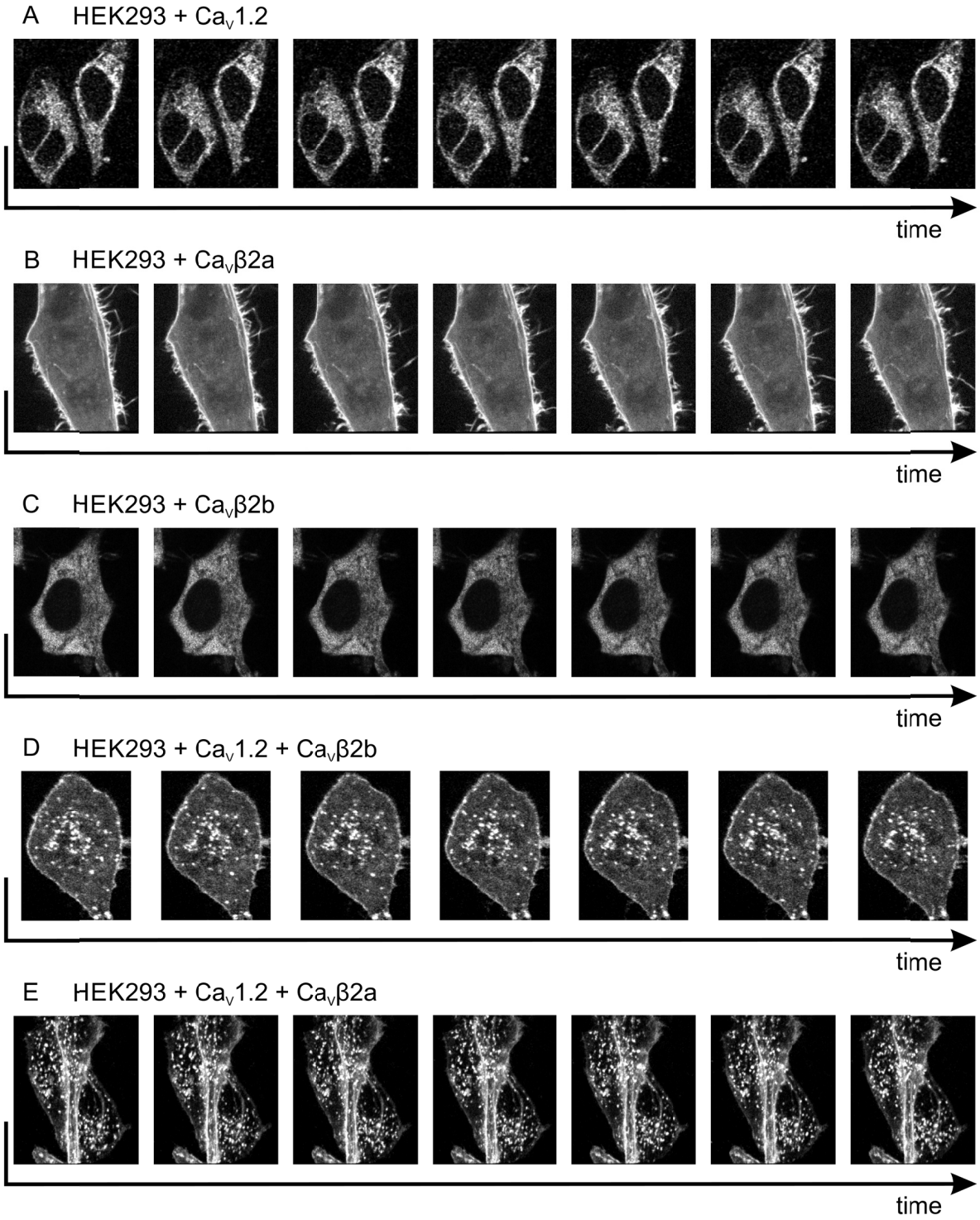

Figure 3.34: Trackable particle movement in HEK293 cells can only be detected after coexpression of $Ca_V1.2$ and $Ca_V\beta$. Laser scanning spinning disk confocal images of HEK293 cells expressing A) $Ca_V1.2$-EGFP (Δt = 2.4 s), B) $Ca_V\beta2a$-mRFP (Δt = 4 s), C) $Ca_V\beta2b$-mRFP (Δt = 2.6 s), D) $Ca_V\beta2b$-mRFP and $Ca_V1.2$-mNeonGreen (Δt = 3.6 s) or E) $Ca_V\beta2a$-mRFP and $Ca_V1.2$-mNeonGreen (Δt = 4 s), all 24 h after transfection.

Figure 3.35 shows the same film sequence that is presented in Figure 3.34E with $Ca_V1.2$ colored in green and $Ca_V\beta$ in red. Simple eye-tracking inspection of the moving vesicles agrees with the notion that most of the $Ca_V1.2$ moving particles are connected to a $Ca_V\beta$ particle (Figure 3.35, ROI a). In contrast regions where no movement of the channel is detected no $Ca_V\beta$ is found in the channels' sourrounding (Figure 3.35, ROI b). The magnification of the regions of interest within the film sequence of HEK293 cells coexpressing both subunits show that the "green and red" fluorophores move together throughout the cell suggesting that $Ca_V1.2$ is associated with $Ca_V\beta$ during the channel´s intracellular transport.

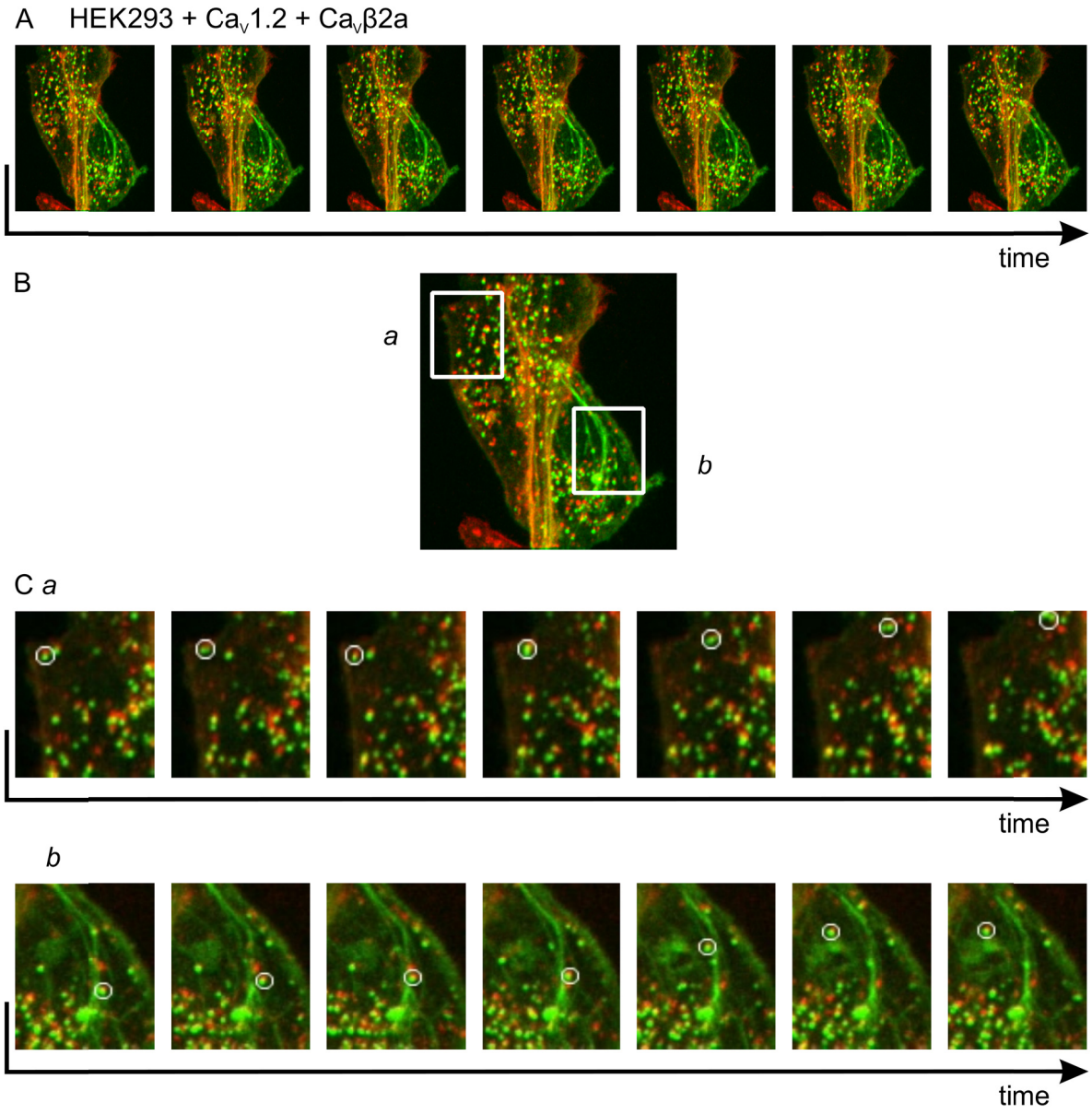

Figure 3.35: Fluorescently labelled Ca$_V$1.2 seem to be associated with fluorescent Ca$_V$β2a and to move together. Laser scanning spinning disk confocal images of HEK293 cells expressing Ca$_V$β2a-mRFP (red) and Ca$_V$1.2-mNeonGreen (green) (Δt = 4 s); A) shows an overview of the recorded cells, B) gives the taken regions of interest for the magnification in C) where one particle per sequence is marked for better visualization of its movement during time.

In order to dissect retrograde from secretory transport, Flp-In T-REx cells were transfected with Ca$_V$1.2 to allow synchronization of channel expression. The Ca$_V$1.2 expressed in Flp-In T-REx cells was either fluorescently labelled or covalently linked to a HaloTag. Coupling the channel to the very bright mNeonGreen fluorescent protein allowed longer exposition time minimizing bleaching (Shaner et al. 2013). Labelling the channel with

HaloTag ligands permitted the dissection of $Ca_V1.2$ channels engaged in the biosynthetic secretory pathway from the ones removed from the plasma membrane. Channels bearing the HaloTag that are already assembled into the plasma membrane can be selectively labelled by exposing to a cell impermeable HaloTag ligand resulting in the specific labelling of channels at the cell surface. In such a way, the fluorescently labelled channels correspond exclusively to the pool of channels that was internalized within endosomes.

Figure 3.36 shows a $Ca_V\beta2a$-mcherry inducible Flp-In T-REx ('Flp-In') cell expressing $Ca_V1.2$-HaloTag and stained with the cell impermeable HaloTag Ligand AlexaFluor488. $Ca_V1.2$ fluorescently labelled channels distributes along the plasma membrane and some of them are found intracellularly indicating that internalization has occurred. Most of the endosomes containing the channel do not colocalize with $Ca_V\beta2a$ that can also be observed in the plasma membrane and intracellularly. Given that $Ca_V1.2$-HaloTag preserves its binding capability to $Ca_V\beta$, this result suggests that channel internalization is independent of $Ca_V\beta$ association (Figure 3.36).

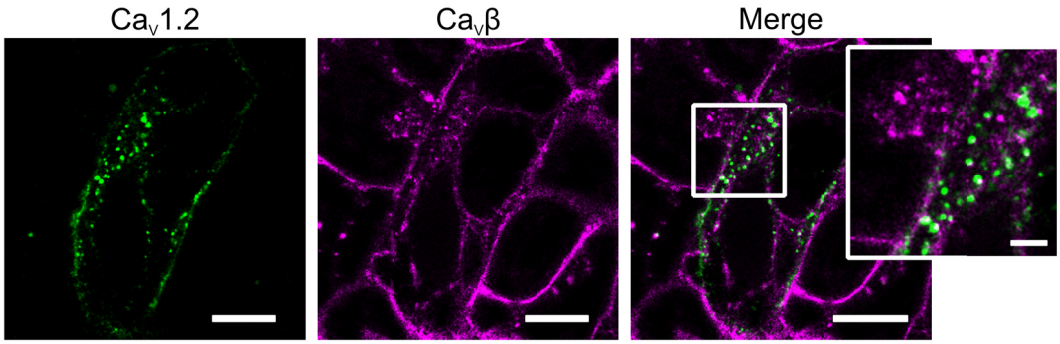

Figure 3.36: $Ca_V1.2$-HaloTag in induced Flp In-T-REx-$Ca_V\beta2a$-mcherry cells is internalized. Laser scanning confocal images of Flp-In T-REx-$Ca_V\beta2a$-mcherry cells transfected with $Ca_V1.2$-HaloTag stained with the impermeable HaloTag Ligand AlexaFluor488 (green, left image). $Ca_V\beta2a$-mcherry expression was induced with tetracycline for 20 h, shown in the middle image (magenta). The right image shows the merge. Scale bar = 10 µm.

A pulse chase experiment consists of a consecutive staining of the cells first with the permeable fluorescent HaloTag ligands followed by the impermeable one. Flp-In cells expressing the $Ca_V1.2$-Halo tagged channel and $Ca_V\beta2a$-mcherry subjected to the chase pulse labelling strategy demonstrates that the internalized channels i.e. the labelled channels with the impermeable ligand, are distinguished clearly from the pool of intracellular channels that have not been yet inserted into the plasma membrane and thus were available for being

stained with the cell permeable dye during the pulse chase (Figure 3.37A). Moreover, control stainings in untransfected cells with the same ligands result in no fluorescence signal (Figure 3.37B).

These observations prove the specificity of the ligands to the $Ca_V1.2$-HaloTag channel and validate the use of this labelling strategy to follow the destiny of internalized channels.

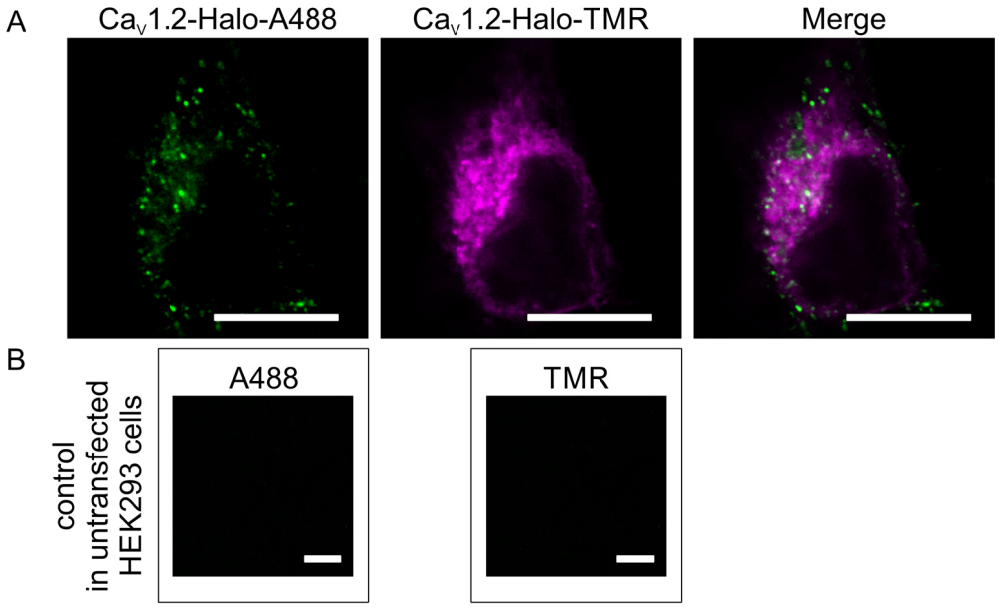

Figure 3.37: Two pools of channels within forward and retrograde trafficking. Laser scanning confocal images of A) HEK293 expressing $Ca_V1.2$-HaloTag and unlabelled $Ca_V\beta$ were stained sequentially with impermeable HaloTag-ligand AlexaFluor488 ($Ca_V1.2$-Halo-488, green) and permeable HaloTag-ligand TMR ($Ca_V1.2$-Halo-TMR, magenta). The right column shows the merge. Scale bar = 10 µm. B) Control with untransfected HEK293 cells stained with either the impermeable HaloTag Ligand AlexaFluor488 (right picture) or the permeable HaloTag Ligand TMR (left picture). Scale bar = 50 µm.

In order to compare transport dynamics of $Ca_V1.2$ channels within the secretory and endocytic pathway and to assess the effect of the two $Ca_V\beta2$ isoforms four different groups of cells, transfected with different subunit combinations, were analyzed and described in Table 3.1 with the corresponding abbreviation used hereinafter:

Table 3.1: Transfection schemes and cells used for single particle tracking analysis.

Group	Description	Abbreviation
1)	HEK293 cells cotransfected with Ca_Vβ2a-mRFP and Ca_V1.2-mNeonGreen	HEK-Ca_V1.2-Ca_Vβ2a
2)	HEK293 cells cotransfected with Ca_Vβ2b-mRFP and Ca_V1.2-mNeonGreen	HEK-Ca_V1.2-Ca_Vβ2b
3)	Flp-In T-REx-Ca_Vβ2a-mcherry (induced), transfected with Ca_V1.2-mNeonGreen	Flp-In-Ca_V1.2
4)	Flp-In T-REx-Ca_Vβ2a-mcherry (induced), transfected with Ca_V1.2-Halo + AlexaFluor488-Ligand	Flp-In-Ca_V1.2-Halo

The first two groups include HEK293 cells cotransfected with Ca_V1.2-mNeonGreen and Ca_Vβ2a-mRFP (group 1) or Ca_V1.2-mNeonGreen and Ca_Vβ2b-mRFP (group 2). In the third and fourth group Ca_Vβ2a-mcherry induced Flp-In T-REx cells either transfected with Ca_V1.2-mNeonGreen (group 3) or with Ca_V1.2-HaloTag and stained with the impermeable HaloTag Ligand AlexaFluor488 (group 4) were used.

To investigate the dynamics of the channel's transport, single trajectories were reconstituted from single particle tracking analysis on each different time frame (Figure 3.38A). Particles were detected by finding local intensity maxima and subsequently connected by using an algorithm for an autoregressive motion model. From the evaluation of the resulting trajectories the type of motion and diffusion coefficient for moving particles can be evaluated. The trajectories obtained for a representative cell is shown in Figure 3.38B-D. Using the software Imaris, the pool of reconstructed trajectories can be color coded according to different motion parameters, including speed and the direction of the displacement for each trajectory is visualized by arrows (Figure 3.38C-D).

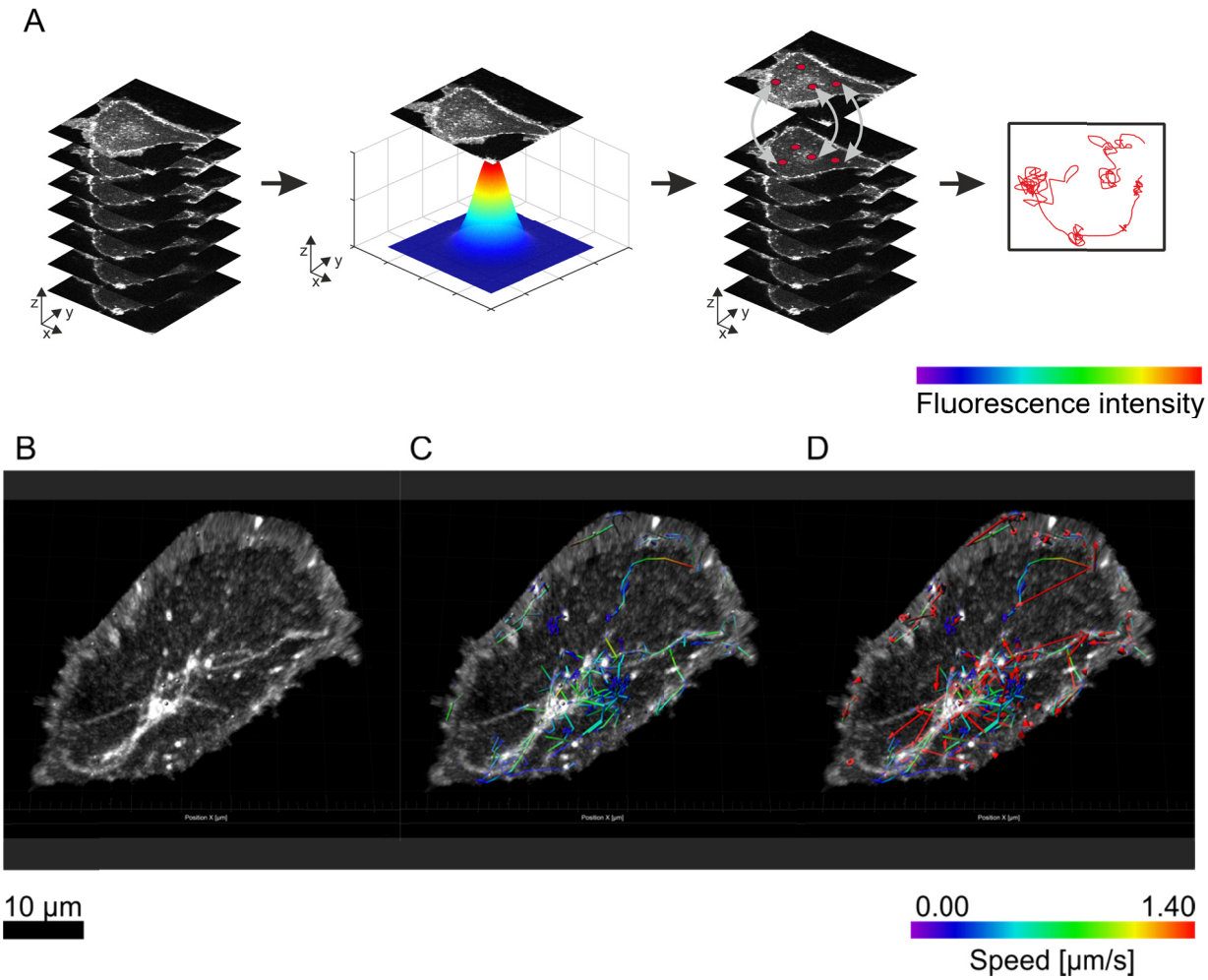

Figure 3.38: Principle of the single particle tracking and the trajectory-analysis in Imaris. A) Methodology of single particle tracking: Within the projection of frames all intensity peaks of fluorescent particles are detected, fitted with Gaussian and traced with nearest neighbor algorithm to particles in the next time frame. This connections result in trajectories. B)-D) Screenshots from an exemplary HEK293 cell expressing fluorescence labeled $Ca_V1.2$ and $Ca_V\beta2a$ (not shown) within the analysis by using the software Imaris. B) Particles are detected within the z-stack and C) connected to trajectories by using a special algorithm. D) Red arrows show the direction of displacement. In this case, all trajectories are color coded by their speed.

Since all cells showed different signal to noise ratios, each individual cell was further eye-inspected after particle detection and building of trajectories to evaluate false connections between particles.

The trajectories were determined in x-, y-, and z-direction and the complete set obtained for one representative cell transfected with $Ca_V1.2$-mNeonGreen and $Ca_V\beta2a$-mRFP (group 1) is plotted in a three-dimensional space (Figure 3.39A and B). To facilitate visualization, the

trajectories are also plotted in a two dimensional graph (Figure 3.39C). Only the trajectories detected for $Ca_V1.2$-mNeonGreen are shown.

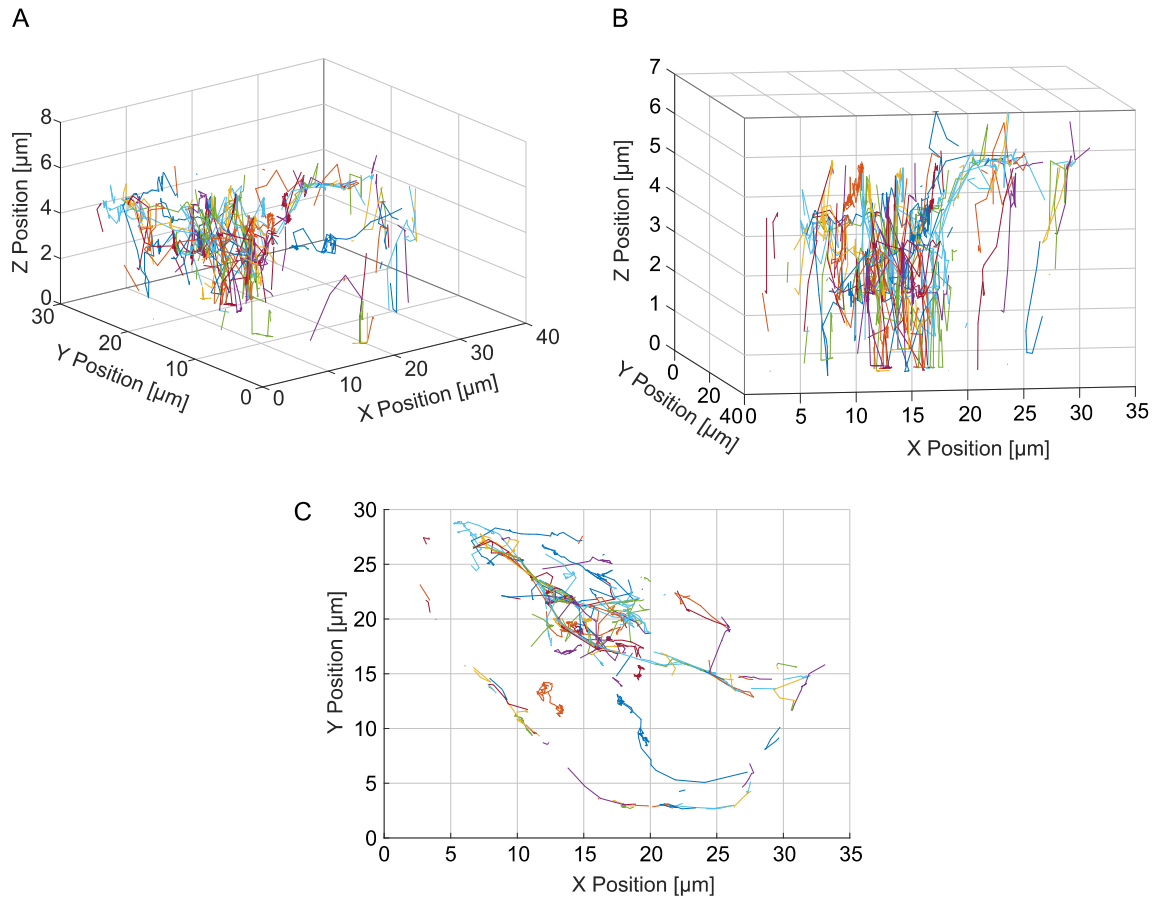

Figure 3.39: Trajectories of fluorescently labelled $Ca_V1.2$ coexpressed with $Ca_V\beta$. Sum of all trajectories of $Ca_V1.2$ found in one representative HEK293 cell plotted in A) three-dimensional space diagonally from above and B) from the front. C) shows the top view in two dimensions.

The graphs show that the trajectories for $Ca_V1.2$ vary considerable in length and space. In the three-dimensional plots, the trajectories are distributed throughout along the Z-axis, extending from the bottom surface of the cell (z position = 0 µm) to the top (Figure 3.39A-B). Looking at the three-dimensional plot from the front view (Figure 3.39B) one observe that only a small part of the trajectories touches the upper (top) edge of the cell. In the two-dimensional plot, the trajectories resemble the morphology of the cell in term that the area where no trajectory was obtained corresponds to the nuclei and the margins to the plasma membrane. From this plot it appears that a number of trajectories take place along the cell border near the plasma membrane and other around the perinuclear region (Figure 3.39C).

Figure 3.40 show the trajectories obtained from a representative cell expressing the Halo tagged $Ca_V1.2$ (group 4), i.e. tracks from internalized channels.

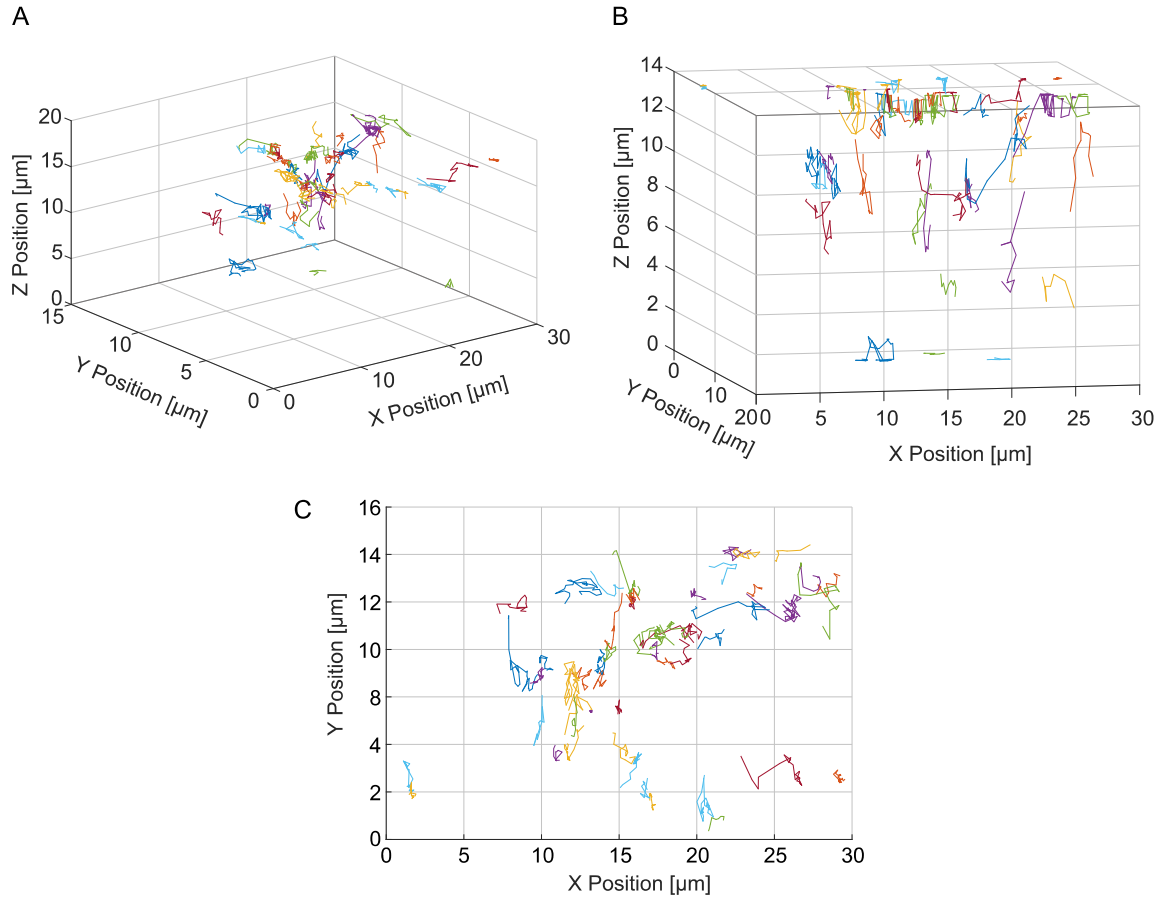

Figure 3.40: Trajectories of $Ca_V1.2$-HaloTag in induced Flp-In T-REx cells labelled with impermeable ligand. Sum of all trajectories of $Ca_V1.2$-HaloTag found in one representative Flp-In cell plotted in A) three-dimensional space diagonally from above and B) from the front. C) shows the top view in two dimensions.

In comparison with group 1, fewer trajectories were obtained that would be expected when tracking only endocytosed channels. In the front view within the three-dimensional plot it can be observed that the main proportion of the trajectories is localized at the upper top edge of the cell (z position = 14 µm, Figure 3.40B). This is consistent with the excepted location of channels moving from the plasma membrane as a result of internalization and highlights the use of this strategy to follow internalized $Ca_V1.2$.

A central parameter during the tracking analysis is the maximal distance the algorithm is allowed to search for connecting particles in consecutive frames as depicted in Figure 3.41. Due to the fact that the search radius constrains the maximal speed that can be calculated for

any given particle, a compromise had to be found between reliable connections and therefore identifiable trajectories and the speed limit. With increasing search radius the distance covered by the particle could be longer and therefore the maximal speed increases. However, because more matching candidates are found within the search radius, the probability for false connections augments.

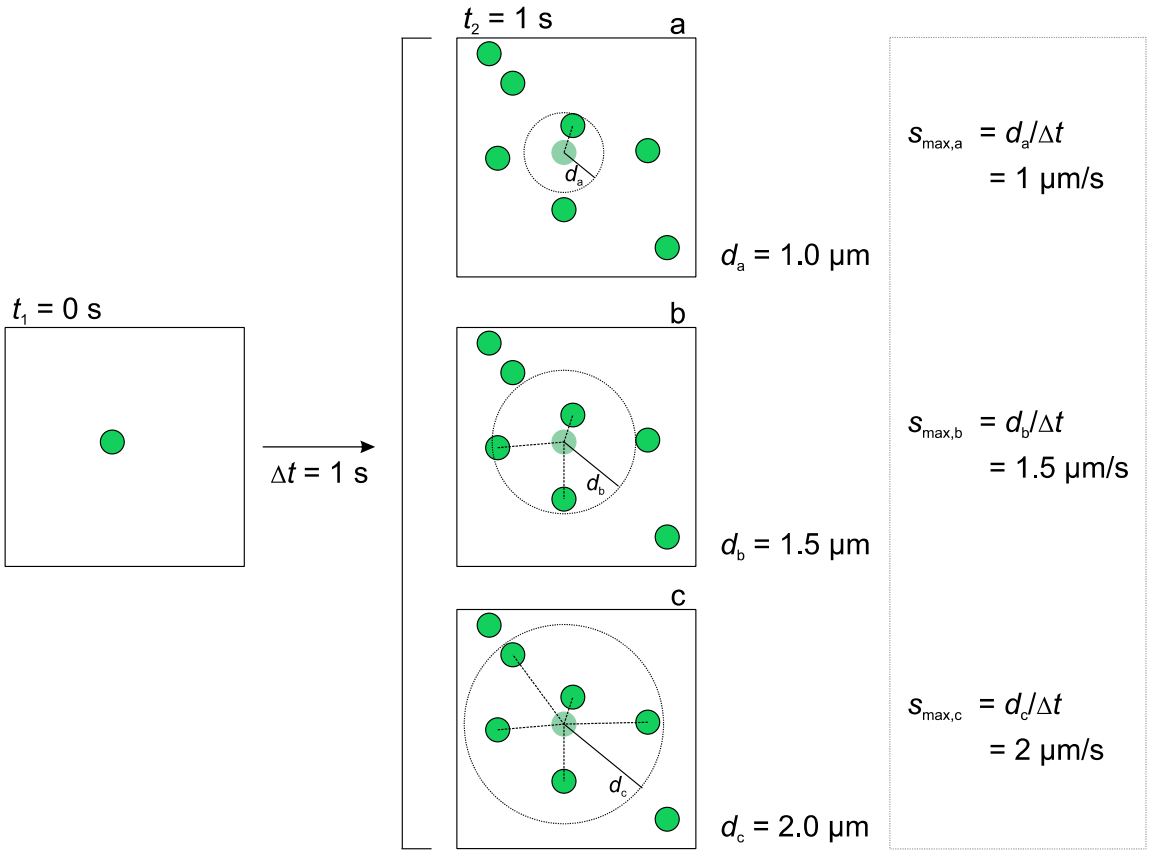

Figure 3.41: Effect of the maximal search distance for connections of particles in consecutive time frameson the speed limit of their movement. After detecting the fluorescence intensity maxima of a particle at the first time point (t_1), it has to be connected to the corresponding particle in the next time frame (t_2). To find this particle again, a maximal search distance (d_a, d_b and d_c) has to be set, in which the algorithm looks for possible connections. The larger this maximal search distance the higher is the maximal speed (s_{max}) of the tracked particle, but the more possible match candidates exists, which may lead to false-positive connections.

Due to different numbers of z-frames and therefore a varying acquisition time (cf. Δt in Figure 3.41) used for each cell, the search radius was adjusted for each analyzed cell during the tracking process. The search radius was set to a value that allowed the highest speed value for reconstructing consistent trajectories. Hereby, a standard deviation of 25% within one group of cells described in Table 3.1 was not exceeded. Moreover, the maximum value of the speed

obtained from all trajectories within one group was calculated resulting in smaller values than the speed limit (Table 3.2). This shows that the speed limit does not restrict the maximum speed of the fastest particle.

Table 3.2: Comparison of speed limit and maximum speed. The calculated speed limit (dependent on number of z-stacks and the search radius for trajectory-connection) for all cells within one group with standard deviation and the maximal speed of all trajectories within one group also with standard deviation is given. The respective n is written italic letters below.

Group		**Speed limit [µm/s]** **mean ± stDev** ***number of cells***	**Max speed [µm/s]** **mean ± stDev** ***number of trajectories***
1) HEK293	$Ca_V1.2$	0.82 ± 0.09 *10*	0.59 ± 0.16 *2375*
	$Ca_V\beta2a$	0.75 ± 0.07 10	0.59 ± 0.11 *2947*
2) HEK293	$Ca_V1.2$	0.91 ± 0.16 *8*	0.59 ± 0.20 *2581*
	$Ca_V\beta2b$	1.00 ± 0.24 *8*	0.68 ± 0.26 *3051*
3) Flp-In T-REx	$Ca_V1.2$	0.84 ± 0.24 *7*	0.48 ± 0.08 *1523*
	$Ca_V\beta2a$	0.96 ± 0.20 *7*	0.60 ± 0.16 *869*
4) Flp-In T-REx	$Ca_V1.2$	0.62 ± 0.13 *7*	0.29 ± 0.08 *766*
	$Ca_V\beta2a$	0.93 ± 0.19 *7*	0.41 ± 0.07 *460*

3.7.3 Analysis of trajectories and evaluation of motion parameters of $Ca_V1.2$

The single particle tracking analysis, as described above, was done for all groups of cells (cf. Table 3.1) and the resulting trajectories were used to investigate dynamic parameters of the movement and to evaluate the type of motion. The analysis of the trajectories dynamics in the present study aimed at:

1) the investigation of the impact of the two isoforms of $Ca_V\beta$ on the transport dynamics of $Ca_V1.2$,
2) the assessment of the cotransport of $Ca_V1.2$ and $Ca_V\beta$ during the channel's itinerary and
3) the distinction of $Ca_V1.2$ transport dynamics during the secretory and retrograde transport.

From the analysis of trajectories various parameters describing the motion of particles can be extracted. In particular two of these parameters will be highlighted in the following: i) the length of the displacement within one trajectory and ii) the mean value of the speed during its itinerary.

To investigate the different impact of $Ca_V\beta$ isoforms on $Ca_V1.2$ transport, the displacement and the mean speed for all $Ca_V1.2$ trajectories obtained from cells expressing $Ca_V1.2$ with $Ca_V\beta2a$ and $Ca_V1.2$ with $Ca_V\beta2b$ were plotted in histograms (Figure 3.42).

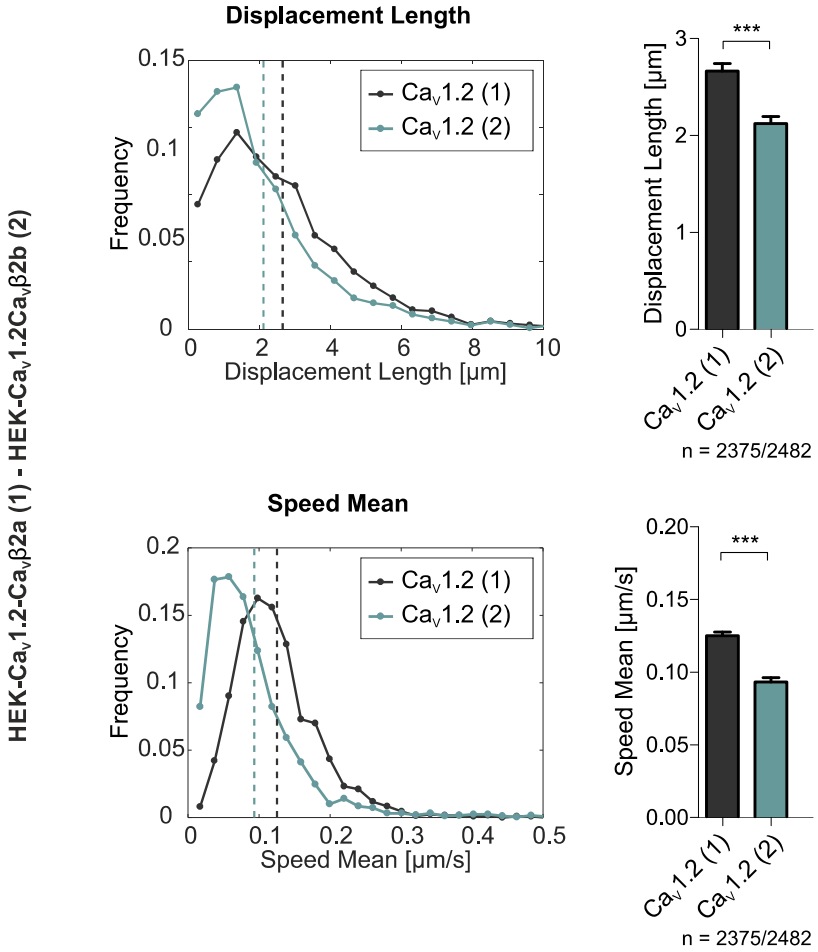

Figure 3.42: $Ca_V\beta$ isoforms have different effect of the frequency distributions of $Ca_V1.2$'s mean speed and displacement values. Distribution frequency of displacement length values (upper row) and mean speed values (lower row) of all trajectories obtained by $Ca_V1.2$ within one group. In every graph, values are compared between group 1 (HEK-$Ca_V1.2$-$Ca_V\beta2a$, grey) and 2 (HEK-$Ca_V1.2$-$Ca_V\beta2b$, green). The vertical dotted lines represent the corresponding mean values. Counts are normalized by the total number of observations. Bar plots beside each histogram show the respective mean values of the displacement length (upper row) and mean speed (lower row). Each bar represents the mean of n analyzed trajectories (number given below the bars) with its 95% confidence interval. Statistical difference between the fractions was tested with One-Way ANOVA followed by post hoc Bonferroni's Multiple Comparison test ($p \leq 0.01$). Stars represent statistical significances between the two series.

The histograms in Figure 3.42 demonstrate that $Ca_V1.2$ coexpressed with $Ca_V\beta2a$ (group 1) shows more trajectories having longer displacement length and higher mean speed values than when coexpressed with $Ca_V\beta2b$ (group 2). The mean values for the length of the displacement and the mean speed show that in average $Ca_V1.2$ moves longer distances and faster with $Ca_V\beta2a$ than with $Ca_V\beta2b$. Thus the two $Ca_V\beta$ isoforms differently influence the transport of the $Ca_V1.2$ channel.

This effect might be due to their chemical properties. Palmitoylated $Ca_V\beta2a$ not only binds to $Ca_V1.2$ but also can anchor to the vesicles membrane strengthening the association to the channel. Thus, cytosolic $Ca_V\beta2b$ is supposed to dissociate more frequent from the α_1-subunit (Campiglio et al. 2013, Stotz et al. 2004) that might lead to an interruption of the transport and therefore to a decreased displacement and lower speed.

A putative cotransport of $Ca_V1.2$ and $Ca_V\beta$ was deduced by visual inspection of laser scanning confocal images from cells expressing both subunits (cf. Figure 3.35). I rationalize that the dynamic parameters describing the transport for the individual subunits during a cotransport must overlap. A direct comparison of the distribution of the mean speed and displacement length values for the each subunit in group 1 and 2 is shown in Figure 3.44. The histograms for $Ca_V1.2$ and $Ca_V\beta$ in each condition show similar distributions.

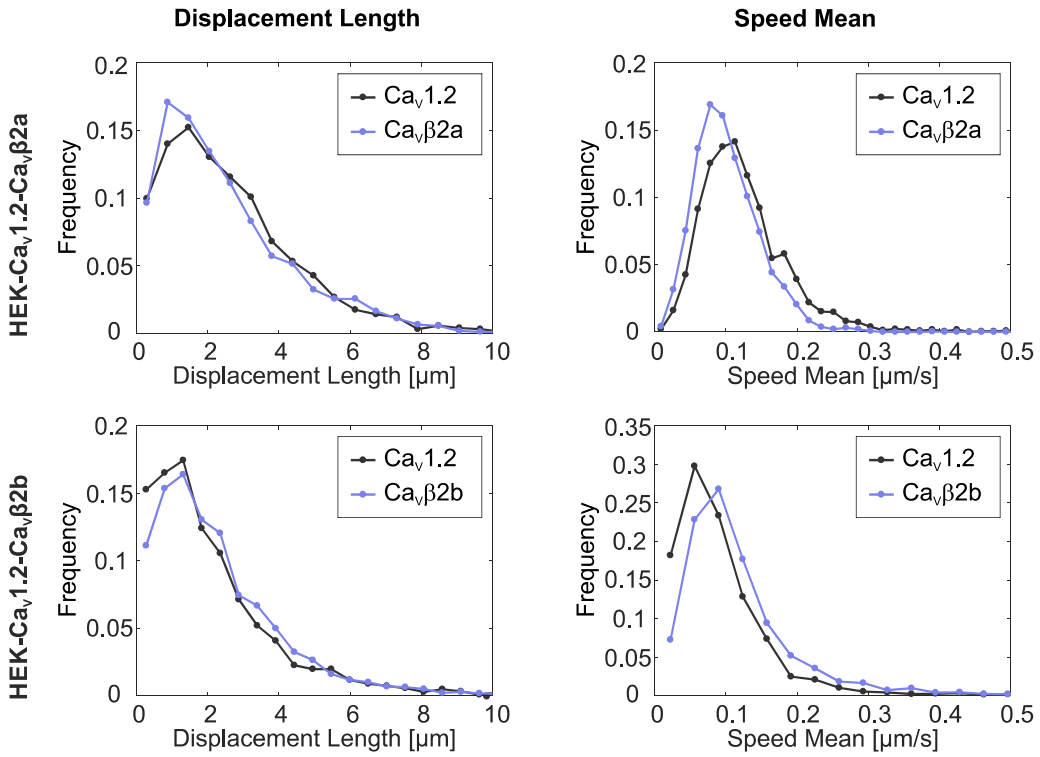

Figure 3.43: Histograms of trajectories displacement length and mean speed values. Distribution frequency of displacement length values (left column) and mean speed values (right column) of all trajectories within one group. Trajectories obtained by $Ca_V1.2$ are presented by a dark grey line, trajectories of $Ca_V\beta$ by a blue line. Counts are normalized by the total number of observations.

In both groups, the curves for $Ca_V1.2$ and $Ca_V\beta$ have the same range of values for the displacement length and mean speed and share the major part of the distribution. The major number of trajectories for both, $Ca_V1.2$ and $Ca_V\beta$, reach a displacement length of around 1 µm. The maximal value of 10 µm occurs for both subunits at very low frequency. The mean speed values range from 0 µm/s to a maximum of 0.5 µm/s with the highest frequencies reached at around 0.1 µm/s. For cells expressing $Ca_V1.2$ with $Ca_V\beta2a$, the latter show a greater fraction of particles moving with lower speed than $Ca_V1.2$. Conversely, in cells expressing $Ca_V1.2$ with $Ca_V\beta2b$, $Ca_V1.2$ shows a peak of higher frequencies at slower mean speed than $Ca_V\beta2b$. Based on the assumption that $Ca_V\beta2b$ dissociates faster from the channel, the amount of channels not associated with a β-subunit and therefore, the amount of channels being stuck in the cytoskeleton network, is higher than with $Ca_V\beta2a$. This pool of "slower" channels that are not associated with a β-subunit might be packed within aggresomes forming an 'immobile' cluster (Zaarur et al. 2008). The same can be true for the pool of $Ca_V\beta2a$ moving slower than $Ca_V1.2$.

The distribution of displacement length and mean speed values for the trajectories obtained from Flp-In cells induced for $Ca_V\beta2a$ and transfected with $Ca_V1.2$ (group 3, Flp-In-$Ca_V1.2$) show similar pattern as for cotransfected HEK293 cells (Figure 3.44, upper row). These observations points towards a cotransport of $Ca_V1.2$ and $Ca_V\beta$. However, in the last group (Flp-In-$Ca_V1.2$-Halo) different distribution pattern of $Ca_V1.2$ and $Ca_V\beta$ can be found. More β-subunits are moving a longer distance than 2 µm compared to the corresponding α-subunits (Figure 3.44, lower row).

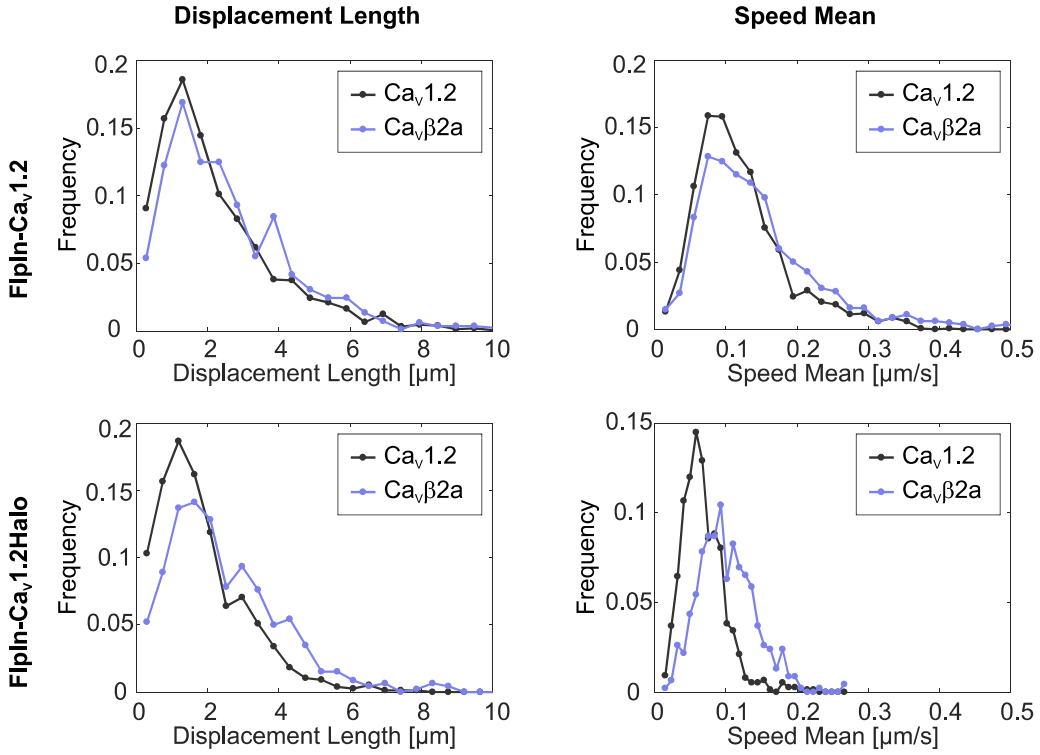

Figure 3.44: Similar histograms indicate a cotransport of $Ca_V1.2$ and $Ca_V\beta$ on its forward pathway, but not after internalization. Distribution frequency of displacement length values (left column) and mean speed values (right column) of all trajectories within one group. Trajectories obtained by $Ca_V1.2$ are presented by a dark grey line, trajectories of $Ca_V\beta$ by a blue line. Counts are normalized by the total number of observations.

$Ca_V1.2$-HaloTag (group 4) shows higher frequencies of shorter trajectories compared to the corresponding $Ca_V\beta$. The distribution of the mean speed values differs between the two Flp-In cell groups. In Flp-In cells expressing $Ca_V1.2$-mNeonGreen both, $Ca_V1.2$ and $Ca_V\beta2a$, share a large pool of speed values, whereas $Ca_V1.2$-HaloTag shows only a partial overlap with the speed distribution of the corresponding $Ca_V\beta2a$. This suggests that both subunits are not cotransported along the endosomal pathway. This is the first hint that internalized channels differ in their subunit composition from channels being transported along the secretory pathway.

While writing my thesis, a statistical analysis of the mean speed histograms of $Ca_V1.2$ and $Ca_V\beta2a$ was done in collaboration with Daniel Kortzak. If $Ca_V1.2$ and $Ca_V\beta2a$ are moving together, their distributions should share at least one component. This possibility was tested by fitting a mixture of three Gaussians independent to the distributions of both, $Ca_V1.2$ and $Ca_V\beta2a$, obtained from $Ca_V\beta2a$ expressing cells from groups 1, 3 and 4. The best fit yielded

only one common peak for $Ca_V1.2$ and $Ca_V\beta2a$ in cells from group 1 and 3 (Table 3.3). An F-test confirmed that the values for the largest peak are not significantly different (p-value, Table 3.3).

Table 3.3: Components of $Ca_V1.2$ and $Ca_V\beta2a$ mean speed distribution with statistical significance.

	Peak 1	**Peak 2**	**Peak 3**
$Ca_V1.2$	0.063	0.103	0.172
$Ca_V\beta2a$	0.076	0.127	0.174
p-value (F-test)	*< 0.01*	*< 0.01*	*0.9*

The data indicates that even though the mean speed distributions as a whole are not identical, they share a common component that moreover, represents the fastest one. This fast pool is absent in the mean speed distribution of $Ca_V1.2$-Halo. This suggests that this fast component is part of the secretory transport and thus during this pathway the $Ca_V1.2$ α_1 pore-forming subunit and the accessory β-subunit travel together.

A comparison of $Ca_V1.2$-trajectories from group 3 and 4 highlights the differences in thetransport along the secretory and the endosomal transport (Figure 3.45).

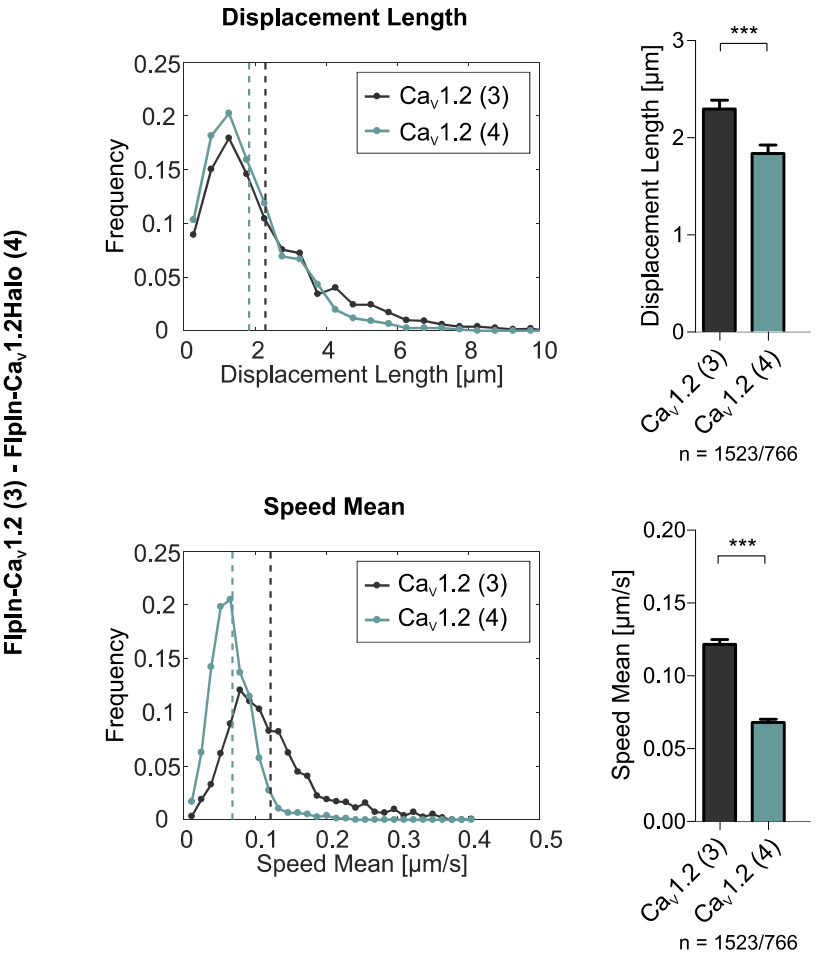

Figure 3.45: Histograms of trajectories from $Ca_V1.2$ and $Ca_V1.2$-Halo differ in displacement length and mean speed values distribution. Distribution frequency of displacement length values (upper row) and mean speed values (lower row) of all trajectories obtained by $Ca_V1.2$ within one group. In every graph values are compared between group 3 (FlpIn-$Ca_V1.2$, grey) and 4 (FlpIn-$Ca_V1.2$-Halo, green). The vertical dotted lines represent the corresponding mean values. Counts are normalized by the total number of observations. Bar plots beside each histogram show the respective mean values of the displacement length (upper row) and mean speed (lower row). Each bar represents the mean of n analyzed trajectories (number given below the bars) with its 95% confidence interval. Statistical difference between the fractions was tested with One-Way ANOVA followed by post hoc Bonferroni's Multiple Comparison test ($p \leq 0.01$). Stars represent statistical significances between the two series.

The frequencies of the displacement values of $Ca_V1.2$ trajectories from group 3 and 4 differ in their distribution (cf. mean values in Figure 3.45, upper row), however, they also share a pool of values. The distributions of the mean speed values also differ significantly (cf. mean values in Figure 3.45, lower row). Here it is clearly recognizable in the histogram that the speeds from $Ca_V1.2$-HaloTag only partially overlap with $Ca_V1.2$ from group 3. It is striking that the endocytosed $Ca_V1.2$-HaloTag move slower, with a maximal mean speed of around 0.2 µm/s, than the $Ca_V1.2$-mNeonGreen from group 3 which travel on average faster than 0.3 µm/s.

These differences result from the fact that group 4 includes only internalized $Ca_V1.2$ on their retrograde trafficking pathway and group 3 includes $Ca_V1.2$-particle moving in both directions to and from the plasma membrane.

This is confirmed by the fact that the range of speed values calculated for endocytosed $Ca_V1.2$-HaloTag-trajectories also exist within the range of speed values determined from $Ca_V1.2$ moving in all directions. Thus, a distinction of $Ca_V1.2$ transport dynamics along the secretory and retrograde transport was identified.

To study these differences in more detail and to evaluate the type of motion for every obtained trajectory the respective mean-square displacement (MSD) curves were calculated, which are proportional to the diffusion coefficient of each particle. Figure 3.46 gives an overview of the general process to analyze the type of motion from MSD data.

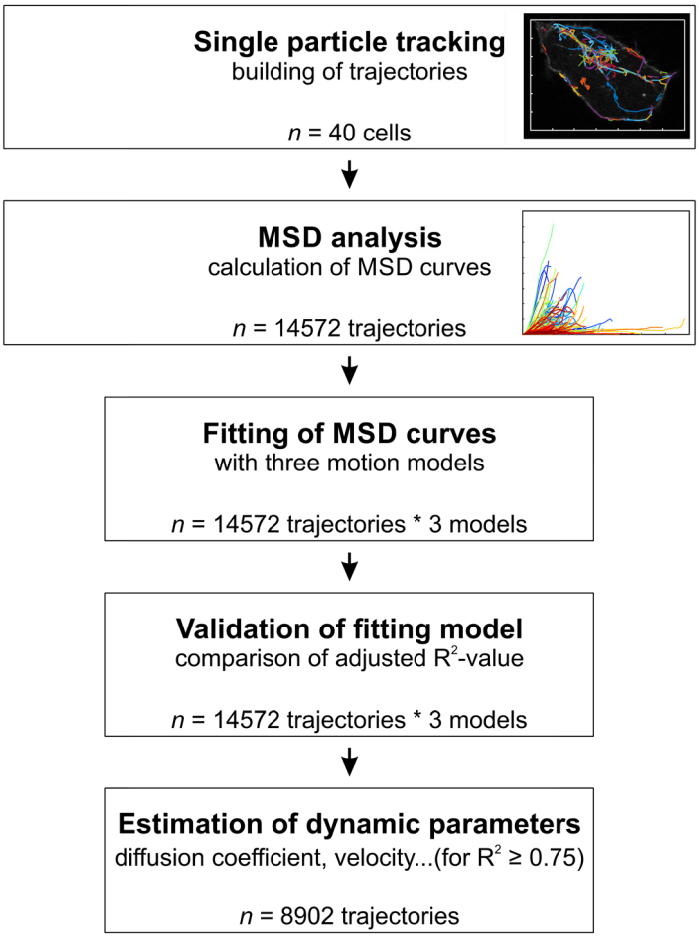

Figure 3.46: Scheme of the process of the analyzation. After the single particle tracking, the obtained trajectories were used to calculate the respective MSD curves. Each curve was fitted with three different models. The best R^2 value validates the estimation of dynamic parameters.

Transport of particles combines different types of motion, directed motion along the cytoskeleton driven by motor proteins as well as passive motion. I used three models to fit the MSD curves of all found trajectories within all groups (cf. 2.9.1). The fitting process is shown in Figure 3.47. The first model describes a diffusion process plus flow and therefore a normal Brownian motion of the particles with a directed movement factor. The second model describes anomalous diffusion. This model is known to be true for vesicles in living cells due to the molecular crowding of the intracellular milieu (Banks and Fradin 2005). The α-exponent depends on the type of anomalous diffusion and its value reflects a directed or non-directed movement. The third model adds a flow component to the model of anomalous diffusion.

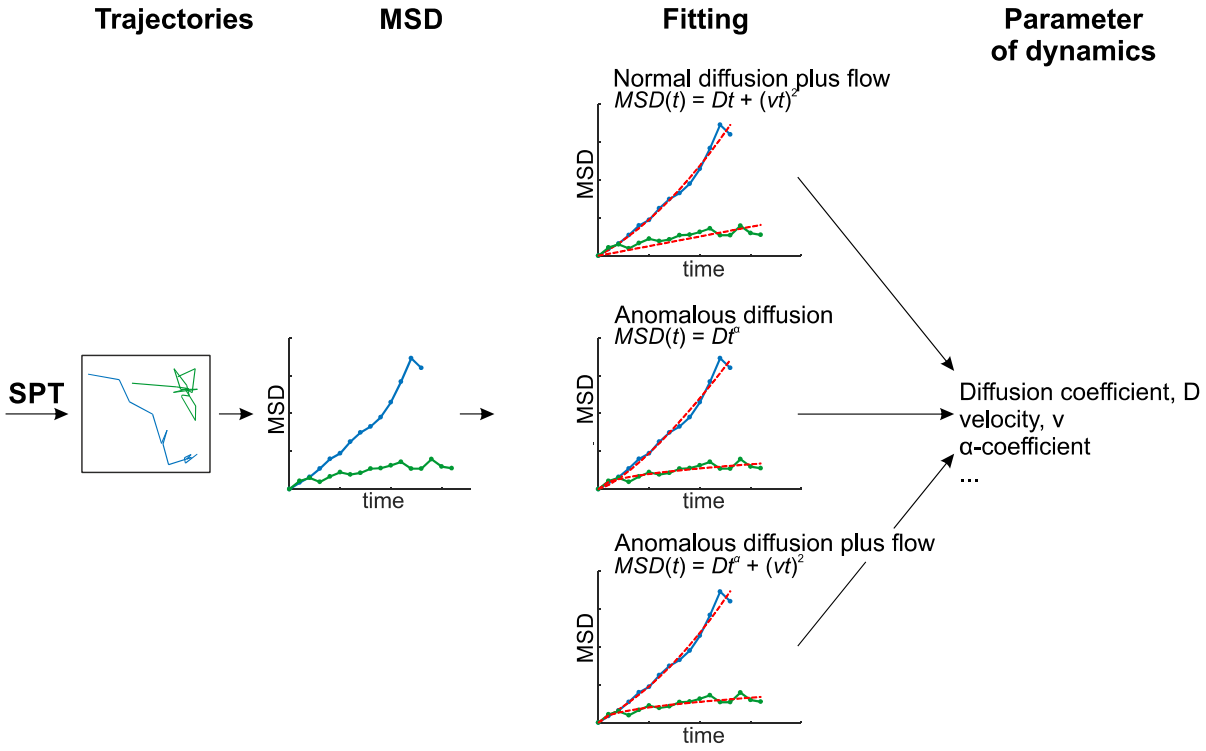

Figure 3.47: Analysis procedure for the fitting of the MSD curves for all trajectories. MSD curves of all trajectories were calculated and fitted by three models: diffusion plus flow, anomalous diffusion and anomalous diffusion plus flow. From these fits dynamic parameters were calculated.

The goodness of the fit was evaluated by the adjusted R-squared value. This is a modification of R-squared that adjusts for the number of explanatory terms in a model relative to the number of data points in order to avoid misleadingly high R-squared values due to more variables within the fitting model. It represents the fraction by which the square of the

standard error of a multiple regression is less than the variance of the dependent variable. This means that the standard error of the regression goes down as adjusted R-squared goes up. Since all fitted models used the same dependent variable the model with the highest adjusted R-squared has the lowest standard error of the regression. To determine the best fitting model all trajectories were fitted with each model regression. From this analysis the mean R-squared value for each group was calculated to assess the goodness of the fit for the whole data set (Figure 3.48).

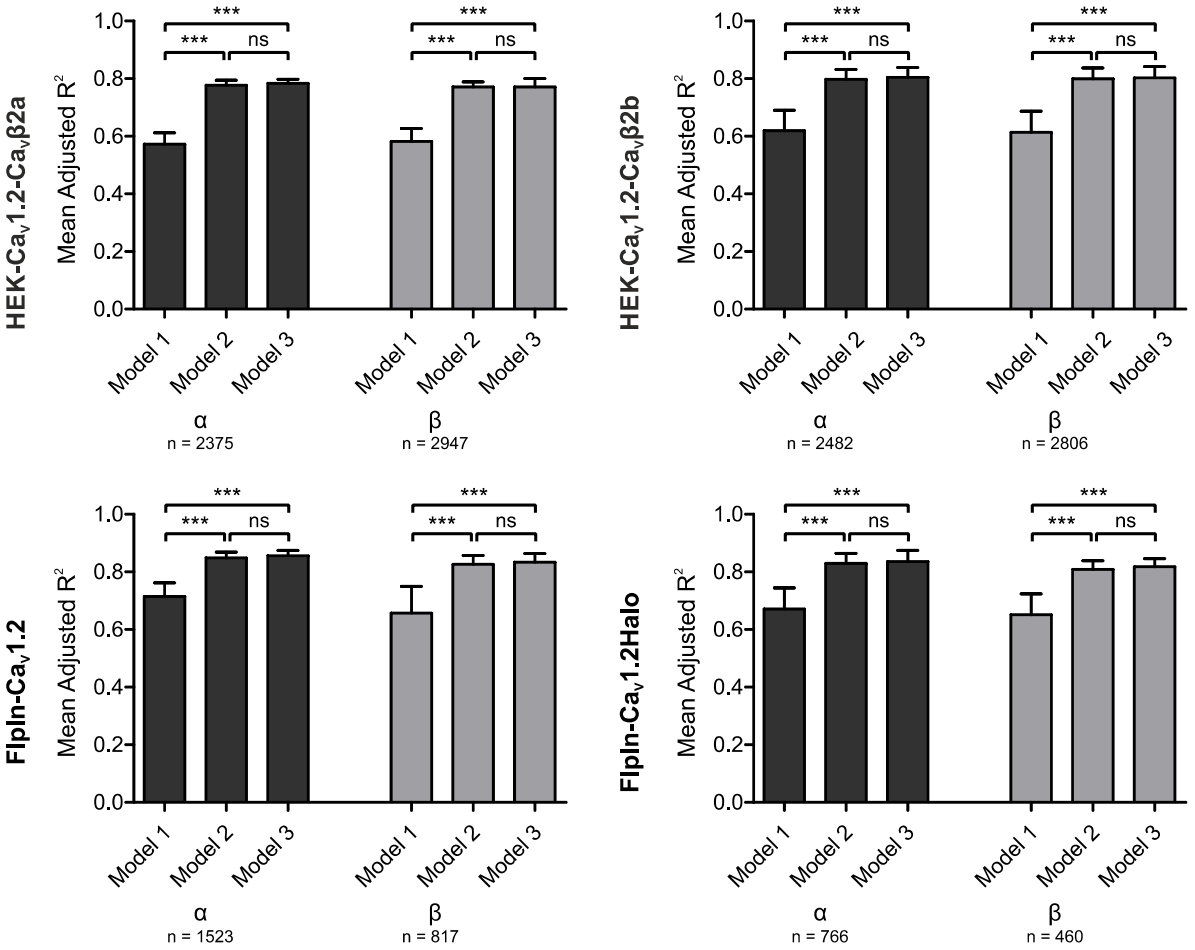

Figure 3.48: Comparison of fitting models revealed the motion of $Ca_V1.2$ as anomalous diffusion. Mean of the adjusted R-squared values of three models fitted to the MSD curves of all trajectories determined from the movement of $Ca_V1.2$ (α, dark grey) and $Ca_V\beta$ (β, light grey) in each analyzed group (indicate beside each plot). Model 1: Normal diffusion plus flow, Model 2: Anomalous Diffusion, Model 3: Anomalous Diffusion plus flow. Each bar represents the mean of n analyzed trajectories (number given below the bars) with its 95% confidence interval. Statistical differences between the fractions were tested with One-Way ANOVA followed by post hoc Bonferroni's Multiple Comparison test ($p \leq 0.001$). Stars represent statistical significances between the two series, ns = no significant.

Figure 3.48 shows that for both subunits in all four groups of cells the mean adjusted R-squared values for the first model 'Normal diffusion plus flow' are significantly lower than for the other two models. However there is no statistical significant difference between the R-squared values of Model 2 and 3, describing anomalous diffusion without and with flow, respectively. Thus, the majority of the determined trajectories are related to an anomalous diffusion either with or without a directed flow component. Since the second model is sufficient to explain the observed data with less parameter, this model was used to determine the diffusion coefficients. Moreover, the value of the α-exponent from this model was examined to characterize the type of anomalous diffusion. For the analysis only trajectories with fitted MSD curves yielding adjusted R-squared values larger than 0.75 were used. This indicates that the model explains at least 75% of the variability of the measured data around its mean.

The distributions of the diffusion coefficients calculated for $Ca_V1.2$ and $Ca_V\beta$ are not symmetric and show a wide range of values from $0.1 \cdot 10^{-5}$ to 1.3 $\mu m^2/s$. To visualize all data the bins of the histograms were distributed uniformly on a logarithmic scale (Figure 3.49) and the median was calculated to report the central tendency.

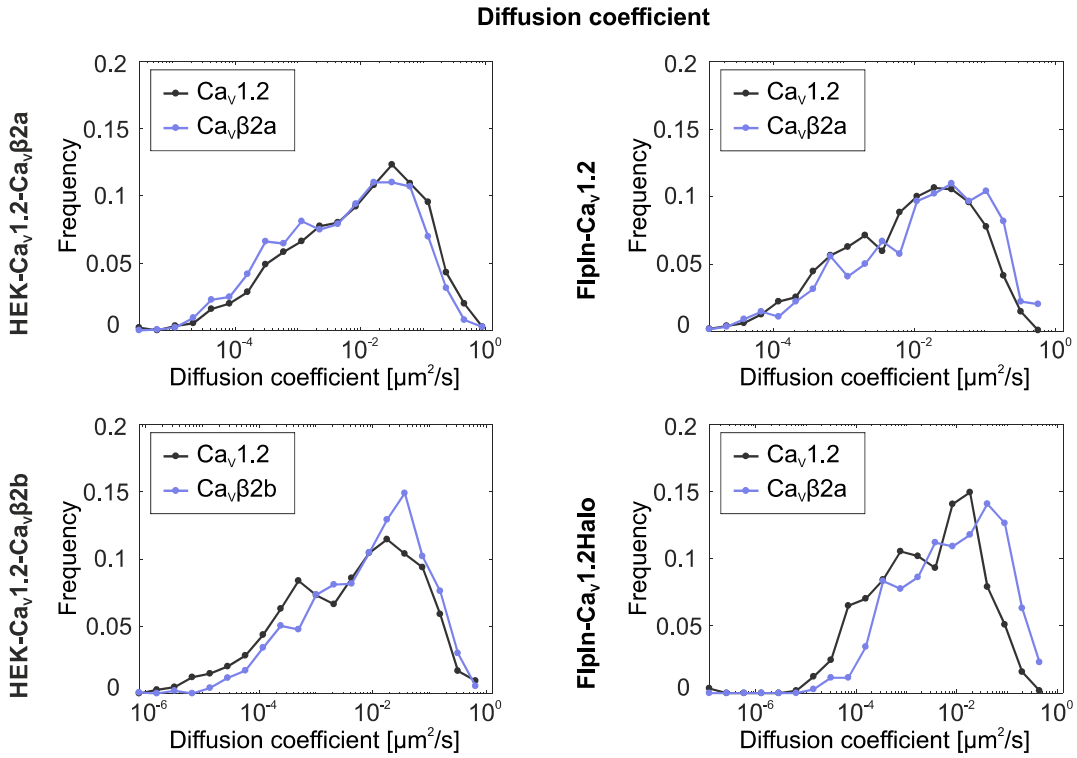

Figure 3.49: Histograms of trajectories diffusion coefficient show similar courses for Ca$_V$1.2 and Ca$_V$β. The graphs show the distribution frequency of the diffusion coefficients of all trajectories within one group. Trajectories obtained by Ca$_V$1.2 are presented by a dark grey line, trajectories of Ca$_V$β by a blue line. Counts are normalized by the total number of observations.

The frequency distributions of the diffusion coefficients of Ca$_V$1.2 and of Ca$_V$β within the first three groups show a similar course (Figure 3.49). This is expected for cotransport mechanism of the subunits because with the same diffusion coefficients the underlying physical principle of the movement is the same. However, in group 4 a greater discrepancy of the frequency distributions of the diffusion coefficients estimated for Ca$_V$1.2-Halo and Ca$_V$β after internalization is observed. All together, these data emphasizes our idea that during endocytosis an association of α- and β- subunit is not crucial but both subunits are associated during the forward trafficking.

The direct comparison of the effect of the two Ca$_V$β isoforms on the diffusion coefficient of Ca$_V$1.2 displays a slightly higher motility of the channel coexpressed with Ca$_V$β2a (Figure 3.50, left histogram) (median diffusion coefficient of HEK-Ca$_V$1.2-Ca$_V$β2a 0.0120 μm^2/s interquartile range (IQR) 0.0016 – 0.0517, median diffusion coefficient of HEK-Ca$_V$1.2-Ca$_V$β2b 0.0062 μm^2/s IQR 0.0006 – 0.0312). This higher motility with Ca$_V$β2a was already

insinuated from the comparison of the mean speed of $Ca_V1.2$ in coexpression experiments with either $Ca_V\beta2a$ or $Ca_V\beta2b$ (Figure 3.43). The lower diffusion coefficient values for $Ca_V1.2$ associated with $Ca_V\beta2b$ (group 2) could be explained by an increased dissociation rate of $Ca_V\beta2b$ in comparison to $Ca_V\beta2a$.

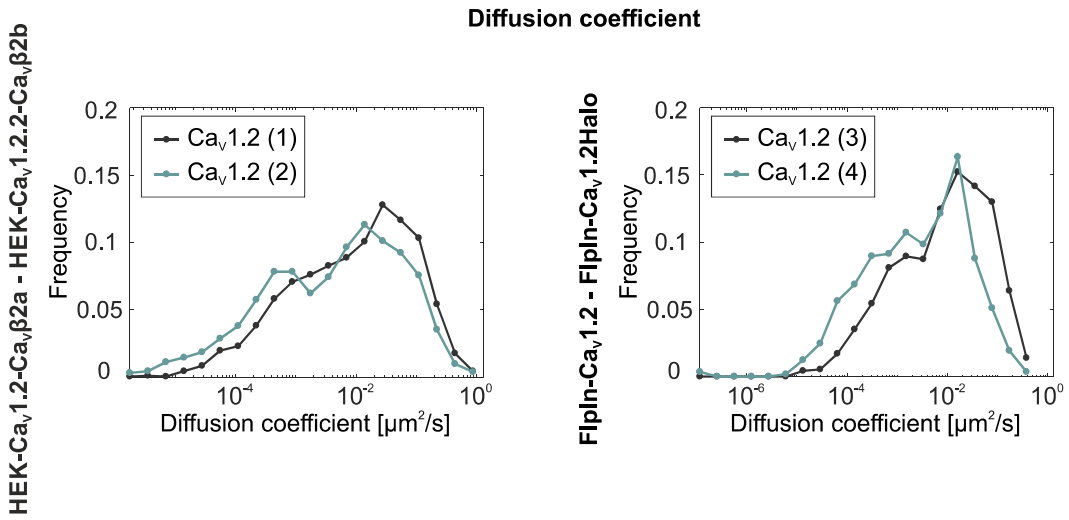

Figure 3.50: Histograms of $Ca_V1.2$ trajectories' diffusion coefficients differ between secretory and internalized channels. Distribution frequency of diffusion coefficient values of all trajectories obtained by $Ca_V1.2$ within one group. Values are compared between group 1 (HEK-$Ca_V1.2$-$Ca_V\beta2a$, grey) and 2 (HEK-$Ca_V1.2$-$Ca_V\beta2b$, green) (left histogram) as well as between group 3 (FlpIn-$Ca_V1.2$, grey) and 4 (FlpIn-$Ca_V1.2$-Halo, green) (right histogram). Counts are normalized by the total number of observations.

Comparing the distribution of diffusion coefficients, the curve of endocytosed $Ca_V1.2$-Halo strongly differs from that of $Ca_V1.2$ of group 3, that includes both forward and retrograde trafficking (Figure 3.50, right histogram) (median diffusion coefficient of FlpIn-$Ca_V1.2$ 0.0119 $\mu m^2/s$ interquartile range (IQR) 0.0019 – 0.0433, median diffusion coefficient of FlpIn-$Ca_V1.2$-Halo 0.0027 $\mu m^2/s$ IQR 0.0004 – 0.0317). As already mentioned, the diffusion coefficients were obtained from MSD curves fitted to an anomalous diffusion mode that can be related with super- or sub- anomalous diffusion process (cf. Figure 3.48). Within this context, this indicates that forward trafficking of $Ca_V1.2$ not only differ in the subunit stoichiometry but also in the anomalous component reflected in the α-coefficient.

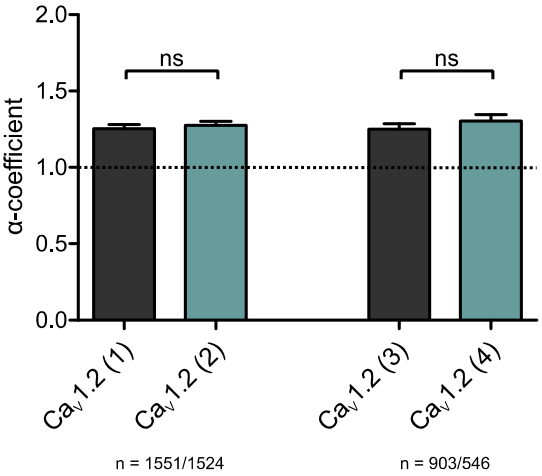

Figure 3.51: Mean values of α-coefficients for all Ca$_V$1.2 trajectories implicate super anomalous diffusion. Mean values of the α-coefficient of all trajectories determined from the movement of Ca$_V$1.2 in each analyzed group (1: HEK-Ca$_V$1.2-Ca$_V$β2a; 2: HEK-Ca$_V$1.2-Ca$_V$β2b; 3: Flp-In-Ca$_V$1.2; 4: Flp-In-Ca$_V$1.2-Halo). Each bar represents the mean of n analyzed trajectories (number given below the bars) with its 95% confidence interval. Statistical differences between the fractions were tested with One-Way ANOVA followed by post hoc Bonferroni's Multiple Comparison test ($p \leq 0.01$). ns = no significant.

The mean values of the α-coefficient, calculated from the MSD curves of Ca$_V$1.2 trajectories in all four groups is higher than 1.0 (Figure 3.51). This implicates a super anomalous diffusion as the main type of movement for Ca$_V$1.2 with both isoforms of Ca$_V$β as well as for endocytosed channels. This is expected for an active transport of Ca$_V$1.2-containing vesicles along cytoskeletal tracks driven by motor proteins.

If the trajectories are separated according to their displacement length, significant differences of the α-coefficients for long (≥ 2 µm) and short (< 2µm) trajectories can be observed in all groups (Figure 3.52). All trajectories for Ca$_V$1.2 longer than 2 µm have a mean α-coefficient larger than 1.4, whereas trajectories covering shorter displacements show a mean α-coefficient around 1.0.

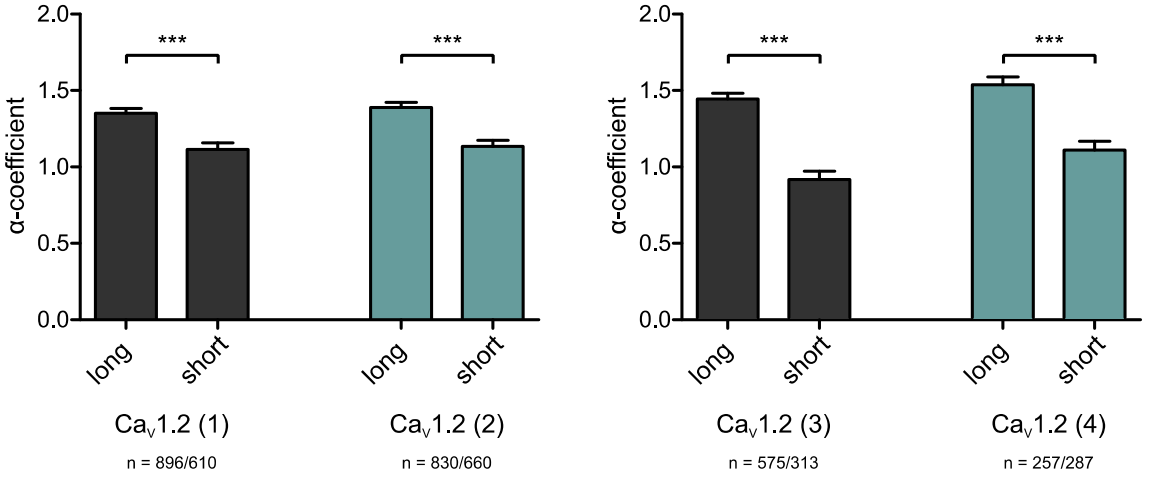

Figure 3.52: Statistical analysis of trajectories α-coefficients in filtered groups revealed distinct types of motion. Mean values with 95% confidence interval of the α-coefficients of trajectories determined from the movement of $Ca_V1.2$ in each analyzed group (1: HEK-$Ca_V1.2$-$Ca_V\beta2a$; 2: HEK-$Ca_V1.2$-$Ca_V\beta2b$; 3: Flp-In-$Ca_V1.2$; 4: Flp-In-$Ca_V1.2$-Halo). Trajectories are grouped in 'long': displacement length ≥ 2 µm and 'short': displacement length < 2µm. Statistical differences between the fractions were tested with One-Way ANOVA followed by post hoc Bonferroni's Multiple Comparison test ($p \leq 0.01$). Stars represent statistical significances between the two series.

For Brownian motion the α-coefficient equals 1 and for anomalous diffusion it deviates from one. Motions with values of $1.4 \leq \alpha \geq 2$ are considered to be active-mediated vesicle movement, whereas $0 < \alpha < 1.4$ ($\alpha \neq 1$) are typical for passive motion (Ahmed et al. 2013, Lund et al. 2014, Zajac et al. 2013). Applied to our data, the values obtained for α-coefficients are consistent with this, since $Ca_V1.2$ displaying different type of motions, by which the channel is transported actively over long distances but also shows sections of confined movement.

The long range sections of the channels itinerary to the plasma membrane would represent active transport of $Ca_V1.2$ supported by motor proteins along cytoskeleton tracks. During this transport the travelling might be interrupt.

To investigate these transitions between passive and active motions individual trajectories of $Ca_V1.2$ were analyzed segmentally.

From the cell showed in Figure 3.39 four trajectories, based on different shapes and directional motion towards the plasma membrane, were selected for further analysis. For spatial orientation within the cell, the four trajectories are shown in Figure 3.53 together with the laser scanning confocal image of the corresponding cell.

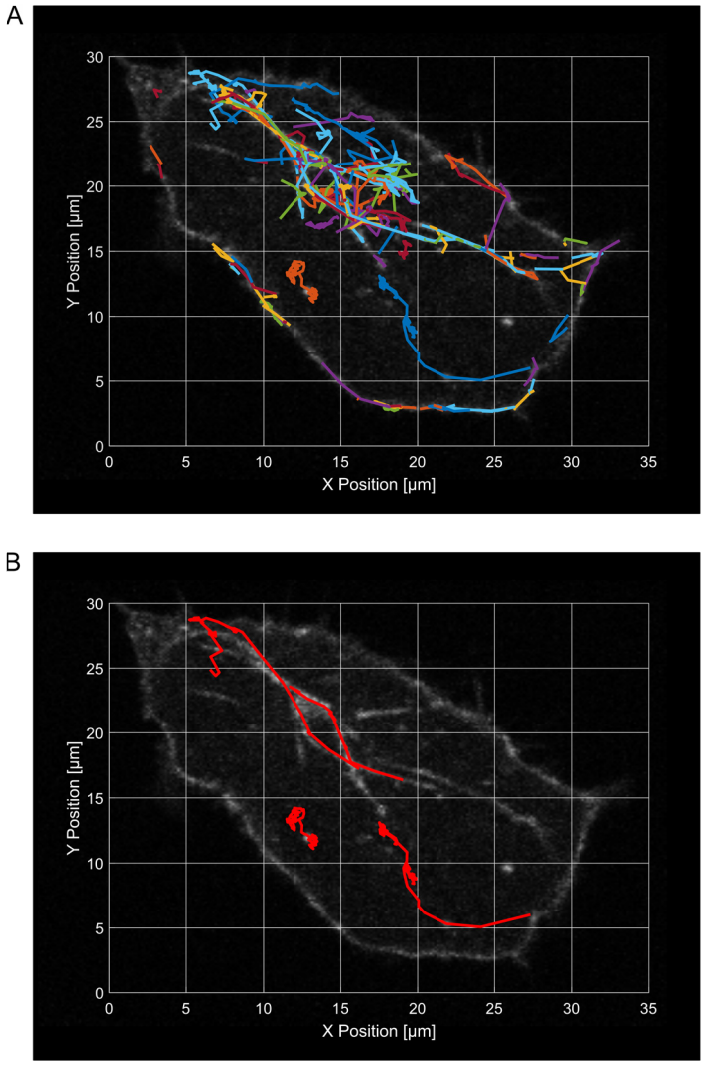

Figure 3.53: Raw trajectories of $Ca_V1.2$ in the cell context. A) Sum of all trajectories of $Ca_V1.2$ found in one representative HEK293 cell with the corresponding Laser scanning confocal image of the cell in the background. B) Four different shaped trajectories selected for further analysis.

The selected trajectories are shown in different colors in two-dimensional and three-dimensional plots (Figure 3.54). Two trajectories clearly show long-distance displacement of the particle (green and yellow). The blue trajectory shows a mixture of extended and interrupted by space restricted segments. The red trajectory consists only of a confined course of movement.

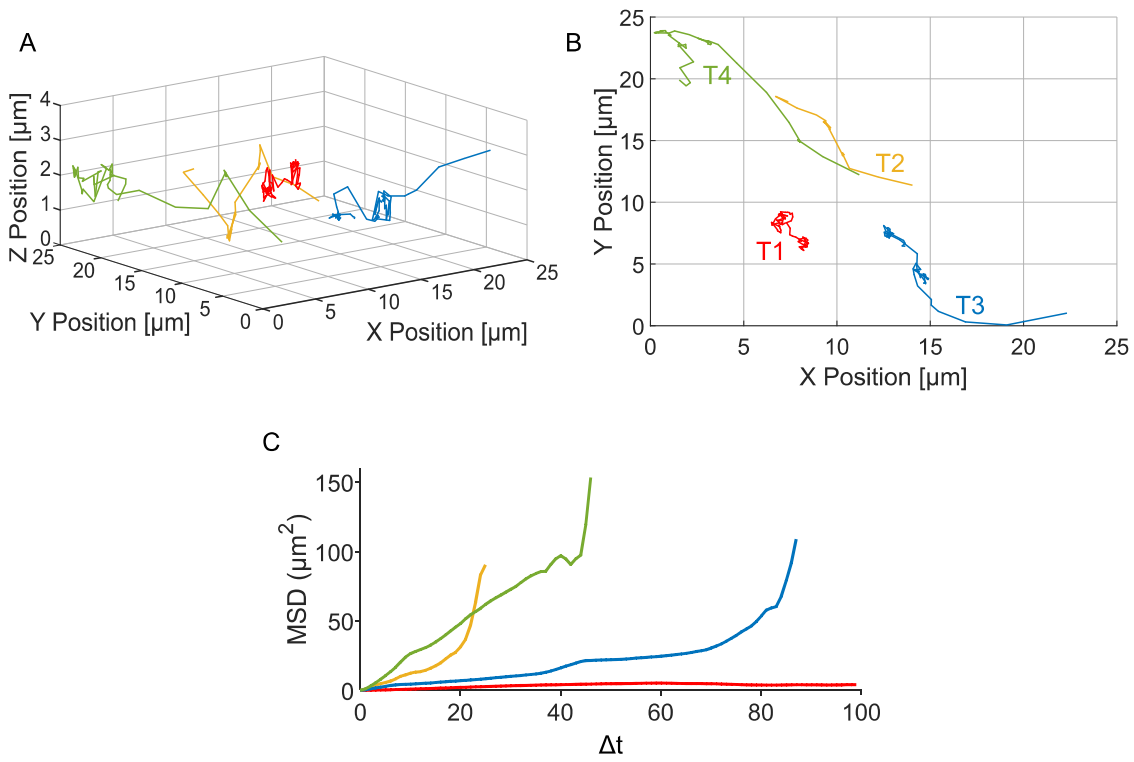

Figure 3.54: Selected trajectories differ in shape and calculated MSD curves show distinct slopes. Chosen trajectories (T1-T4) plotted in A) three-dimensional and B) two-dimensional space. C) Corresponding mean-square displacement-curves for all shown trajectories, color-coded in the respective color.

From all selected trajectories the MSD curves where calculated (Figure 3.54C). It can be noticed that the calculated MSD curves for the four trajectories (T1 to T4) differ in their slope. Furthermore, each MSD curve comprises different linear components with diverse time dependences resembling the different segments of the corresponding trajectory. For the segmentally analysis, every trajectory was segmented by visual inspection of breaks within the course of the MSD curve. These segments were investigated separately by limiting the fitting model to the corresponding borders. In Figure 3.55 and Figure 3.56 the four chosen trajectories are separated in at least two segments. For a detailed visualization, the path of each trajectory over time is shown in x-, y- and z-direction and the corresponding MSD curve is shown below. The vertical dotted lines present the fitting borders, with corresponding segments in the three-dimensional plot. The beginning of each trajectory (t = 0) is marked by a star. At the bottom, the calculated α-coefficients for each segment are indicated. Please notice that there is a change in the scale in the three-dimensional plots of the trajectories.

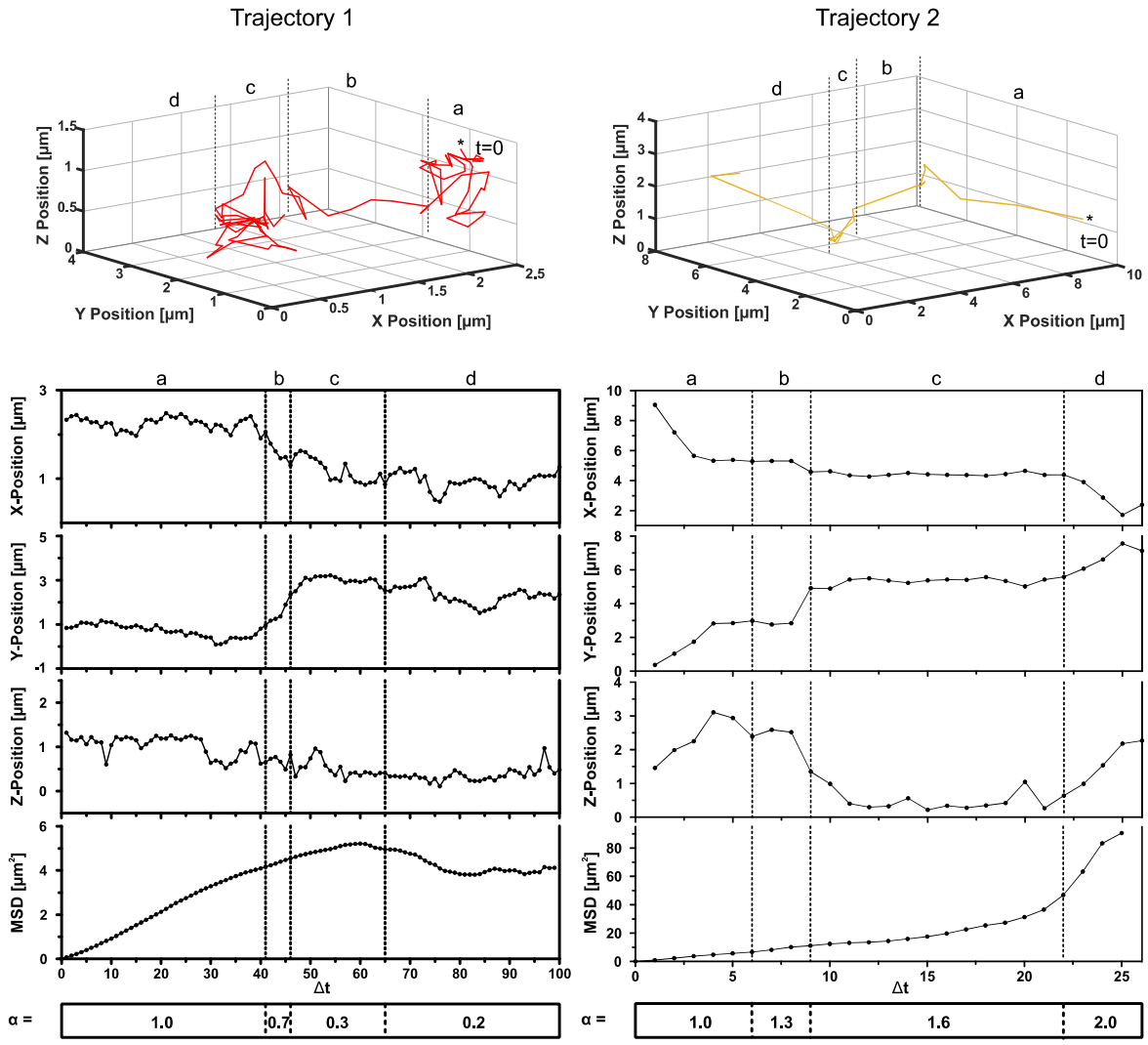

Figure 3.55: Segmented investigation of selected trajectories 1 and 2. Shown are trajectory 1 (red, left column) and 2 (yellow, right column). In descending order the respective trajectory is shown in three dimensional space with a star representing t = 0, followed by its movement over time in x-, y- and z-direction. Below this the corresponding mean square displacement curve is shown. Borders of the segements are marked with vertical dotted lines. At the bottom, the calculated α-coefficient for each segment is presented.

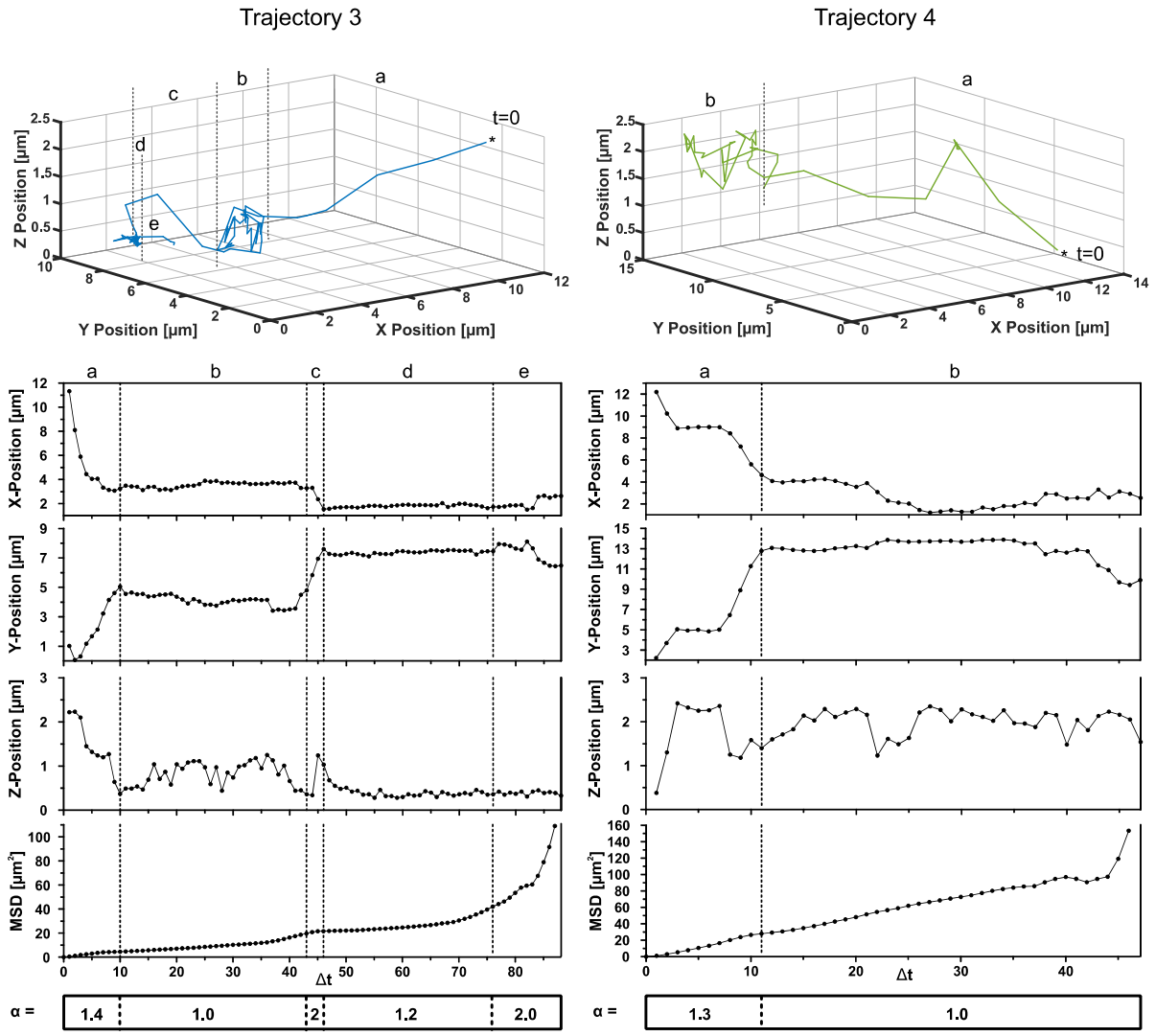

Figure 3.56: Segmented investigation of selected trajectories 3 and 4. Shown are trajectory 3 (blue, left column) and 4 (green, right column).). In descending order the respective trajectory is shown in three dimensional space with a star representing t = 0, followed by its movement over time in x-, y- and z-direction. Below this the corresponding mean square displacement curve is shown. Borders of the segments are marked with vertical dotted lines. At the bottom, the calculated α-coefficient for each segment is presented.

The segmental analysis of the trajectories shows that different segments indeed display different α-coefficients. Trajectory 1 (red) was segmented in four parts (a-d) (Figure 3.55, left panel). For all parts an α-coefficient below 1.4 was calculated that is consistent with confined movement. This agrees with the fact that the major displacement within this trajectory is relatively small, only 1 µm. Trajectory 2 (yellow) presents a larger displacement up to 8 µm length (Figure 3.55, right panel). Here it can be seen that the first two segments, a and b, have

α-coefficients below 1.4, but the fitting of part c and d results in values greater than 1.4, corresponding to an abrupt movement in z-direction followed by a long-distance movement.
A mixture of confined and direct movement was observed in trajectory 3 (blue, Figure 3.56 left panel). Segments a and c give α-coefficient values greater than 1.4, clearly corresponding to the linear structures in the trajectory. Segments b and d of trajectory 3 demonstrate a random motion, resulting in α-coefficient values below 1.4 and therefore, indicating the occurrence of a confined movement.
Trajectory 4 (green) was segmented in only two parts, one extended part and a restricted part (Figure 3.56 right panel). Despite of the linear segment, both α-coefficients calculated are below 1.4.

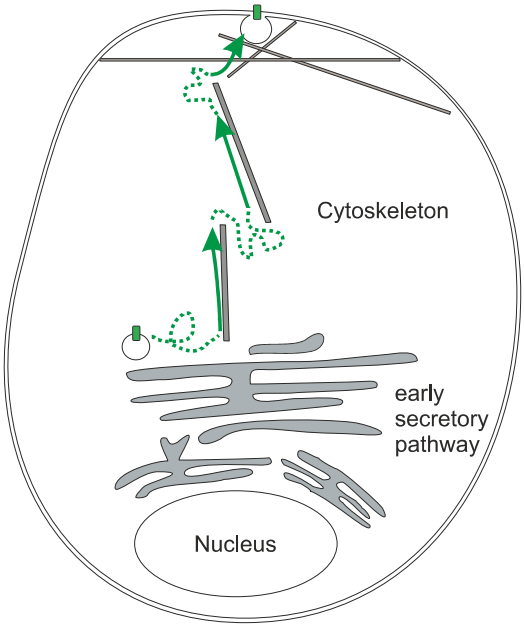

Figure 3.57: $Ca_V1.2$ shows alternating motion, combined of active transport and confined movement.

I conclude that since $Ca_V1.2$ shows alternating motion, its transport can be a mixture of active and passive sections. During its intracellular transport $Ca_V1.2$ channels switches between directed movement where it is actively transported by motor proteins along the cytoskeleton and confined movement, caused by interruptions during the transport (Figure 3.57).

4 Discussion

The regulation of the expression level of voltage-activated calcium channels at the plasma membrane is crucial for controlling the amount of calcium entering into the cell and thus for cell survival. The surface expression of the channel depends on its precise transport towards and from the plasma membrane. The biosynthetic secretory pathway of $Ca_V1.2$ starts with the release of the channel from the ER. In mammalian cells the entry point for membrane proteins into the secretory pathway is through specific exit sites within the ER (ERES), from where COPII vesicle buds for reaching the Golgi-network (Bannykh et al. 1996, Budnik and Stephens 2009, Palade 1975). For the $Ca_V1.2$ α_1-pore-forming subunit ER release is mediated by the regulatory β-subunit and several mechanisms have been proposed. $Ca_V\beta$ might unmask an ER retention signal (Bichet et al. 2000) or exposes an export signal in the channels' I-II loop nearby the $Ca_V\beta$ binding site or AID site (Fang and Colecraft 2011). In addition, Altier et al. (2011) found that $Ca_V\beta$ prevents the degradation of $Ca_V1.2$ by the ER associated degradation pathway (ERAD). This quality control for newly synthetized proteins in the ER acts in cellular homeostasis by preventing the accumulation of misfolded proteins within the ER membrane (Ruggiano et al. 2014).

Here, I show that in the absence of $Ca_V\beta$, $Ca_V1.2$ is excluded from the ERES. After coexpression with $Ca_V\beta$, the association of the two subunits occurs while the channel is inserted in the ER membrane and initiates the movement of the channel to the ERES. From here the channel must leave immediately towards the Golgi, because virtually no channels are found within ERES. Thus, the β-subunit appears to be the rate limiting factor to provide a very fast and efficient transport of the channel over the ERES to enter the biosynthetic pathway. Although, $Ca_V\beta$ is mandatory for the release of the channel from the ER, our results show that both subunits have not necessarily to be translated at the same time point. Within a defined time frame $Ca_V1.2$ stays in a conformation in which $Ca_V\beta$ can actively bind to the channel allowing its rapid exit from the ER to be transported towards the Golgi complex facing the ER (*cis*-Golgi). We found $Ca_V1.2$ overlapping with a *trans*-Golgi membrane protein in the presence of $Ca_V\beta$, but in its absence no channels were found in the Golgi system. This implies that $Ca_V1.2$ is degraded directly from the ER and no channel leaves the ER without $Ca_V\beta$. Thus, the channel control quality in the ER is very tight.

The intracellular transport machinery of $Ca_V1.2$ to the plasma membrane has been assumed, as for other cardiac ion channels, to be microtubule dependent (Hong et al. 2010, Smyth and

Shaw 2010, Steele and Fedida 2014). In this study I could show that $Ca_V1.2$ distributes lengthwise with tubulin filaments in both heterologous and endogenous system, suggesting that long-distance transport of $Ca_V1.2$ is done along tubulin tracks. Moreover, this transport along microtubules is F-actin independent, because it is preserved in the presence of the actin-disruptor cytochalasin D. The microtubule-dependance is also suggested to be required for translocation of proteins from the ER to the Golgi (Caviston and Holzbaur 2006, Watson et al. 2005). However, this could not be confirmed for $Ca_V1.2$ transport in this study. After tubulin disruption the translocation of vesicles from the ERES to the Golgi system still took place and $Ca_V1.2$ was found colocalized with *trans*-Golgi marker but not with ERES. So, the early steps of the biosynthetic pathway of $Ca_V1.2$ seem to be independent from microtubules integrity and only after the channel leaves the Golgi system it is transported along cytoskeletal tracks.

It has been shown that the association of $Ca_V\beta$ with the α_1-subunit is reversible at the level of the plasma membrane (Fang and Colecraft 2011, Hidalgo and Neely 2007). This raises the question if after association in the ER these subunits are cotransported towards the plasma membrane or they dissociate and travel separately from each other. Here, using a new strategy in which I analyzed not only their colocalization, but also their motional dynamics, I demonstrate cotransport of $Ca_V1.2$ and $Ca_V\beta$. Visual observations as well as the quantitative analysis of the movement of $Ca_V1.2$ revealed that the transport of the channel towards the plasma membrane takes place in an associated form together with $Ca_V\beta$. Statistical analysis resulted in a common peak of the highest speed values calculated from $Ca_V1.2$ and $Ca_V\beta$ coexpression experiments for each separated subunit. This fastest component is assumed to be cotransport, happening during an active transport mediated by motor proteins along microtubules. Whether during passive transport they are associated with each other remains elusive.

Different $Ca_V\beta$ isoforms are known to differentially affect the electrophysical properties of a channel in the plasma membrane (Hidalgo and Neely 2007). In my study, I found that the two isoforms of $Ca_V\beta$, 2a and 2b, also have a different impact on the channel's transport. To my knowledge this is the first hint that isoforms of $Ca_V\beta$ differently regulates the transport of the channel. $Ca_V1.2$ coexpressed with $Ca_V\beta2a$ show a faster transport over longer distances than coexpressed with $Ca_V\beta2b$. This difference might result from the distinct chemical properties of the two isoforms. Within the group of seven $Ca_V\beta2$ isoforms, only β2a and β2e are membrane associated by an N-terminal palmitoylation or a positively charged sequence, respectively. The membrane associated $Ca_V\beta$s are targeted to the plasma membrane

independently from $Ca_V\alpha_1$ and are known to dramatically slow down the voltage-dependent inactivation (Chien et al. 1998, Miranda-Laferte et al. 2014, Olcese et al. 1994). We hypothesize that the two isoforms of $Ca_V\beta$ might equally dissociate from the α_1-subunit, but $Ca_V\beta$2a with its membrane anchored motif remains in the vicinity of the channel and thus can easily reassociate. I envision that only associated channels might restore active transport through a mechanism yet to be discovered. The differentially effect of the two isoforms within the cotransport of both subunits adds a new regulatory activity for the multifunctional $Ca_V\beta$ (Hidalgo and Neely 2007, Hofmann et al. 2015). Since the β-subunit binds the channel with its GK domain, its SH3 domain remains available for protein-protein interactions (Mayer 2001, Opatowsky et al. 2004b). This also provides a new regulatory input for the transport channel complex.

In the dynamic analysis I showed that the transport of calcium channels is a mixture of active and passive transport. Evaluation of the anomalous α-coefficient of different segments during the channels trajectory demonstrated alternating motion of the channel. This has been simulated in previous studies for other protein transport processes (Brangwynne et al. 2009, Neri et al. 2013, Trybus 2013).

In vivo transport of neuronal voltage-activated calcium channels have been studied (Schneider et al. 2015). Neurons are polarized cells whereby proteins are synthesized in the soma and travels along microtubules through the axon (Hirokawa and Takemura 2005). Schneider et al. (2015) described mobility of neuronal $Ca_V2.1$ and $Ca_V2.2$ α_1-pore-forming subunits and found the same range of diffusion coefficient values with very similar median values as found in my study for $Ca_V1.2$. This highlights our conclusion that anterograde transport of $Ca_V1.2$ is microtubule-dependent.

The in vivo speed of kinesin (0.8 µm/s) motor proteins that walk along microtubules (Howard 2001) match the maximal speed values estimated by $Ca_V1.2$ movement (up to 0.7 µm/s). This supports the idea that $Ca_V1.2$ is transported by motor proteins along microtubule tracks. Between periods of active transport $Ca_V1.2$ showed passive motion sections. In these periods the channels transport might be paused due to the molecular crowdedness within the cell, so channels are stuck in the cytoskeletal network. Additional, it might be possible that more motor proteins with distinct movement directions bind to one vesicle, stucking the movement (Ross et al. 2008, Trybus 2013). Alternatively, as proposed before the active transport might be interrupted due to dissociation of $Ca_V\beta$.

In this study all my experimental results and previous work from our group point to a recycling pathway likely through cortical F-actin. In previous studies in our group $Ca_V\beta$ was found to bind to actin filaments (Stolting et al. 2015). Actin filaments are an important route in the last step previous to plasma membrane insertion or during endocytosis (Al-Bassam et al. 2012). I have shown that in heterologous and HL-1 cells while recycling takes place no lysosomal degradation was observed. These results explain recent data from our laboratory showing no alterations in L-type current expression following disruption of the tubulin network by nocodazole treatment. Recycling could compensate for the lack of channels coming from the secretory pathway along the microtubules in nocodazole treated cells. I do observed a nocodazole-induced dispersal of the Golgi resulting in a closeness of it to the plasma membrane (Cole et al. 1996) that may partially explain this effect. Despite of this, I demonstrate recycling in the absence of any pharmacological treatment. So, we propose endocytic recycling as a mechanism by which cells preserves steady expression of $Ca_V1.2$ channels in the plasma membrane. Worth to notice is that we do not observe changes in the currents and that pulse-chase experiments reported by other studies demonstrate that membrane-bound $Ca_V1.2$ has a half-life as short as 3 h (Chien et al. 1995), whereas total cellular $Ca_V1.2$ half-life could be as much as 25 h (Catalucci et al. 2013). This implies that within the time frame of our experiments the channel indeed is endocytosed. From this, we assume that there is a compensatory mechanism so that channels that are internalized are reinserted in the membrane to keep stable $Ca_V1.2$ expression levels in the cell surface.

In recent studies it has been shown that treatment of HL-1 cardiomyocytes with dynasore, an inhibitor of dynamin-dependent endocytosis, increased $Ca_V1.2$ surface expression while co-incubation of the cells with dynasore and nocodazole prevented $Ca_V1.2$ enhancement (Hong et al. 2010). These results are consistent with a microtubule-dependent biosynthetic forward transport for $Ca_V1.2$ and, most notably, they demonstrate the occurrence of dynamin-dependent endocytosis of this channel. This dynamin-dependent endocytosis of the calcium channel has been found to be actively provoked by $Ca_V\beta$ interacting with dynamin in *Xenopus laevis* (Gonzalez-Gutierrez et al. 2007, Miranda-Laferte et al. 2011). Consistent with the post-endocytic sorting found for other cardiac ion channels (Gao et al. 2012, Steele and Fedida 2014) my data on both, heterologous expressed and endogenous $Ca_V1.2$, revealed Rab5- and Rab11-dependent recycling pathways for this ion channel transmembrane protein. Recycling along actin filaments has been described to be driven by the motor protein myosin VI that is able to move in the minus-direction of the actin filaments towards the cell interior (Dance et

al. 2004, Roberts et al. 2004) and the conventional myosin V that is known to interact with Rab11 and transports proteins back to the plasma membrane (Lapierre et al. 2001, Schumacher-Bass et al. 2014, Seabra and Coudrier 2004).

In the quantitative analysis of the channels' dynamics I found that the internalized $Ca_V1.2$-HaloTag is not associated with $Ca_V\beta$. These results point toward the hypotheses that no cotransport takes place during retrograde trafficking. Furthermore they are consistent with previous studies that show that channels lacking the AID site are still internalized even in the presence of $Ca_V\beta$ (Gonzalez-Gutierrez et al. 2007).

I propose that after dissociation of $Ca_V\beta$ from the AID site of $Ca_V1.2$, the β-subunit triggers channels' endocytosis by association with dynamin (Gonzalez-Gutierrez et al. 2007) and $Ca_V\beta$ does not reassociate during the retrograde transport. The binding between the β-subunit and actin filaments (Stolting et al. 2015) would promote the anterograde transport for channel recycling. The latter is favored by recruiting the channel beneath the plasma membrane through the retention of $Ca_V1.2$-containing endosomes within the cortical actin cytoskeleton and preventing their transfer to the microtubule system. The recycling process may occur through myosin motor proteins walking along actin filaments. This is consistent with the range of speed values found for internalized $Ca_V1.2$, which include both, a pool of slow speed values, comparable to the speed of the retrograde moving myosin VI (0.05 µm/s) and values comparable with the speed of anterograde moving myosin V (0.2 µm/s) (Howard 2001) that can be four times faster. However, no faster speed values consistent to dynein (up to 1.1 µm/s) or kinesin velocities were estimated. Since dynein was found to stimulate early to late endosome fusion (Aniento et al. 1993, Murray and Wolkoff 2003, Neefjes and van der Kant 2014) this could be another hint for the internalized channel to be transported along a recycling rather than a degradational pathway. Taken together we propose that actin-dependent endocytic recycling of $Ca_V1.2$ is responsible for maintaining a stable L-type current surface expression. The regulating factor for the channels internalization and retrograde transport to recycling endosomes is the dissociation of $Ca_V\beta$ at the level of the plasma membrane. All together this study emphazised the relevance of $Ca_V\beta$ in the quality control for $Ca_V1.2$'s protein function at different steps of the channels life cycle; immatured channels in the ER are allowed to exit to the secretory pathway and matured channels in the plasma membrane are retained until $Ca_V\beta$ dissociates.

In conclusion my studies contribute to the understanding of the intracellular transport of voltage-activated calcium channels. Figure 4.1 shows a graphic summary of my results. I could show that $Ca_V\beta$ is the rate limiting factor for the efficient release of $Ca_V1.2$ over ERES to the trans-Golgi system, independently from the microtubule network. From there the channel is actively cotransported with $Ca_V\beta$ by motor proteins along microtubule tracks. Alternating motion of $Ca_V1.2$ shows that during this itinerary towards the plasma membrane the transport is interrupted. Here different $Ca_V\beta$ isoforms have different impact on the channels transport dynamics. At the level of the plasma membrane I postulate a model by which actin-dependent endocytic recycling regulates $Ca_V1.2$ homeostasis in the plasma membrane. Here again $Ca_V\beta$ is the regulatory factor providing an internalization of the channel towards the recycling endosomes until an association of both subunits initiates a reinsertion in the plasma membrane.

A better understanding of the regulation of voltage activated calcium channels surface expression may hopefully inspire the development of strategies to interfere with the process of transport of calcium channels that is affected in human diseases.

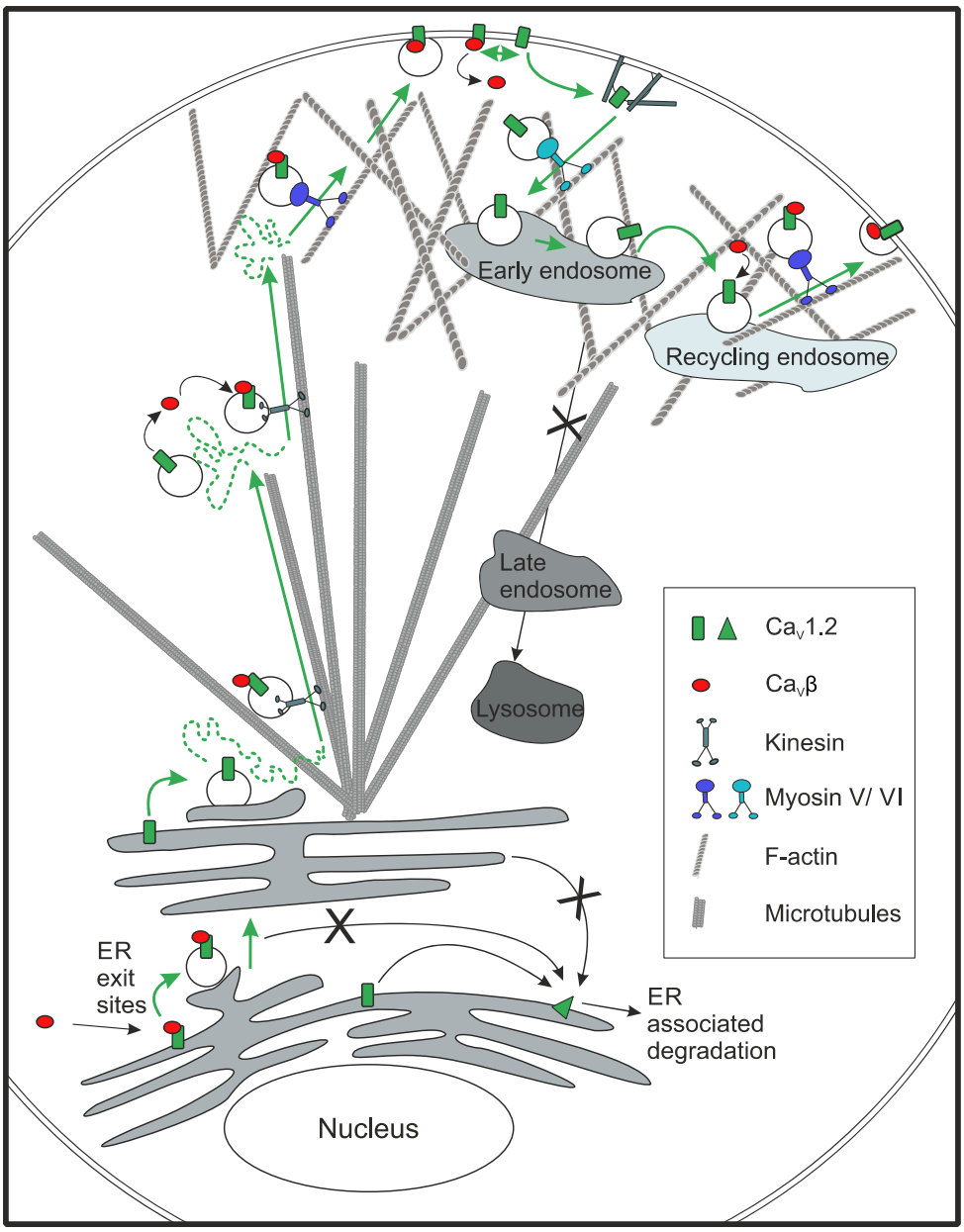

Figure 4.1: Graphical summary of the calcium channels' transport described in this study. In the presence of $Ca_V\beta$, $Ca_V1.2$ is efficiently transported from the ER through ER exit sites to the Golgi system. From there both subunits are cotransported by motor proteins along cytoskeletal tracks, showing alternating active and passive motion. In the plasma membrane the channels expression is regulated by an endosomal recycling pathway, in which the internalized channels are transported without $Ca_V\beta$ to recycling compartments from where they are recruited to be reinserted in the plasma membrane.

5 Literature

Ahmed, W. W., Williams, B. J., Silver, A. M. and Saif, T. A. (2013) Measuring nonequilibrium vesicle dynamics in neurons under tension. Lab Chip 13: 570-8.

Al-Bassam, S., Xu, M., Wandless, T. J. and Arnold, D. B. (2012) Differential trafficking of transport vesicles contributes to the localization of dendritic proteins. Cell Rep 2: 89-100.

Alberts, B. (2008) Molecular biology of the cell. Garland Science, pp.

Altier, C., Garcia-Caballero, A., Simms, B., You, H., Chen, L., Walcher, J., Tedford, H. W., Hermosilla, T. and Zamponi, G. W. (2011) The $Ca_V\beta$ subunit prevents RFP2-mediated ubiquitination and proteasomal degradation of L-type channels. Nat Neurosci 14: 173-80.

Altman, D., Goswami, D., Hasson, T., Spudich, J. A. and Mayor, S. (2007) Precise positioning of myosin VI on endocytic vesicles in vivo. PLoS Biol 5: e210.

Ando, T. and Skolnick, J. (2010) Crowding and hydrodynamic interactions likely dominate in vivo macromolecular motion. Proceedings of the National Academy of Sciences 107: 18457-18462.

Aniento, F, Emans, N, Griffiths, G and Gruenberg, J (1993) Cytoplasmic dynein-dependent vesicular transport from early to late endosomes. The Journal of Cell Biology 123: 1373-1387.

Aschenbrenner, L., Naccache, S. N. and Hasson, T. (2004) Uncoated Endocytic Vesicles Require the Unconventional Myosin, Myo6, for Rapid Transport through Actin Barriers. Molecular Biology of the Cell 15: 2253-2263.

Babst, M. (2014) Quality control at the plasma membrane: One mechanism does not fit all. The Journal of Cell Biology 205: 11-20.

Banks, D. S. and Fradin, C. (2005) Anomalous diffusion of proteins due to molecular crowding. Biophys J 89: 2960-71.

Bannykh, S I, Rowe, T and Balch, W E (1996) The organization of endoplasmic reticulum export complexes. The Journal of Cell Biology 135: 19-35.

Beguin, P., Mahalakshmi, R. N., Nagashima, K., Cher, D. H. K., Takahashi, A., Yamada, Y., Seino, Y. and Hunziker, W. (2005) 14-3-3 and calmodulin control subcellular distribution of Kir/Gem and its regulation of cell shape and calcium channel activity. Journal of Cell Science 118: 1923-1934.

Beguin, P., Nagashima, K., Gonoi, T., Shibasaki, T., Takahashi, K., Kashima, Y., Ozaki, N., Geering, T., Iwanaga, T. and Seino, S. (2001) Regulation of Ca^{2+} channel expression at the cell surface by the small G-protein kir/Gem. Nature 411: 701-706.

Berridge, M. J., Lipp, P. and Bootman, M. D. (2000) The versatility and universality of calcium signalling. Nat Rev Mol Cell Biol 1: 11-21.

Bhattacharyya, D. and Glick, B. S. (2007) Two mammalian Sec16 homologues have nonredundant functions in endoplasmic reticulum (ER) export and transitional ER organization. Mol Biol Cell 18: 839-49.

Bichet, D., Cornet, V., Geib, S., Carlier, E., Volsen, S., Hoshi, T., Mori, Y. and De Waard, M. (2000) The I-II loop of the Ca^{2+} channel α_1 subunit contains an endoplasmic reticulum retention signal antagonized by the β subunit. Neuron 25: 177-90.

Bolte, S. and Cordelieres, F. P. (2006) A guided tour into subcellular colocalization analysis in light microscopy. J Microsc 224: 213-32.

Bouchaud, J-P. and Georges, A. (1990) Anomalous diffusion in disordered media: Statistical mechanisms, models and physical applications. Physics Reports 195: 127-293.

Braakman, I. and Bulleid, N. J. (2011) Protein Folding and Modification in the Mammalian Endoplasmic Reticulum. Annual Review of Biochemistry 80: 71-99.

Brangwynne, C. P., Koenderink, G. H., Mackintosh, F. C. and Weitz, D. A. (2009) Intracellular transport by active diffusion. Trends Cell Biol 19: 423-7.

Budnik, A. and Stephens, D. J. (2009) ER exit sites--localization and control of COPII vesicle formation. FEBS Lett 583: 3796-803.

Buraei, Z. and Yang, J. (2010) The β Subunit of Voltage-Gated Calcium Channels. Physiological Reviews 90: 1461-1506.

Campiglio, M., Di Biase, V., Tuluc, P. and Flucher, B. E. (2013) Stable incorporation versus dynamic exchange of β subunits in a native Ca^{2+} channel complex. Journal of Cell Science 126: 2092-2101.

Campiglio, M. and Flucher, B. E. (2015) The role of auxiliary subunits for the functional diversity of voltage-gated calcium channels. J Cell Physiol 230: 2019-31.

Catalucci, D., Zhang, D.-H., Desantiago, J., Aimond, F., Barbara, G., Chemin, J., Bonci, D., Picht, E., Rusconi, F., Dalton, N. D., Peterson, K. L., Richard, S., Bers, D. M., Brown, J. H. and Condorelli, G. (2013) Akt regulates L-type Ca^{2+} channel activity by modulating $Ca_V\alpha_1$ protein stability. The Journal of Cell Biology 200: 851-851.

Catterall, W. A. (2011) Voltage-Gated Calcium Channels. Cold Spring Harbor Perspectives in Biology 3:

Catterall, W. A., Perez-Reyes, E., Snutch, T. P. and Striessnig, J. (2005) International Union of Pharmacology. XLVIII. Nomenclature and Structure-Function Relationships of Voltage-Gated Calcium Channels. Pharmacological Reviews 57: 411-425.

Caviston, J. P. and Holzbaur, E. L. F. (2006) Microtubule motors at the intersection of trafficking and transport. Trends in Cell Biology 16: 530-537.

Chen, C. and Okayama, H. (1987) High-efficiency transformation of mammalian cells by plasmid DNA. Mol Cell Biol 7: 2745-52.

Chen, Y. C., Li, M., Zhang, Y., He, L., Yamada, Y., Fitzmaurice, A., Shen, Y., Zhang, H., Tong, L. and Yang, J. (2004) Structural basis of the α_1-β subunit interaction of voltage-gated Ca^{2+} channels. Nature 429: 675-680.

Chibalina, M. V., Seaman, M. N. J., Miller, C. C., Kendrick-Jones, J. and Buss, F. (2007) Myosin VI and its interacting protein LMTK2 regulate tubule formation and transport to the endocytic recycling compartment. Journal of Cell Science 120: 4278-4288.

Chien, A. J., Gao, T., Perez-Reyes, E. and Hosey, M. M. (1998) Membrane Targeting of L-type Calcium Channels: Role of palmitoylation in the subcellular localization of the β2a subunit. Journal of Biological Chemistry 273: 23590-23597.

Chien, A. J., Zhao, X., Shirokov, R. E., Puri, T. S., Chang, C. F., Sun, D. Y., Rios, E. and Hosey, M. M. (1995) Roles of a Membrane-localized β Subunit in the Formation and Targeting of Functional L-type Ca^{2+} Channels. Journal of Biological Chemistry 270: 30036-30044.

Claessen, J. H. L., Kundrat, L. and Ploegh, H. L. (2012) Protein quality control in the ER: balancing the ubiquitin checkbook. Trends in Cell Biology 22: 22-32.

Clapham, D. E. (2007) Calcium Signaling. Cell 131: 1047-1058.

Cole, N. B., Sciaky, N., Marotta, A., Song, J. and Lippincott-Schwartz, J. (1996) Golgi dispersal during microtubule disruption: regeneration of Golgi stacks at peripheral endoplasmic reticulum exit sites. Molecular Biology of the Cell 7: 631-650.

Cole, R. (2014) Live-cell imaging. Cell Adh Migr 8: 452-9.

Dalton, S., Takahashi, S. X., Miriyala, J. and Colecraft, H. M. (2005) A single $Ca_V\beta$ can reconstitute both trafficking and macroscopic conductance of voltage-dependent calcium channels. The Journal of Physiology 567: 757-769.

Dance, A. L., Miller, M., Seragaki, S., Aryal, P., White, B., Aschenbrenner, L. and Hasson, T. (2004) Regulation of Myosin-VI Targeting to Endocytic Compartments. Traffic 5: 798-813.

Desnos, C., Huet, S. and Darchen, F. (2007) 'Should I stay or should I go?': myosin V function in organelle trafficking. Biology of the Cell 99: 411-423.

Dix, J. A. and Verkman, A. S. (2008) Crowding Effects on Diffusion in Solutions and Cells. Annual Review of Biophysics 37: 247-263.

Doherty, G. J. and Mcmahon, H. T. (2009) Mechanisms of endocytosis. Annu Rev Biochem 78: 857-902.

Dolphin, A. C. (2003) β subunits of voltage-gated calcium channels. J Bioenerg Biomembr 35: 599-620.

Dupont, A., Stirnnagel, K., Lindemann, D. and Lamb, D. C. (2013) Tracking image correlation: combining single-particle tracking and image correlation. Biophys J 104: 2373-82.

Egea, G., Lazaro-Dieguez, F. and Vilella, M. (2006) Actin dynamics at the Golgi complex in mammalian cells. Curr Opin Cell Biol 18: 168-78.

Egea, G., Serra-Peinado, C., Salcedo-Sicilia, L. and Gutierrez-Martinez, E. (2013) Actin acting at the Golgi. Histochem Cell Biol 140: 347-60.

Einstein, A. (1905) Über die von der molekularkinetischen Theorie der Wärme geforderte Bewegung von in ruhenden Flüssigkeiten suspendierten Teilchen. Annalen der Physik 322: 549-560.

Fang, K. and Colecraft, H. M. (2011) Mechanism of auxiliary β-subunit-mediated membrane targeting of L-type ($Ca_V1.2$) channels. J Physiol 589: 4437-55.

Fletcher, D. A. and Mullins, R. D. (2010) Cell mechanics and the cytoskeleton. Nature 463: 485-92.

Flores-Rodriguez, N., Rogers, S. S., Kenwright, D. A., Waigh, T. A., Woodman, P. G. and Allan, V. J. (2011) Roles of Dynein and Dynactin in Early Endosome Dynamics Revealed Using Automated Tracking and Global Analysis. Plos One 6:

Gao, Y., Bertuccio, C. A., Balut, C. M., Watkins, S. C. and Devor, D. C. (2012) Dynamin- and Rab5-dependent endocytosis of a Ca^{2+} -activated K^+ channel, KCa2.3. PLoS One 7: e44150.

Gonzalez-Gutierrez, G., Miranda-Laferte, E., Neely, A. and Hidalgo, P. (2007) The Src homology 3 domain of the β-subunit of voltage-gated calcium channels promotes endocytosis via dynamin interaction. J Biol Chem 282: 2156-62.

Graham, F. L., Smiley, J., Russell, W. C. and Nairn, R. (1977) Characteristics of a human cell line transformed by DNA from human adenovirus type 5. J Gen Virol 36: 59-74.

Grant, B. D. and Donaldson, J. G. (2009) Pathways and mechanisms of endocytic recycling. Nat Rev Mol Cell Biol 10: 597-608.

Hale, C. M., Chen, W. C., Khatau, S. B., Daniels, B. R., Lee, J. S. and Wirtz, D. (2011) SMRT analysis of MTOC and nuclear positioning reveals the role of EB1 and LIC1 in single-cell polarization. J Cell Sci 124: 4267-85.

Hall, D. and Hoshino, M. (2010) Effects of macromolecular crowding on intracellular diffusion from a single particle perspective. Biophysical Reviews 2: 39-53.

Herrmann, H. and Aebi, U. (2000) Intermediate filaments and their associates: multi-talented structural elements specifying cytoarchitecture and cytodynamics. Curr Opin Cell Biol 12: 79-90.

Hidalgo, P., Gonzalez-Gutierrez, G., Garcia-Olivares, J. and Neely, A. (2006) The α_1-β-subunit interaction that modulates calcium channel activity is reversible and requires a competent alpha-interaction domain. J Biol Chem 281: 24104-10.

Hidalgo, P. and Neely, A. (2007) Multiplicity of protein interactions and functions of the voltage-gated calcium channel β-subunit. Cell Calcium 42: 389-96.

Hinshaw, J. E. (2000) Dynamin and Its Role in Membrane Fission. Annual Review of Cell and Developmental Biology 16: 483-519.

Hirokawa, N., Noda, Y., Tanaka, Y. and Niwa, S. (2009) Kinesin superfamily motor proteins and intracellular transport. Nat Rev Mol Cell Biol 10: 682-96.

Hirokawa, N. and Takemura, R. (2005) Molecular motors and mechanisms of directional transport in neurons. Nat Rev Neurosci 6: 201-214.

Hofmann, F., Belkacemi, A. and Flockerzi, V. (2015) Emerging Alternative Functions for the Auxiliary Subunits of the Voltage- Gated Calcium Channels. Current Molecular Pharmacology 8: 162-168.

Hofmann, F., Flockerzi, V., Kahl, S. and Wegener, J. W. (2014) L-type $Ca_V1.2$ calcium channels: from in vitro findings to in vivo function. Physiol Rev 94: 303-26.

Hong, T. T., Smyth, J. W., Gao, D., Chu, K. Y., Vogan, J. M., Fong, T. S., Jensen, B. C., Colecraft, H. M. and Shaw, R. M. (2010) BIN1 localizes the L-type calcium channel to cardiac T-tubules. PLoS Biol 8: e1000312.

Horgan, C.P. and Mccaffrey, M.W. (2011) Rab GTPases and microtubule motors. Biochemical Society Transactions 39: 1202-1206.

Howard, J. (2001) Mechanics of motor proteins and the cytoskeleton. Sinauer Associates, Publishers, xvi, 367 p. pp.

Hughes, H., Budnik, A., Schmidt, K., Palmer, K. J., Mantell, J., Noakes, C., Johnson, A., Carter, D. A., Verkade, P., Watson, P. and Stephens, D. J. (2009) Organisation of human ER-exit sites: requirements for the localisation of Sec16 to transitional ER. J Cell Sci 122: 2924-34.

Ivanov, A. I. (2008) Exocytosis and Endocytosis. Humana Press, pp.

Jaqaman, K., Loerke, D., Mettlen, M., Kuwata, H., Grinstein, S., Schmid, S. L. and Danuser, G. (2008) Robust single-particle tracking in live-cell time-lapse sequences. Nat Methods 5: 695-702.

Jordan, M. A. and Wilson, L. (2004) Microtubules as a target for anticancer drugs. Nat Rev Cancer 4: 253-65.

Jovic, M., Sharma, M., Rahajeng, J. and Caplan, S. (2010) The early endosome: a busy sorting station for proteins at the crossroads. Histology and Histopathology 25: 99-112.

Kalaidzidis, Y. (2007) Intracellular objects tracking. European Journal of Cell Biology 86: 569-578.

Kincaid, M. and Cooper, A. (2007) Misfolded Proteins Traffic from the Endoplasmic Reticulum (ER) Due to ER Export Signals. Molecular Biology of the Cell 18: 455-463.

Kirchhausen, T. (2000) Clathrin. Annual Review of Biochemistry 69: 699-727.

Krendel, M. and Mooseker, M. S. (2005) Myosins: tails (and heads) of functional diversity. Physiology (Bethesda) 20: 239-51.

Langford, G. M. (2002) Myosin-V, a versatile motor for short-range vesicle transport. Traffic 3: 859-65.

Lanzetti, L. (2007) Actin in membrane trafficking. Curr Opin Cell Biol 19: 453-8.

Lapierre, L. A., Kumar, R., Hales, C. M., Navarre, J., Bhartur, S. G., Burnette, J. O., Provance, D. W., Jr., Mercer, J. A., Bahler, M. and Goldenring, J. R. (2001) Myosin vb is associated with plasma membrane recycling systems. Mol Biol Cell 12: 1843-57.

Lingwood, D. and Simons, K. (2010) Lipid rafts as a membrane-organizing principle. Science 327: 46-50.

Luby-Phelps, K. (2000) Cytoarchitecture and physical properties of cytoplasm: volume, viscosity, diffusion, intracellular surface area. Int Rev Cytol 192: 189-221.

Lund, F. W., Jensen, M. L., Christensen, T., Nielsen, G. K., Heegaard, C. W. and Wustner, D. (2014) SpatTrack: an imaging toolbox for analysis of vesicle motility and distribution in living cells. Traffic 15: 1406-29.

Manders, E. M. M., Verbeek, F. J. and Aten, J. A. (1993) Measurement of Colocalization of Objects in Dual-Color Confocal Images. Journal of Microscopy-Oxford 169: 375-382.

Maxfield, F. R. and Mcgraw, T. E. (2004) Endocytic recycling. Nat Rev Mol Cell Biol 5: 121-32.

Mayer, B.J. (2001) SH3 domains: complexity in moderation. Journal of Cell Science 114: 1253-1263.

Mayor, S. and Pagano, R. E. (2007) Pathways of clathrin-independent endocytosis. Nat Rev Mol Cell Biol 8: 603-12.

Mcmahon, H. T. and Boucrot, E. (2011) Molecular mechanism and physiological functions of clathrin-mediated endocytosis. Nat Rev Mol Cell Biol 12: 517-533.

Mehta, A. D., Rock, R. S., Rief, M., Spudich, J. A., Mooseker, M. S. and Cheney, R. E. (1999) Myosin-V is a processive actin-based motor. Nature 400: 590-593.

Merrifield, C. J., Feldman, M. E., Wan, L. and Almers, W. (2002) Imaging actin and dynamin recruitment during invagination of single clathrin-coated pits. Nat Cell Biol 4: 691-698.

Merrifield, C. J., Perrais, D. and Zenisek, D. (2005) Coupling between Clathrin-Coated-Pit Invagination, Cortactin Recruitment, and Membrane Scission Observed in Live Cells. Cell 121: 593-606.

Michalet, X. (2010) Mean square displacement analysis of single-particle trajectories with localization error: Brownian motion in an isotropic medium. Phys Rev E Stat Nonlin Soft Matter Phys 82: 041914.

Miranda-Laferte, E., Ewers, D., Guzman, R. E., Jordan, N., Schmidt, S. and Hidalgo, P. (2014) The N-terminal domain tethers the voltage-gated calcium channel β2e-subunit to the plasma membrane via electrostatic and hydrophobic interactions. J Biol Chem 289: 10387-98.

Miranda-Laferte, E., Gonzalez-Gutierrez, G., Schmidt, S., Zeug, A., Ponimaskin, E. G., Neely, A. and Hidalgo, P. (2011) Homodimerization of the Src homology 3 domain of the calcium channel β-subunit drives dynamin-dependent endocytosis. J Biol Chem 286: 22203-10.

Mizuno-Yamasaki, E., Rivera-Molina, F. and Novick, P. (2012) GTPase Networks in Membrane Traffic. Annual Review of Biochemistry 81: 637-659.

Mu, F. T., Callaghan, J. M., Steelemortimer, O., Stenmark, H., Parton, R. G., Campbell, P. L., Mccluskey, J., Yeo, J. P., Tock, E. P. C. and Toh, B. H. (1995) EEA1, an Early Endosome-Associated Protein - Eea1 Is a Conserved α-Helical Peripheral Membrane-Protein Flanked by Cysteine Fingers and Contains a Calmodulin-Binding IQ Motif. Journal of Biological Chemistry 270: 13503-13511.

Murray, J. W. and Wolkoff, A. W. (2003) Roles of the cytoskeleton and motor proteins in endocytic sorting. Adv Drug Deliv Rev 55: 1385-403.

Nakano, A. (2002) Spinning-disk confocal microscopy -- a cutting-edge tool for imaging of membrane traffic. Cell Struct Funct 27: 349-55.

Nakano, A. and Luini, A. (2010) Passage through the Golgi. Curr Opin Cell Biol 22: 471-8.

Neefjes, J. and Van Der Kant, R. (2014) Stuck in traffic: an emerging theme in diseases of the nervous system. Trends Neurosci 37: 66-76.

Neely, A. and Hidalgo, P. (2014) Structure-function of proteins interacting with the α_1 pore-forming subunit of high-voltage-activated calcium channels. Front Physiol 5: 209.

Neri, I., Kern, N. and Parmeggiani, A. (2013) Modeling cytoskeletal traffic: an interplay between passive diffusion and active transport. Phys Rev Lett 110: 098102.

Ohashi, E., Tanabe, K., Henmi, Y., Mesaki, K., Kobayashi, Y. and Takei, K. (2011) Receptor sorting within endosomal trafficking pathway is facilitated by dynamic actin filaments. PLoS One 6: e19942.

Olcese, R., Qin, N., Schneider, T., Neely, A., Wei, X., Stefani, E. and Birnbaumer, L. (1994) The amino terminus of a calcium channel β subunitsets rates of channel inactivation independently of the subunit's effect on activation. Neuron 13: 1433-1438.

Olzmann, J. A., Kopito, R. R. and Christianson, J. C. (2013) The mammalian endoplasmic reticulum-associated degradation system. Cold Spring Harb Perspect Biol 5:

Opatowsky, Y., Chomsky-Hecht, O. and Hirsch, J. A. (2004a) Expression, purification and crystallization of a functional core of the voltage-dependent calcium channel β subunit. Acta Crystallographica Section D-Biological Crystallography 60: 1301-1303.

Opatowsky, Yarden, Chen, Chien-Chang, Campbell, Kevin P. and Hirsch, Joel A. (2004b) Structural Analysis of the Voltage-Dependent Calcium Channel β Subunit Functional Core and Its Complex with the α_1 Interaction Domain. Neuron 42: 387-399.

Palade, G (1975) Intracellular aspects of the process of protein synthesis. Science 189: 347-358.

Pragnell, M., De Waard, M., Tanabe, T., Snutch, T. P. and Campbell, K. P. (1994) Calcium channel β-subunit binds to a conserved motif in the I-II cytoplasmic linker of the α_1-subunit. Nature 368: 67-70.

Rapoport, T. A. (2007) Protein translocation across the eukaryotic endoplasmic reticulum and bacterial plasma membranes. Nature 450: 663-9.

Roberts, A. J., Kon, T., Knight, P. J., Sutoh, K. and Burgess, S. A. (2013) Functions and mechanics of dynein motor proteins. Nat Rev Mol Cell Biol 14: 713-26.

Roberts, R., Lister, I., Schmitz, S., Walker, M., Veigel, C., Trinick, J., Buss, F. and Kendrick-Jones, J. (2004) Myosin VI: cellular functions and motor properties. Philos Trans R Soc Lond B Biol Sci 359: 1931-44.

Ross, J. L., Ali, M. Y. and Warshaw, D. M. (2008) Cargo transport: molecular motors navigate a complex cytoskeleton. Curr Opin Cell Biol 20: 41-7.

Ruggiano, A., Foresti, O. and Carvalho, P. (2014) ER-associated degradation: Protein quality control and beyond. The Journal of Cell Biology 204: 869-879.

Ruthardt, N., Lamb, D. C. and Brauchle, C. (2011) Single-particle tracking as a quantitative microscopy-based approach to unravel cell entry mechanisms of viruses and pharmaceutical nanoparticles. Mol Ther 19: 1199-211.

Samaj, J., Baluska, F., Voigt, B., Schlicht, M., Volkmann, D. and Menzel, D. (2004) Endocytosis, actin cytoskeleton, and signaling. Plant Physiology 135: 1150-1161.

Saxton, M. J. (1993) Lateral diffusion in an archipelago. Dependence on tracer size. Biophysical Journal 64: 1053-1062.

Saxton, M. J. (2008) Single-particle tracking: connecting the dots. Nat Methods 5: 671-2.

Saxton, M. J. (2009) Single Particle Tracking. In: Jue, Thomas (eds.) Fundamental Concepts in Biophysics: Volume 1. Humana Press, pp. 1-33.

Saxton, M. J. and Jacobson, K. (1997) Single Particle Tracking: Applications to Membrane Dynamics. Annual Review of Biophysics and Biomolecular Structure 26: 373-399.

Sbalzarini, I. F. and Koumoutsakos, P. (2005) Feature point tracking and trajectory analysis for video imaging in cell biology. J Struct Biol 151: 182-95.

Schneider, R., Hosy, E., Kohl, J., Klueva, J., Choquet, D., Thomas, U., Voigt, A. and Heine, M. (2015) Mobility of calcium channels in the presynaptic membrane. Neuron 86: 672-9.

Schumacher-Bass, S. M., Vesely, E. D., Zhang, L., Ryland, K. E., Mcewen, D. P., Chan, P. J., Frasier, C. R., Mcintyre, J. C., Shaw, R. M. and Martens, J. R. (2014) Role for myosin-V motor proteins in the selective delivery of Kv channel isoforms to the membrane surface of cardiac myocytes. Circ Res 114: 982-92.

Seabra, M. C. and Coudrier, E. (2004) Rab GTPases and myosin motors in organelle motility. Traffic 5: 393-9.

Semenova, I., Burakov, A., Berardone, N., Zaliapin, I., Slepchenko, B., Svitkina, T., Kashina, A. and Rodionov, V. (2008) Actin dynamics is essential for myosin-based transport of membrane organelles. Curr Biol 18: 1581-6.

Serge, A., Bertaux, N., Rigneault, H. and Marguet, D. (2008) Dynamic multiple-target tracing to probe spatiotemporal cartography of cell membranes. Nat Methods 5: 687-94.

Shaner, N. C., Lambert, G. G., Chammas, A., Ni, Y., Cranfill, P. J., Baird, M. A., Sell, B. R., Allen, J. R., Day, R. N., Israelsson, M., Davidson, M. W. and Wang, J. (2013) A bright monomeric green fluorescent protein derived from *Branchiostoma lanceolatum*. Nat Methods 10: 407-9.

Shaner, N. C., Steinbach, P. A. and Tsien, R. Y. (2005) A guide to choosing fluorescent proteins. Nat Methods 2: 905-9.

Shaw, R. M. and Colecraft, H. M. (2013) L-type calcium channel targeting and local signalling in cardiac myocytes. Cardiovasc Res 98: 177-86.

Smyth, J. W. and Shaw, R. M. (2010) Forward trafficking of ion channels: what the clinician needs to know. Heart Rhythm 7: 1135-40.

Smyth, J. W., Vogan, J. M., Buch, P. J., Zhang, S. S., Fong, T. S., Hong, T. T. and Shaw, R. M. (2012) Actin cytoskeleton rest stops regulate anterograde traffic of connexin 43 vesicles to the plasma membrane. Circ Res 110: 978-89.

Steele, D. F. and Fedida, D. (2014) Cytoskeletal roles in cardiac ion channel expression. Biochim Biophys Acta 1838: 665-73.

Stenmark, H. (2009) Rab GTPases as coordinators of vesicle traffic. Nature Reviews Molecular Cell Biology 10: 513-525.

Stolting, G., De Oliveira, R. C., Guzman, R. E., Miranda-Laferte, E., Conrad, R., Jordan, N., Schmidt, S., Hendriks, J., Gensch, T. and Hidalgo, P. (2015) Direct interaction of $Ca_V\beta$ with actin up-regulates L-type calcium currents in HL-1 cardiomyocytes. J Biol Chem 290: 4561-72.

Stotz, S. C., Jarvis, S. E. and Zamponi, G. W. (2004) Functional roles of cytoplasmic loops and pore lining transmembrane helices in the voltage-dependent inactivation of HVA calcium channels. The Journal of Physiology 554: 263-273.

Striessnig, J., Pinggera, A., Kaur, G., Bock, G. and Tuluc, P. (2014) L-type Ca^{2+} channels in heart and brain. Wiley Interdisciplinary Reviews: Membrane Transport and Signaling 3: 15-38.

Szydlowska, K. and Tymianski, M. (2010) Calcium, ischemia and excitotoxicity. Cell Calcium 47: 122-129.

Traub, L. M. (2009) Tickets to ride: selecting cargo for clathrin-regulated internalization. Nat Rev Mol Cell Biol 10: 583-596.

Trybus, K. M. (2013) Intracellular transport: the causes for pauses. Curr Biol 23: R623-5.

Vale, R. D. (2003) The molecular motor toolbox for intracellular transport. Cell 112: 467-80.

Van Petegem, F., Clark, K. A., Chatelain, F. C. and Minor, D. L., Jr. (2004) Structure of a complex between a voltage-gated calcium channel β-subunit and an α_1-subunit domain. Nature 429: 671-5.

Vashist, S., Kim, W., Belden, W. J., Spear, E. D., Barlowe, C. and Ng, D. T.W. (2001) Distinct retrieval and retention mechanisms are required for the quality control of endoplasmic reticulum protein folding. The Journal of Cell Biology 155: 355-368.

Walter, P. and Johnson, A. E. (1994) Signal sequence recognition and protein targeting to the endoplasmic reticulum membrane. Annu Rev Cell Biol 10: 87-119.

Watson, P., Forster, R., Palmer, K. J., Pepperkok, R. and Stephens, D. J. (2005) Coupling of ER exit to microtubules through direct interaction of COPII with dynactin. Nat Cell Biol 7: 48-55.

Weiss, M., Elsner, M., Kartberg, F. and Nilsson, T. (2004) Anomalous subdiffusion is a measure for cytoplasmic crowding in living cells. Biophys J 87: 3518-24.

Wells, A. L., Lin, A. W., Chen, L.-Q., Safer, D., Cain, S. M., Hasson, T., Carragher, B. O., Milligan, R. A. and Sweeney, H. L. (1999) Myosin VI is an actin-based motor that moves backwards. Nature 401: 505-508.

Woll, D., Kolbl, C., Stempfle, B. and Karrenbauer, A. (2013) A novel method for automatic single molecule tracking of blinking molecules at low intensities. Physical Chemistry Chemical Physics 15: 6196-6205.

Wu, J., Yan, Z., Li, Z., Qian, X., Lu, S., Dong, M., Zhou, Q. and Yan, N. (2016) Structure of the voltage-gated calcium channel $Ca_V1.1$ at 3.6 Å resolution. Nature 537: 191-196.

Yarar, D., Waterman-Storer, C. M. and Schmid, S. L. (2005) A dynamic actin cytoskeleton functions at multiple stages of clathrin-mediated endocytosis. Mol Biol Cell 16: 964-75.

Yunker, A. M. R. and Mcenery, M. W. (2003) Low-voltage-activated ("T-type") calcium channels in review. Journal of Bioenergetics and Biomembranes 35: 533-575.

Zaarur, N., Meriin, A. B., Gabai, V. L. and Sherman, M. Y. (2008) Triggering Aggresome Formation: Dissecting Aggresome-targeting and aggregation signals in synphilin 1. Journal of Biological Chemistry 283: 27575-27584.

Zajac, A. L., Goldman, Y. E., Holzbaur, E. L. and Ostap, E. M. (2013) Local cytoskeletal and organelle interactions impact molecular-motor- driven early endosomal trafficking. Curr Biol 23: 1173-80.

Zerial, M. and Mcbride, H. (2001) Rab proteins as membrane organizers. Nat Rev Mol Cell Biol 2: 107-17.

Zinchuk, V. and Grossenbacher-Zinchuk, O. (2014) Quantitative colocalization analysis of fluorescence microscopy images. Curr Protoc Cell Biol 62: Unit 4 19 1-14.

Zinchuk, V., Wu, Y. and Grossenbacher-Zinchuk, O. (2013) Bridging the gap between qualitative and quantitative colocalization results in fluorescence microscopy studies. Scientific Reports 3: 1365.